



MONASH University

Problems in Low-Mass Stellar Rotation

Tanner A. Wilson

Doctor of Philosophy

A Thesis Submitted for the Degree of Doctor of Philosophy at
Monash University in 2023
School of Physics and Astronomy

Copyright notice

I certify that I have made all reasonable efforts to secure copyright permissions for third-party content included in this thesis and have not knowingly added copyright content to my work without the owner's permission.

©Tanner A. Wilson (2023).

Abstract

Our understanding of stellar rotation has evolved throughout history, mirroring the discoveries made by early astronomers who revealed the spinning nature of our Sun. In recent times, time-series space-based photometry has revolutionised the study of stellar rotation, enabling us to probe the rotational behaviour of numerous stars, including their internal profiles. However, these advancements have unveiled discrepancies in our current understanding of the evolution of rotation throughout a star's lifetime and the impact rotation has on other observables. This dissertation addresses three distinct challenges in the field of stellar rotation.

First, we show that independent constraints on the surface rotation rates of subgiants allow for more precise inferences on the internal rotation profile shape when performing forward modelling given some observed rotational splittings. We discuss the implications of this result on inferring the missing angular momentum transport required to explain the observed core and surface rotation rates of subgiant stars. Secondly, we adopt a model of stellar spectra with stellar spots to investigate the effect that spots have on the inference of stellar parameters. We do this by generating a synthetic population of stellar spectra with physically motivated stellar and spot parameters and fitting those spectra with a spotted and non-spotted model of the stellar atmosphere. We show that if stellar spots are not accounted for in models of the stellar atmosphere, a mean scatter of 0.03 dex is introduced to the inferred metallicity. We argue that because of this result, stellar spots should be accounted for in models of the stellar atmosphere when precise inferences of stellar metallicity are required. Finally, we discuss the intermediate period gap. We argue that there is little evidence to suggest that we do not observe stars within the gap due to a decrease in stellar activity. We propose that the gap is the result of the onset of equator-fast latitudinal differential rotation onset at the position of the intermediate period gap. Paradoxically, we show that in a synthetic sample of observed rotation periods, this introduces a bias to larger observed rotation periods resulting in the apparent dearth of observations at precise rotation periods.

This thesis provides a comprehensive review of our current knowledge about stellar rotation by synthesising a wealth of observational data, and testing hypotheses that will improve our understanding of this fundamental aspect of stars.

Declaration

This thesis is an original work of my research and contains no material which has been accepted for the award of any other degree or diploma at any university or equivalent institution and that, to the best of my knowledge and belief, this thesis contains no material previously published or written by another person, except where due reference is made in the text of the thesis.

Signature:

Print Name: Tanner A. Wilson

Date:

Thesis including published works declaration

I, Tanner Wilson, hereby declare that this thesis contains no material which has been accepted for the award of any other degree or diploma at any university or equivalent institution and that, to the best of my knowledge and belief, this thesis contains no material previously published or written by another person, except where due reference is made in the text of the thesis. This thesis includes two original papers published in peer-reviewed journals. These papers are provided in Chapters 2 and 3. The ideas, development and writing up of all the papers in the thesis were the principal responsibility of myself, the student, working under the supervision of Associate Professor Andrew R. Casey and Professor Ilya Mandel. I, the student, working within the School of Physics and Astronomy under the supervision of Associate Professor Andrew R. Casey and Professor Ilya Mandel, played a majority role in contributing to the papers constituting Chapters 2-3. My contributions to the papers presented in Chapters 2-3 constitute the majority of the work required for these projects to be published.

The inclusion of co-authors reflects the fact that the work came from active collaboration between researchers and acknowledges input into team-based research. Peer-reviewed works are presented in this thesis in their original published form as required by the Monash Graduate Research Office. Finally, I have not renumbered sections or page numbers of submitted and published papers in order to generate a consistent presentation within the thesis.

Name: Tanner Wilson

Date: September 2023

Signature:

I, Andrew Casey, hereby certify that the above declaration correctly reflects the nature and extent of the student's and co-authors' contributions to this work. In instances where I am not the responsible author, I have consulted with the responsible author to agree on the respective contributions of the authors.

Name: Andrew Casey

Date: September 2023

Signature:

Publications during enrolment

Below is a list of first author publications produced during enrolment.

- [Wilson, Casey, Mandel, Ball, Bellinger & Davies \(2023\)](#)
- [Wilson & Casey \(2023\)](#)

Acknowledgements

It is genuinely surprising that I am writing this section at the end of a long but rewarding three and a half years. I know exactly when I was set on this path towards a PhD in Astrophysics. I was in year 10 at Bendigo South East Secondary College, attending a VCE information evening, deciding what my units would be in year 11. Previous to that night, I thought I wanted to teach music. That night, I decided to do Gen B mathematics, the precursor to Specialist Mathematics. I'm unsure why I chose to do this unit; maybe I thought maths was fun(?) I now realise I was a correct intuition on my behalf, but as a 15-year-old, I had no idea what maths really was, to be honest. That decision to pursue science over the arts, and some fantastic physics and maths teachers in years 11 and 12 (shoutout to Mark and Luigi), pushed me to fall in love with physics and astronomy and follow my passion at Monash University, where I studied a Bachelor of Science and majored in Physics and Astronomy.

Over the next 4 years, I met many amazing and passionate students, including every member of the Monash Advanced Science and Science Scholar Society, who, through my competitive streak, pushed me to work as hard as possible. I would like to mention Alex Heger and Amanda Karakas, who let me, as an undergraduate student, complete projects with them and gave me my first taste of what it means to research. Alex, you also took me on as a student in my Honours year, allowed me to learn and grow in my early academic career and pushed me to achieve the grades required to enter the post-graduate program at Monash. Thank you.

To my supervisor, Andy: you are one of the most intelligent people I have ever met. I want to thank you for allowing me to be your student. Your advice and expectations have pushed me to become and improve myself as a scientist over the past 3 years. I will never forget the lessons you have taught me. Looking back over some of my early work, it is night and day, and I wouldn't have been able to do any of this without you. So, next time, the beer is on me.

To Ilya: thank you for always being there to talk about anything. From the impact of Supernovae on binaries to Shakespeare and Russian Poetry, you were always ready to talk about anything. I will never forget your advice when I met you in your office once when I was worried about something about my research: "We aren't curing cancer". I interpreted this as "it's supposed to be fun". I really appreciate the irony of that memory as I, for the life of me, cannot remember what I was worried about. Yet, your quote is always in my mind while I work.

I want to give a special shoutout to the Low-mass stellar group. Our weekly meetings have made me learn so much, especially how to communicate my science. I have loved learning about the amazing work you all do weekly.

To all of my many office mates over the past three years, despite not being able to be in the office for nearly two of those years. Thank you for always being down for a chat. Special shoutout to

Giulia, Maddy and Avi, who have pushed me to be a better scientist and whom I am grateful to call my friends.

To my best friends Isaac and Tom: you will always be my rock. When I am down and stressed, I can always turn to you for advice or a quick laugh. I appreciate everything that you do for me. Thank you, Tom and Kit, for letting me move in with you when I had no other options (bloody covid). You helped me get through the long days, and I'll always be so thankful for you.

I would also like to thank my parents. Mum and Dad, thank you for supporting me and allowing me to explore and work as hard as possible to complete this. I could not have done this without your support and love. To my brothers Jordan and Riley: I appreciate you being a part of my life and supporting whatever I do.

To my partner Hannah: I'm so glad I met you. Thank you for putting up with the long nights and the partial breakdowns and making me remember what this all means. I love you.

Finally, I have to thank my dog, Spencer, who, while writing, is behind me snoring.

This research was supported by an Australian Government Research Training Program (RTP) Scholarship.

Contents

Copyright notice	i
Abstract	ii
Declaration	iii
Thesis including published works declaration	iv
Publications during enrolment	v
Acknowledgements	vi
List of Figures	x
List of Tables	xiii
1 Introduction	1
1.1 An introduction to the observation of stellar rotation	2
1.1.1 Classical and modern observations of rotation	2
1.2 Evolution of Rotation	9
1.2.1 From birth to the terminal age main-sequence	9
1.2.2 Post-main-sequence	18
1.2.3 Effects of rotation on low-mass evolution	29
2 Constraining the Rotation Profile in a Low-Luminosity Subgiant with a Surface Rotation Measurement	33
2.1 Introduction	35
2.2 Method and results	37
2.2.1 Rotational splittings	37
2.2.2 Forward model	38
2.3 Results	40
2.3.1 Mock data experiments with three hypothetical rotation profiles	40
2.3.2 KIC 12508433	44
2.4 Discussion	46
2.5 Conclusions	48
3 Stellar spots cause measurable variations in atmospheric metallicity	52
3.1 Introduction	53
3.2 Method	55

3.2.1	Stellar parameters for a population of fake stars	55
3.2.2	Spotted spectrum generative model	56
3.3	Results	58
3.4	Discussion	61
3.4.1	Imperfect models	63
3.4.2	When should a spotted model of the stellar atmosphere be employed?	65
3.5	Conclusions	66
4	The effect of Rossby number dependent latitudinal differential rotation on the observed rotation period distribution	67
4.1	Introduction	68
4.2	Methods	73
4.2.1	Generative model	73
4.2.2	A physically motivated synthetic sample of observed rotation periods	78
4.3	Results	82
4.4	Discussion	85
4.5	Conclusions	89
5	Summary, Conclusions and Future Work	90
5.1	Summary	90
5.2	Conclusions	91
5.3	Future Work	92
5.3.1	Applications of our work	92
5.3.2	The future of asteroseismology and observation of stellar rotation through photometric modulation	94
A	An investigation into the evidence for current explanations of the intermediate period gap	96
A.1	Introduction	96
A.2	The gap aligns with a minima in photometric variability	100
A.3	The gap aligns with a minima in $\log R_{\text{HK}}^+$	106
A.4	Is there a sample of low-magnetic activity stars without rotational period detection?	109
A.5	The lack of observation of stars that could fill the intermediate period gap	113
A.6	Summary and discussion	116
A.7	Conclusion	119

List of Figures

1.1	1- σ contours of <i>Kepler</i> (blue), <i>ZTF</i> (green), and <i>Gaia DR3</i> (orange) rotation period distributions kernel density estimates.	5
1.2	Angular rotation rate distributions of low-mass young open clusters and the Sun over time.	10
1.3	Cluster rotation periods against effective temperature.	11
1.4	The rotation period distribution of the McQuillan et al. (2014) sample highlighting the intermediate period gap and long-period pile-up.	14
1.5	Rotation period distribution including fully convective stars.	16
1.6	Qualitative core and surface rotation rates of post-main-sequence stars.	19
1.7	A comparison of modelled and observed core to surface rotation rate ratios of post-main-sequence stars without additional angular momentum transport.	21
1.8	A comparison of modelled and observed core to surface rotation rate ratios of post-main-sequence stars with additional angular momentum transport.	22
1.9	Average core rotation rates of red giants against mixed mode density without additional angular momentum transport.	23
1.10	Average core rotation rates of red giants against mixed mode density without additional angular momentum transport.	24
1.11	Surface rotation period distribution of subgiant stars.	26
1.12	Surface rotation period distribution of red giant stars.	27
1.13	Effect of rotation on pre-main-sequence evolution of a $1 M_{\odot}$ star.	30
1.14	Effect of rotation of main-sequence evoltuon of a stars $1 M_{\odot}$	31
2.1	Rotational kernels for the best-fitting model of KIC 12508433.	39
2.2	Three rotation profiles used in the mock data experiments.	42
2.3	Normalised posterior density following sampling for each <i>mock</i> rotational splitting experiment.	43
2.4	Posterior distributions of core rotation rate Ω_c , the surface rotation rate Ω_s , and the discontinuity position p given the observed $l = \{1,2\}$ rotational splittings of KIC 12508433 and assuming a rotation profile with a step function.	44
2.5	Posteriors on step profile parameters given the rotational splittings of KIC 12508433 and informed prior on surface rotation rate from (Garcia et al., 2014).	45
2.6	Posterior distributions using mock data generated with a step function aligned with the H burning shell ($r/R = 0.05$, purple profile in Figure 2.2). True values are indicated in purple. There is considerable multi-modality and degeneracy present.	49
2.7	Posterior distributions using mock data generated with a step function in the radiative region ($r/R = 0.2$, blue profile in Figure 2.2) and realistic uncertainties. True values in blue.	49

2.8	Posterior distributions using mock data generated with a step function at the BCZ ($r/R = 0.5$; red profile in Figure 2.2), and realistic uncertainties. True values in red.	50
2.9	Posterior distributions using mock data generated with a step profile at the g-mode cavity ($r/R = 0.05$; purple profile in Figure 2.2), with realistic uncertainties, and a 10% prior on surface rotation Ω_s . There is still degeneracy between p and the rotation parameters (e.g., Figure 2.6), but the prior has collapsed all other modes.	50
2.10	Posterior distributions using mock data generated with a step profile in the radiative region ($r/R = 0.20$; blue profile in Figure 2.2), with realistic uncertainties, and a 10% prior on surface rotation Ω_s (compare with Figure 2.7).	51
2.11	Posterior distributions using mock data generated with a step profile at the BCZ ($r/R = 0.50$; red profile in Figure 2.2), with realistic uncertainties, and a 10% prior on surface rotation Ω_s (compare with Figure 2.8).	51
3.1	HR diagram of the 1500 sets of stellar parameters drawn from physically motivated distributions of mass, metallicity and age coloured by [Fe/H].	57
3.2	Recovered traditional stellar parameters (T_{eff} , $\log g$, [Fe/H] and $v \sin i$) from fitting synthetic spotted spectra with a spotted model of the stellar atmosphere against the corresponding injected parameters.	59
3.3	Recovered spot parameters from the synthetic spotted spectra fitted with a spotted model of the stellar spectra against the injected parameters of the synthetic spectra.	60
3.4	The difference between the recovered traditional stellar spectra parameters (T_{eff} , $\log g$, [Fe/H] and $v \sin i$) from the synthetic spotted spectra fitted with both a spotted and non-spotted model of the stellar spectra against the injected parameters of the synthetic spectra.	61
3.5	Bias introduced to T_{eff} when fitting spotted spectra with a non-spotted model against injected parameters of synthetic spectra.	62
3.6	Bias introduced to $\log g$ (orange), [Fe/H] (green) and $\log v \sin i$ (red) when fitting spotted spectra with a non-spotted model against injected parameters of synthetic spectra.	63
3.7	Bias introduced to [Fe/H] when fitting spotted spectra with a non-spotted model against the age of the model used to generate synthetic spectra.	64
4.1	The rotation period distribution of the (McQuillan et al., 2014) sample highlighting the features of the intermediate period gap.	69
4.2	The relationships between latitudinal differential rotation and the stellar R_o adopted in this work.	75
4.3	The effect of the differential rotation on the observed rotation period of a $0.7 M_\odot$ against equatorial rotation period.	77
4.4	The effect of differential rotation on the observed rotation period distribution.	79
4.5	Cluster rotation periods distributions against effective temperature.	81
4.6	The observed rotation period distributions of the synthetic sample of stars given various relations between latitudinal differential rotation and R_o overlayed over the distribution of measured rotation periods of the <i>Kepler</i> sample from McQuillan et al. (2014).	83

4.7	2D histograms of measured and the synthetic observed rotation period distribution assuming various relations between the scale of differential rotation and R_o and the difference between the two.	84
4.8	A comparison between the effective temperature and luminosity distributions of the McQuillan et al. (2014) and synthetic sample adopted in this work.	87
A.1	Colour-magnitude diagram of the closeby rotating main-sequence sample colours by photometric variability (R_{per}).	100
A.2	\log_{10} of the rotation period against <i>Gaia DR3</i> $B_P - R_P$ colour of the closeby rotating main-sequence sample colours by photometric variability (R_{per}).	101
A.3	2D binned photometric variability (R_{per}) for the slices of \log_{10} of the rotation period and colour <i>Gaia</i> $B_P - R_P$ used in this work.	102
A.4	Median and median absolute deviation of photometric variability (R_{per}) against \log_{10} of the rotation period in bins of and colour <i>Gaia</i> $B_P - R_P$	103
A.5	The position of the identified minima in R_{per} against rotational period using the full close-by rotating main-sequence <i>Kepler</i> sample, the R_{per} minima identified with the <i>Kepler-LAMOST</i> crossmatch and the $\log_{10} R_{H,K}^+$ minima identified with the <i>Kepler LAMOST</i> crossmatch.	104
A.6	Median and median absolute deviation of photometric variability (R_{per}) (blue) and $B_P - R_P$ (orange) against \log_{10} of the rotation period in bins of and <i>Gaia</i> $B_P - R_P$ colour.	105
A.7	The <i>LAMOST</i> chromospherically active and <i>Kepler</i> rotating closeby, main-sequence cross-match \log_{10} of rotational period \log_{10} against <i>Gaia</i> $B_P - R_P$ colour coloured by $\log_{10} R_{HK}^+$	107
A.8	Median and median absolute deviation of photometric variability (R_{per}) (blue) and <i>LAMOST</i> $\log_{10} R_{HK}^+$ against \log_{10} of the rotation period in bins of and colour <i>Gaia</i> $B_P - R_P$	108
A.9	HR diagram of the closeby rotating (top) and non-rotating (bottom) main-sequence sample crossmatched with the <i>Kepler-LAMOST</i> field coloured by the chromospheric magnetic activity indicator $\log R_{HK}^+$	110
A.10	The probability density function (left) and cumulative probability density function (right) of $\log R_{HK}^+$ are separated by whether rotation was (blue) or was not (orange) detected in the close-by main-sequence <i>Kepler-LAMOST</i> crossmatch.	111
A.11	The detectability of rotation (top) and 2D histogram of stars without detected rotation periods (bottom) across <i>Gaia</i> $B_P - R_P$ colour and $\log R_{HK}^+$	112
A.12	A histogram of the distribution of $B_P - R_P$ colour of stars with (green) and without (red) detected rotation periods.	114
A.13	Number of stars in each bin against \log_{10} of the rotation period in bins of colour <i>Gaia</i> $B_P - R_P$	115
A.14	The number of stars required to fill the gap (black scatter points) against the number of stars with undetected rotation periods against $B_P - R_P$	116

List of Tables

2.1	Measured properties and best-fit stellar model parameters of KIC 12508433. . .	39
2.2	Best-fitting rotation profile parameters given observed $\ell = 1$ and 2 rotational splittings of KIC 12508433 from optimally localised averages (OLA) (Deheuvels et al., 2014) and forward modelling with flat and informed ($\Omega_s/2\pi = 172 \pm 21$ nHz) priors.	45

Chapter 1

Introduction

Humans have been captivated by the stars since the dawn of civilisation, and this fascination has driven our curiosity to understand the universe around us. The history of astronomy is rich and diverse. Indigenous cultures still use the stars for navigation, seasonal calendars, and mythological stories. From the invention of the modern telescope in the 16th century, some would say the birth of modern astronomy, to the launch of the James Webb Space Telescope, the scale and sophistication of technology has advanced and enhanced our ability to observe and study the stars.

Each observation that we make improves our understanding of the underlying physics of the universe. In recent years the sheer amount of data available to astronomers has increased dramatically due in part to technological advances, such as space-based observatories, which allow us to perform large sky surveys in unprecedented detail. It is clear from these studies that our models of the universe are lacking in a number of important physical processes. One of these physical processes that is particularly not well understood is the evolution of stellar rotation¹.

This introductory chapter is intended to provide context for the reader to understand the following science chapters. The introductory chapter is broken down into the following sections of increasing level of detail: Section 1.1 provides a historical and modern overview of the astronomical observation of rotation and introduces the techniques used to observe the stellar rotation. Section 1.2 reviews our current understanding of the evolution of rotation from birth, through post-main-sequence evolution, to the remnants of rotating stars. Within this Section we² also describe what we call the “problems of stellar rotation” that we have attempted to address in this work. We also briefly describe in this section the effects of the rotation of the evolution of low-mass stars.

¹Most models of stellar evolution completely ignore angular momentum transport.

²For stylistic reason I use the word “we” to describe work that I have led in collaboration with others.

The scientific works in this thesis are motivated by the problems in stellar rotation that are described in detail in this introduction. As a result, this introduction will overlap with the introductions of the scientific works' topics and serve as a companion for readers unfamiliar with the topic.

1.1 An introduction to the observation of stellar rotation

1.1.1 Classical and modern observations of rotation

In this section, we look back at the history of observing stellar rotation, describe how observations of stellar rotation are performed, and describe modern missions that have resulted in the recent big-data boom of stellar rotational astronomy. This discussion will provide the necessary background to our attempts to understand and constrain the astrophysical process that underlie these problems.

The history of observing the rotating stars began with observations of the Sun³. In approximately 1610, Galileo reported evidence of sunspots and tracked their motion in his book “*L’Istoria e dimostrazioni intorno alle macchie solari e loro accidenti*”. He interpreted the motion of stellar spots on the surface of the Sun as a result of its rotation. Adding onto this work in 1630, Christoph Scheiner found that the stellar spots had different rotation periods at the poles and the equator, measurements that agree with modern observations of the Sun. This was the first observation of latitude-dependent rotation, more commonly known as latitudinal differential rotation.

The history of observing stellar⁴ rotation can be traced back to the early 20th century when astronomers first discovered that some stars they observed were rotating. They came to this conclusion through spectroscopic observations ([Elvey, 1929](#); [Struve & Elvey, 1930](#); [Struve, 1930](#)). They found that lines in their spectra were broadened due to the Doppler effect, a technique used to this day. The broadening of spectral absorption lines provides a measure of the equatorial velocity of the star multiplied by the sine of the inclination angle ($v \sin i$). While spectroscopic rotational velocities have been inferred for orders of magnitude more stars than other techniques that we will discuss in this section, the observed rotation rate is modulated by the unknown inclination angle of the star relative to the observer. Constraining the evolution of rotation through spectroscopic rotational velocities of stars is only fruitful with independent constraints to stellar inclination. The stellar inclination is often difficult to measure as it requires either that the star

³As most astronomy does.

⁴Here we make the distinction between the Sun and other stars through the use of the terms “solar” and “stellar” respectively.

is in a binary⁵ or that the star is intensively asteroseismically studied. As a result, only a few studies of the evolution of rotation rely on this data.

Around this time, astrophysicists such as Eddington (Eddington, 1918, 1926, 1929), Milne (Milne, 1923), von Zeipel (von Zeipel, 1924), and others delved into the theoretical aspects of the impact of rotation on stars. To simplify their work, they identified the effects of rotation on stellar structure, energy generation, shape and luminosity. They argued that rotation induces mixing that could transport material in stars, leading to enhanced chemical mixing and angular momentum transport. Advances in computational capabilities allowed astronomers to study the impact of rotation on the mixing of elements within stars in greater detail. Enhanced mixing leads to an increased lifetime on the main-sequence through the transport of hydrogen-rich material to the core, and can create isotope anomalies, such as changes in the isotopic ratio $^{12}\text{C}/^{13}\text{C}$, as well as nitrogen, oxygen and lithium enhancements (Maeder & Meynet, 2000; Heger et al., 2000; Charbonnel et al., 1994). Their results underlay our modern understanding of the impacts of rotation on stellar evolution.

Like the Sun, stars exhibit magnetically active regions⁶. In this work, we will refer to these active regions as stellar spots, however, it should be noted that an active region is composed of two distinct regions: the cool, darker spots and the hot, bright faculae that surround them. Stellar spots are regions of intense magnetic activity on a star's surface from magnetic flux tubes in the convection zone. These flux tubes are thought to be stretched and curled by the differential rotation of the convective region. As a result, convection is inhibited, limiting plasma flow to the surface in these tubes. This results in lower-temperature material within the tube, which looks like a darker spot on the star's surface.

Stellar spots are extremely difficult to image on the surface of stars other than the Sun. However, rotational modulation of magnetically active regions on the surfaces of stars produce quasi-periodic⁷ variations in the disk-integrated flux, generally through magnitude variations due to induced brightness variations from stellar spots. Measuring the period of brightness variation is used as a proxy for the rotation period⁸. However, measuring rotation periods is not straightforward due to the transient nature of stellar spots and the unpredictable recurrence of their signals. While it is commonly accepted that active regions mainly manifest as dim spots, their finite lifetimes and stochastic appearance make it challenging to precisely measure their periods.

⁵This itself relies on the assumption the rotation axis aligns itself with the binary orbital inclination, which may not always be the case (Albrecht et al., 2011, 2013).

⁶Magnetically active regions can have varying effects on the flux of stars. Those regions can be brighter (faculae), darker (spots) and induce emission in strong lines (e.g., Ca II H & K and H α).

⁷Here we will use quasi-periodic and periodic interchangeably though these are distinct terms. Quasi-periodic is more accurate to the signal here. Stellar spots are not constant features on the surface of stars: they have finite lifetimes and stochastically appear on the surfaces of stars. The recurrence of the signal has a component of unpredictability that does not lend itself to precise measurement.

⁸It is important to note here that the rotation period (time taken for one rotation) and rotation rate (frequency of rotation) of a star are not the same quantity. They are inversely related.

Unlike the spectroscopic technique – where the inclination angle modulates the rotation rate – the surface rotation periods from stellar spot brightness modulations are more accurate to the star’s actual rotation rate. In this thesis, we will investigate the impact of latitudinal differential rotation on the observed rotation period of stars. As such we adopt the “surface rotation period” as the average rotation period when spots are present on a star.

To measure the surface rotation periods using these variations, we face a signal-processing problem that involves employing various techniques. The first step is to acquire precise time-series photometry, generating the light curve that represents the brightness variations of the star over time. Before analysing the light curve for periodic variability, data preprocessing is essential to remove systematic effects and correct instrumental noise. Without proper preprocessing, systematic effects on the timescale of low-mass main-sequence rotation periods could be mistaken for genuine signals. Once the light curve is preprocessed, the analysis of periodic signals can take various forms, each offering its unique advantages. Different signal processing techniques are adopted to identify and characterise the periodic variability in the light curve, leading to the determination of rotation periods for the stars under investigation: Lomb-Scargle periodograms (see, e.g., [Lomb, 1976](#); [Scargle, 1982](#); [Mottola et al., 1995](#); [Scott et al., 1992](#); [Reinhold & Reiners, 2013](#); [Reinhold et al., 2013](#)), auto-correlation functions (see, e.g., [Aigrain et al., 2008](#); [Garcia et al., 2014](#); [McQuillan et al., 2014](#)), wavelet transforms (see, e.g., [Garcia et al., 2014](#)), gaussian processes (see, e.g., [Angus et al., 2017](#)), and machine learning (see, e.g., [Claytor et al., 2022](#)). Each come with their own benefits and drawbacks as described more thoroughly in the referenced works.

In order to measure the surface rotation period of stars we need to begin by measuring its time-series flux. Early works relied on ground-based time-domain photometric surveys. These works yielded numerous rotation period measurements for stars in young clusters. However, the limited precision of the telescopes and low cadence of time-sampling achievable from the ground are insufficient to detect rotational modulation in older, less active stars. For many years, the Mount Wilson⁹ program monitored the emission in the cores of the Ca II H & K lines for a large number of low-mass stars over a 20-year period ([Wilson, 1963](#)). The cadence of observations was on the order of days and resultingly became the main source of rotation period measurements for field stars. This changed with the advent of space-based photometric missions such as *CoRoT* (CONvection, ROtation and planetary Transits; [Baglin, 2003](#)), *Kepler* ([Borucki et al., 2010](#); [Howell et al., 2014](#)), *TESS* (Transiting Exoplanet Survey Satellite; [Ricker et al., 2014](#)), and *Gaia* ([Distefano et al., 2023](#)) as well as with long-cadence observations of nearby stars through ground-based facilities such as (ZTF) (the Zwicky Transient Facility; [Lu et al., 2022](#)). These missions have collectively gathered sub-millimag precision photometry with short-cadence observations (time scales between observations on the scale of minutes) over baselines from months to years,

⁹No relation.

which have resulted in the largest high-precision catalogues of rotation periods of low-mass main-sequence stars available.

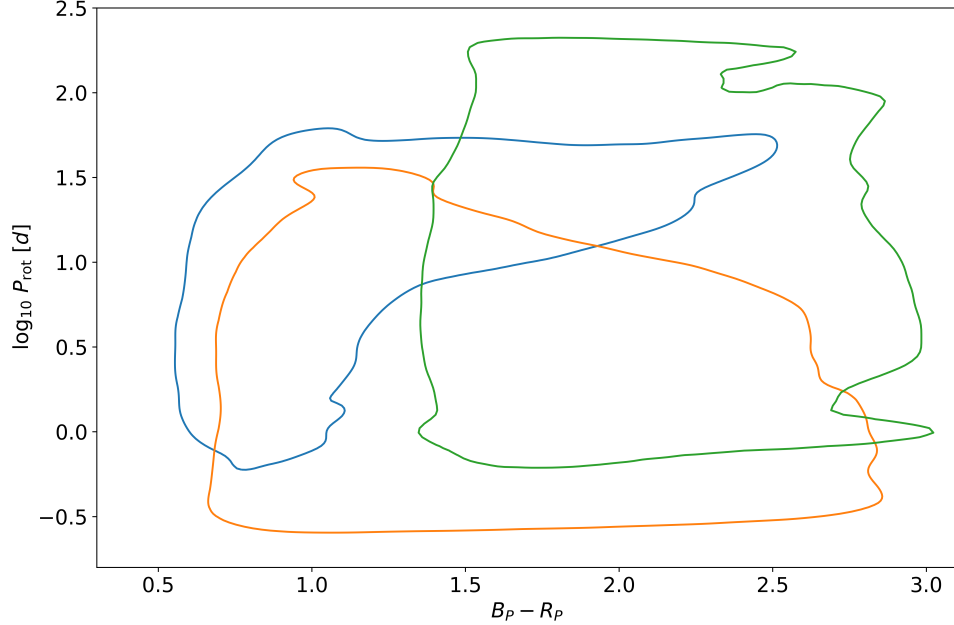


FIGURE 1.1: $1-\sigma$ contours of *Kepler* (blue) (McQuillan et al., 2014), *ZTF* (green) (Lu et al., 2022), and *Gaia DR3* (Distefano et al., 2023) (orange) rotation period distributions computed using kernel density estimation. Each sample probes a different area of the rotation period against colour space with some overlap. This expands our knowledge of the evolution of rotation to different types of stars. Their agreement in overlapping regions of the rotation period distribution also confirms their independent accuracy.

The stellar spot rotation periods obtained from different missions are suited to observe particular masses and rotation period regimes along the main-sequence. To highlight this we show the rotation period distribution against colour (*Gaia DR3* $B_P - R_P$) of the representative *Kepler*, *ZTF* and *Gaia DR3* rotation period samples in blue, green and orange in Figure 1.1 respectively. This results from the underlying telescope parameters, each mission’s observation cadences (Distefano et al., 2012), and, in the case of *Gaia*, the scanning technique employed. Comparing the rotation period distributions in Figure 1.1 we observe a few notable features and limitations from each mission. For example, before post-processing the *Gaia DR3* rotation period sample shows spurious periods centred around 0.5, 18, 25, 32 and 49d (compare Figures 17, 18 and 19. in Distefano et al. (2023)) due to the non-uniformity of *Gaia* sampling. Period detections at these periods, or at fundamental over and undertones, should be treated with caution. Another example comes in the form of the *Kepler* instrument’s temperature changes, which can produce periodic variability with a period of approximately 10 days, falling within the range of rotation periods of young low-mass main-sequence stellar rotators. Rotation period observations close to this period should therefore also be treated with caution.

Different missions can also have different selection functions depending on their intended science goals. *Kepler* mainly targeted solar-like, relatively higher mass ($M \sim M_{\odot}$), stars. As a result, in the *Kepler* sample, there is a lack of measured periods for M dwarfs and fast-rotating young stars. The *ZTF* and *Gaia* samples did not have this targeting bias and have a non-specific untargeted approach and thus probe the rotation periods of the comparatively lower-mass (redder) stars.

Due to the *Kepler* mission’s long baseline, but usually long-cadence data, it is biased towards the observation of long periods ($P > 10$ d). The *Gaia DR3* rotation sample is, as a result of the *Gaia* scanning law, mostly suited to detect periods of rapidly rotating stars ($P < 5$ d) (Distefano et al., 2023). Due to the long observation baseline, the *ZTF* mission was more suited to observe longer rotation periods. Combining the results of these missions, we can accurately probe the evolution of rotation along the main-sequence for a wider range of stellar parameters than the individual missions permit.

Most of what we know about main-sequence stellar rotational evolution arises from measuring stellar spot rotation periods. However, the technique is limited by the requirement for stars to express stellar spots to be effective: a limitation that is invoked several times to explain phenomena discussed later in this Chapter. McQuillan et al. (2014) attempted to measure the stellar spot rotation periods of solar-like stars in the *Kepler* sample. In this work, they recovered the rotation period of 20% of stars with long cadence observations: 34,000 detected rotation periods out of 133,000 selected stars in the sample. On the other hand, Distefano et al. (2023) places the efficiency of the *Gaia DR3* period detection pipeline at $\sim 0.4\%$. They argue that the detection efficiency is non-constant and, in fact, a function of stellar magnitude, the amplitude of the rotational modulation, the stellar rotation period, and the ecliptic latitude. There may be regions of stellar evolution where the stellar spot rotation period does not effectively probe rotational evolution.

Determining the rotation period of a star from stellar spots requires intermittent photometric measurements of stars, known as long-cadence observations, over the time scale of months. On the other hand, measurements with cadences on the order of minutes, known as short-cadence observations, and baselines on the order of years, reveal the internal structure of stars. Stars pulsate, and thus vary in brightness, at particular frequencies related to the structure of the star. The measurement and study of these pulsations is known as asteroseismology (see, e.g., Christensen-Dalsgaard & Gough, 1982; Christensen-Dalsgaard et al., 1990; Aerts et al., 2010; Basu & Chaplin, 2017, for thorough overviews) We can separate the observed frequencies, or modes, of stars into distinct flavours: pressure (p) modes, gravity (g) modes, and mixed modes. p- and g-modes correspond to oscillations propagating in the convective envelope, and the result of trapping of gravity waves in the radiative core with buoyancy as a restoring force, respectively. During the main-sequence, g-modes are trapped within the radiative core and thus

do not introduce brightness variations (oscillations) to the stellar surface. Some g-modes can couple with p-modes in the surface convective cavity during the post-main-sequence and are known as “mixed modes”. Where, precisely, the mixed modes probe is dependent on where in the post-main-sequence the star is observed. For example, subgiant stars express p-modes and mixed modes that can probe both the core and the surface, whereas red giant branch (RGB) stars mainly express mixed modes that can only probe the star’s core.

An oscillation mode, v , is described by its radial number, n , degree ℓ , and the azimuthal order, m . The azimuthal order, m , is relevant when rotation and/or magnetic fields break spherical symmetry. Rotation breaks an oscillation into $2\ell+1$ modes, $m = (-\ell, -\ell+1, \dots, 0, \dots, \ell-1, \ell)$. We are only able to observe low-degree oscillations $\ell < 3$ due to the relatively low amplitude of $\ell > 3$ integrated surface flux variations. Current observations of stars, therefore, only yield the radial ($l = 0$), dipole ($l = 1$) and quadrupole ($l = 2$) modes with the latter two being those relevant to rotational observations (Basu & Chaplin, 2017). The difference in the frequency of $m = 0$ and $m = 1$ or -1 modes are known as the rotational splitting (δv). The rotational splitting is dependent on the rotation rate of a star in the cavity that the mode naturally oscillates and therefore the rotational splittings of the mixed modes allow us to infer the rotation rate in the radiative region and deep core (Metcalfe et al., 2010; Bedding et al., 2011). The frequencies of rotationally split modes are given by

$$v_{nlm} = v_{nl} + m\delta v = v_{nl} + m\beta_{n,l} \int_0^R K_{nl}(r)\Omega(r)dr \quad (1.1)$$

where $K_{nl}(r)$ is known as the rotational kernel, R is the radius of the star, $\Omega(r)$ is the rotation profile of a star, and β_{nl} is a mode inertia dependent scaling (Hansen et al., 1977; Gough, 1981). $\beta_{n,l}$ and $K_{n,l}(r)$ depend on the structure of the star and are set using a 1-D model. The rotational splitting of a mode can be therefore thought of as a weighted average of the rotational profile dependent on the rotational kernel, or rather the structure of the star. Here we have assumed a 1D rotation profile for a star, dependent only on radius. For meaningful inference of the latitudinal differential rotation, a large number of observed rotational splittings are required. Latitudinal dependence has therefore only been probed in the Sun and a small number of Solar twins (Benomar et al., 2018). The effects of latitudinal differential rotation can be shown to be a 2nd order effect on the rotational splittings, therefore they have little effect on the inference of the radial rotational profile of a star (Gough & Thompson, 1990; Gough & Toomre, 1991; Gough et al., 1996).

Determining the rotation profile of a star using the observed rotational splittings is nontrivial. The rotation profile is convolved with the rotation kernels and the number of observed rotational splittings is finite. One of the critical challenges in asteroseismic inversions is to extract meaningful information from the limited set of observed oscillation frequencies. Inference of parts

of the rotation profile is possible¹⁰. State-of-the-art methods involve the use of linear inversion techniques, regularised least-squares fitting and forward modelling (see, e.g., Christensen-Dalsgaard et al., 1990, 1993; Aerts et al., 2010, for thorough discussion of these techniques).

Owing to the required long baseline and short-cadence of data to perform asteroseismology we have only been able to probe asteroseismic rotation recently through the *Kepler* and *K2* missions. In the *Kepler* field, the cross-section of stars with both short-cadence observations and those with observation periods long enough to obtain a high enough signal-to-noise to perform asteroseismic inference does not include a large number of stars. On the other hand, *K2* did not provide long enough baseline observations of stars to rigorously measure the rotation splittings of any stars.

Only limited constraints can be placed on the surface rotation rate from asteroseismology during the main-sequence. Main-sequence stars only express p-mode solar-like oscillations with long mode-lifetimes, which can only probe the structure of the convective surface region. Long mode lifetimes result in broadened oscillation peaks in the power spectrum. Stars also spend the majority of their main-sequence lifetime slowly rotating. This results in rotational broadenings of the oscillations rather than distinct rotational splittings. Without precise measurements of the rotational splittings for many oscillation modes, precise inference of the surface rotation rate is limited.

The inefficiency of asteroseismic inference of rotation rates along the main-sequence is best exhibited in Hall et al. (2021), who measured the asteroseismic surface rotation rates of 91 stars. Figure 2 in Hall et al. (2021) compares the stellar spot rotation period with the surface rotation period from asteroseismic inference of the rotation profile. The surface rotation periods generally agree, confirming that the surface brightness oscillation period from stellar spots is indeed the surface rotation period. However, the rotation periods obtained from asteroseismology are much less precise than their stellar spot rotation period counterparts. Despite requiring much more data, the information provided by this technique is limited compared to stellar spot brightness modulation periods.

Asteroseismology allows us to probe the internal rotational structure of post-main-sequence stars, something we cannot otherwise do with photometric variability from stellar spots or spectroscopic line broadenings. At the time of writing the number of post-main-sequence (subgiant and RGB) stars with measured internal rotation rates is of order 100 (see, e.g., Deheuvels et al., 2014; Gehan et al., 2019; Li et al., 2020b,a; Moyano et al., 2022). The constraints to the rotation profile of stars by asteroseismology, even in the post-main-sequence, are also somewhat limited. The core and surface rotation rates of subgiants can simultaneously be probed. However, where in a star the rotation can be probed depends on the observed oscillation modes, which depend

¹⁰Here we have specifically used the term “parts”. What we can infer about the rotation profile, i.e. constraints to a region of the star or to parameters of a model, is dependent on the techniques.

on the stellar structure. The rotation rates measured by asteroseismology are kernel-based averages of the rotation profile in regions that the expressed oscillation modes probe. For example, subgiants' core and surface rotation rates are the kernel-based average rotation rates of the innermost $r/R < 0.05$ and outermost $r/R > 0.9$ regions (on average). Between these regions, the rotation profile is not constrained. As a result, the shape of the rotation profile, which can act as fingerprints of specific angular momentum transport mechanisms at play, is also not constrained. This is because: a) state-of-the-art measurements of rotational splittings are low signal-to-noise and are often also imprecise, and b) the observed rotational splittings are a finite subset of the infinite number of rotational splittings that would be required to accurately and precisely constrain the entire rotation profile.

Despite the constraints, asteroseismology has paved the way for several fundamental discoveries about the evolution of stellar rotation. Modern observations using asteroseismology¹¹, for example, have found that the Sun, and most post-main-sequence stars, exhibit differential rotation along the radial axis, known as radial differential rotation. Measurement of the rotation profile of post-main-sequence stars has allowed us to probe these stars' internal mixing and angular momentum transport.

It is through a combination of these methods: periodic variability from stellar spots, asteroseismology, and, to a certain extent, spectroscopic line broadenings, as well as recent targeted missions that we have begun to truly uncover the evolution of rotation in stars.

1.2 Evolution of Rotation

1.2.1 From birth to the terminal age main-sequence

All baryonic matter in the universe has some angular momentum. Stars are born in the core of spinning molecular clouds from the infall of matter due to gravity. As a result, all stars are rotating. The amount of angular momentum a star is born with may depend on the cloud from which it was formed.

At the beginning of the pre-main-sequence (PMS) phase, a young star is typically surrounded by a disk of gas and dust from which it is accreting material. The accretion process can increase the star's rotation rate, as the angular momentum of the infalling material is transferred to the star. However, as the star grows in size and mass, its magnetic field becomes stronger, which can slow down its rotation through the process of magnetic braking.

One key feature of PMS rotational evolution is the “disk-locking” phenomenon, in which the star's rotation becomes locked to the rotation of the disk([Eggenberger et al., 2012](#)). This occurs

¹¹As well as helioseismology for the Sun.

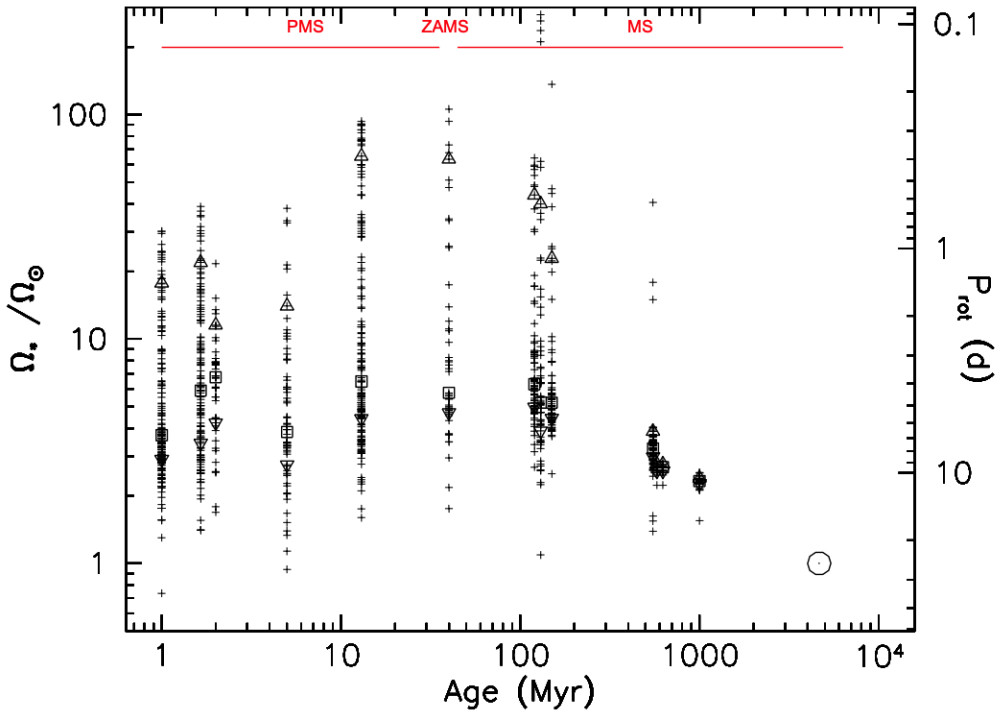


FIGURE 1.2: Angular rotation rate (relative to solar) distributions of low-mass young open clusters and the Sun. Inverted triangles, triangles, and squares represent the 25th, 50th, and 90th percentiles. Open circle denotes the present value of the rotation rate of the Sun. Median (50th percentile) values indicate that the rotation rate of cluster is approximately constant with age, despite the spin-up by accretion. In order of increasing age (left to right) the clusters are ONC (1 Myr) (Herbst et al., 2002), NGC 6530 (Henderson & Stassun, 2012), NGC 2264 (2 Myr) (Affer et al., 2013), NGC 2362 (5 Myr) (Irwin et al., 2008), h PER (13 Myr) (Moraux et al., 2013), NGC 2547 (40 Myr) (Irwin et al., 2008), Pleiades (120 Myr) (Hartman et al., 2010), M50 (130 Myr) (Irwin et al., 2009), M35 (150 Myr) (Meibom et al., 2009), M37 (550 Myr) (Hartman et al., 2009), Praesepe (700 Myr) (Delorme et al., 2011), Hyades (625 Myr) (Delorme et al., 2011), and NGC 6811 (1 Gyr) (Meibom et al., 2011). Sourced from Gallet & Bouvier (2013), Figure 1.

when the star’s magnetic field is strong enough to interact with the disc, causing the star and diskto rotate together. disk-locking can help to explain why some PMS stars have relatively long rotation periods, even though they are young and should be rotating rapidly due to the effects of accretion.

The interplay between accretion and magnetic braking can result in a complex evolution of the rotation rate of a young star during the PMS phase (Gallet & Bouvier, 2013). Observations of young stars in star-forming regions have revealed that the rotation rates of PMS stars span a wide range. We show this complex relationship in Figure 1.2. Compared to the main-sequence, where stars generally spin-down due to surface winds, the median rotation rate of PMS cluster is relatively constant with age.

The surface rotation period increases over time for stars $< 1.1 M_\odot$. Within this range of masses, angular momentum is lost from the convective surface through mass loss and interactions of

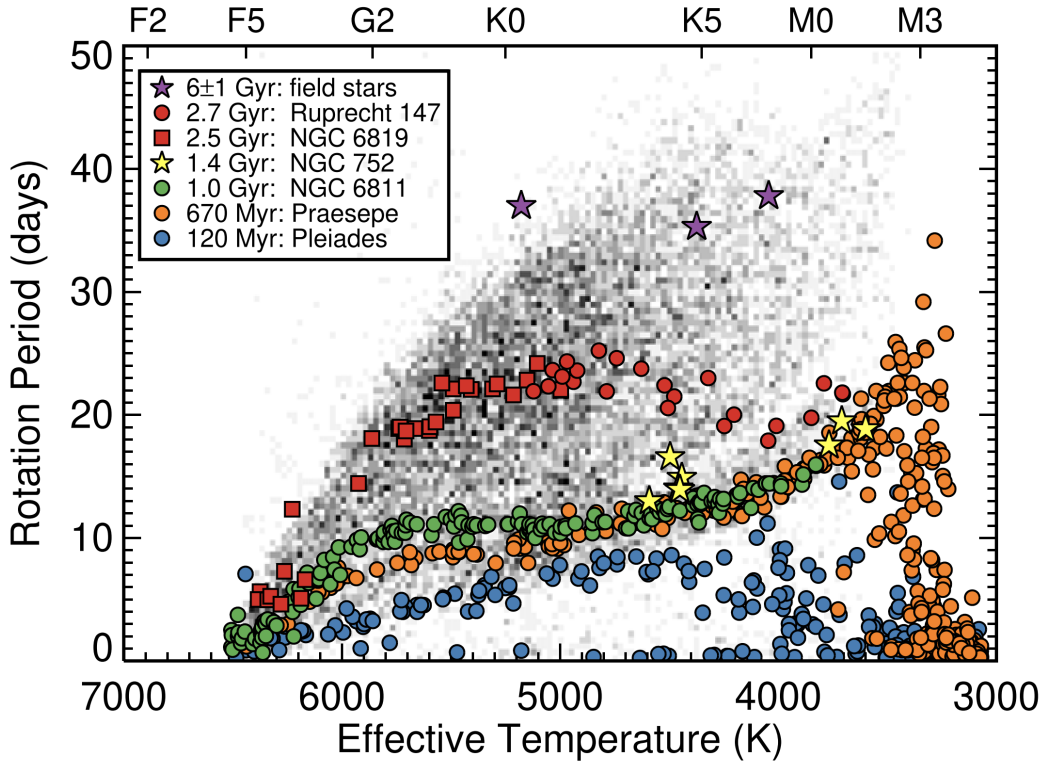


FIGURE 1.3: Scatter plot of young open clusters, Pleiades (120 Myr, blue ([Rebull et al., 2016](#))), Praesepe (orange, 700 Myr, ([Douglas et al., 2017, 2019](#))) and NGC 6811 (green, 1 Gyr, ([Curtis et al., 2019](#))), NGC 752 (yellow, 1.4 Gyr), NGC 6819 (red squares, 2.5 Gyr - projected forward to 2.7 Gyr: scaled through Skumanich spin-down, for direct comparison with the Ruprecht 147 sample, ([Meibom et al., 2011](#))), and Ruprecht 147 (red circles, 2.7 Gyr, ([Curtis et al., 2020](#))) overlayed on the *Kepler* ([McQuillan et al., 2014](#)) rotation period sample. Highlighted in this Figure is the mass dependence of the slow-rotator sequence and the commonality of the shape of rotation period distribution as set by the ascension to the slow-rotator sequence. The agreement between low-mass Praesepe and NGC6811 periods also implies mass-dependent core-envelope coupling for young (<1 Gyr) stars. Sourced from top left panel of Figure 7 in [Curtis et al. \(2020\)](#).

the star's magnetic field and the lost ionised material through stellar winds, known as magnetic braking. Through observations of the Pleiades, Ursa Major, and Hyades stars and the Sun, [Skumanich \(1972\)](#) derived the proportional relation between the rotational rate of stars and the inverse square of their age: $\Omega(t) \propto t^{-1/2}$. This relation forms the standard for expected rotational evolution and, therefore, measures the ages of stars from their rotational rate.

Outside the ~ 0.4 and $1.1 M_{\odot}$ range, the rotation period also decreases, albeit slower, with much more complex relationships with time. Above $\sim 1.1 M_{\odot}$, known as the Kraft break ([Kraft, 1967](#)), stars have shallower convective envelopes and are believed to have less efficient magnetic dynamos. Resultingly, the magnetic braking in these stars is less efficient, and these stars continue to rotate rapidly throughout most of their main-sequence lifetimes. Below $0.4 M_{\odot}$ stars are fully convective and angular momentum is efficiently transported throughout the star. A greater amount of angular momentum needs to be removed to slow the star's rotational

rate, compared to stars that are not fully convective. The main-sequence rotational evolution of stars with mass $> 1.3 M_{\odot}$ is unprobed. Above this mass, stars have no convective envelope, and thus, they do not express stellar spots nor solar-like oscillations that can be used to probe the surface rotation rate. Theoretical modelling of the rotational evolution of high-mass stars is a substantial area of research in which observations of stellar parameters such as chemical abundances must independently constrain angular momentum transport rather than observations of stellar rotation. As this work has a stronger focus on observing the rotation of stars, these results will not be discussed here. For more information, we suggest reviews of astrophysical models of high-mass stellar rotational evolution, e.g. [Heger \(1998\)](#); [Maeder & Meynet \(2000\)](#); [Maeder \(2009\)](#).

While many main-sequence stars have had their rotation rates measured, their ages are not well-constrained. As a result, the evolution of rotation with age is difficult to determine. We can marginally investigate the evolution of rotation from variances to the rotation period distributions (rotation period against effective temperature or mass) of the small number of nearby young open clusters with known ages. Observations of young open clusters' main-sequence surface rotation period from the *Kepler* mission also suggest that angular momentum transport over a star's lifetime is qualitatively consistent between clusters ([Spada & Lanzafame, 2020](#)) and a number of features can be observed by comparison between open clusters of different ages.

In the low-mass regime ($0.4 < M_{\odot} < 1.1$), young stars can be separated into two distinct categories depending on their rotation rate: stars that are still undergoing disk-locking, and those that are on the so-called “slow-rotator sequence” (see, e.g., [Lanzafame & Spada, 2015](#)). The slow-rotator sequence appears to be a common feature between the rotation distributions of young clusters: clusters of different ages reflect similar rotation period distributions, albeit modulated by angular momentum transport over time. For a young open cluster ($< 1 \text{ Gyr}$), whether a star has ascended to the slow-rotator sequence is mass-dependent, and this mass dependence sets the initial shape of the rotation period distribution. This is best illustrated by the rotation period distributions of the Pleiades (120 Myr, blue) and Praesepe (670 Myr, orange) in Figure 1.3 where a majority of high-mass stars have ascended to the slow-rotator sequence. In contrast, low-mass ($< 4500 \text{ K}$) stars have not. Further, a larger proportion of low-mass stars have ascended to the slow-rotator sequence in the older Praesepe.

Until recently it was assumed that there was little to no angular momentum transport between the radiative core and convective surface of main-sequence stars in the between $0.4 < M_{\odot} < 1.1$ range. Helioseismic observations suggest that only the solar surface undergoes rotational braking, and the core remains rotating rapidly. This suggests that minimal angular momentum transport occurs between the core and the surface during the main-sequence. [Spada & Lanzafame \(2020\)](#) proposed that mass-dependent angular momentum transport between the core and the surface was required to explain observations of young ($< 1 \text{ Gyr}$) open cluster rotation period

distributions. They compared the observations of the ~ 700 Myr old Praesepe and the 1 Gyr old NGC 6811 clusters. Comparing the rotation period distribution of the Pleiades (120 Myr), Praesepe (670 Myr), and NGC 6811 (1 Gyr) in Figure 1.3, [Spada & Lanzaflame \(2020\)](#) find that higher mass stars ($> 0.9 M_{\odot}$) that are on the slow rotator sequence of the older NGC 6811 have longer periods than their counterparts in the younger Praesepe, as Skaumanich rotational evolution suggests. On the other hand, the two clusters' rotation periods are indistinguishable at lower masses ($< 0.8 M_{\odot}$). In other words, low-mass stars have not been spinning down at all in the intervening 300 Myr. They argue that behaviour is the result of mass-dependent core-envelope coupling – angular momentum transport between the core and the surface – briefly compensating for the loss of angular momentum due to wind braking at the surface. They develop a semi-analytic model of the rotation period's evolution with a star's age and mass, tuned with the observations of stellar cluster rotation period distributions. This notably improves the accuracy of gyrochronology compared to the Skaumanich relation, especially for younger low-mass stars.

The slow spin-down rates of fast rotating stars could instead be related to saturation of the angular momentum loss due to stellar winds ([Johnstone et al., 2015b,a](#); [Gallet & Bouvier, 2013](#)). This is motivated by the saturation of magnetic field indicators for fast rotation rates, or, rather, low Rossby numbers ([Wright et al., 2011](#)). This could explain the slower observed spin-down of young, rapidly rotating stars. Both of these prescriptions neglect each other: [Spada & Lanzaflame \(2020\)](#) includes a simple stellar wind prescription that does not consider the saturated regime, while [Gallet & Bouvier \(2013\)](#) does not consider mass-dependent angular momentum transport within the star.

Another phenomenon not well explained by Skaumanich-like rotational evolution is the observed intermediate period gap. [McQuillan et al. \(2014\)](#) calculated the rotation periods of $\sim 30,000$ stars in the *Kepler* sample from photometric oscillations of surface brightness from stellar spots. The distribution of the logarithm of the rotation periods from this sample against colour is shown in Figure 1.4. Following increasing rotation period as a proxy for time, this Figure highlights the overabundance of observations followed, temporally, by a dearth of observations of particular rotation periods, the position of which varies with mass.

It is worth identifying where the rotation period gap occurs with respect to stellar evolution. [Reinhold et al. \(2019\)](#) first suggested that the gap aligns with isochrone at ~ 800 Myr using [Barnes \(2010\)](#) gyrochronological relations. [Reinhold & Hekker \(2020\)](#) updated this value to ~ 750 Myr with a larger set of *K2* data. Contrary to the hypothesis that the gap aligns itself with a certain isochrone, [Curtis et al. \(2020\)](#) identified that the open cluster Ruprecht 147 contains stars above and below the gap, as well as one star that appeared to be within the gap. This suggests that the gap does not align itself with a particular age. Instead, they argued that the gap aligns itself with a line of constant Rossby number of 0.5. The Rossby Number is defined as the ratio of the rotation period to the convective turnover timescale ($R_o = P_{rot} / \tau_{conv}$), which itself is

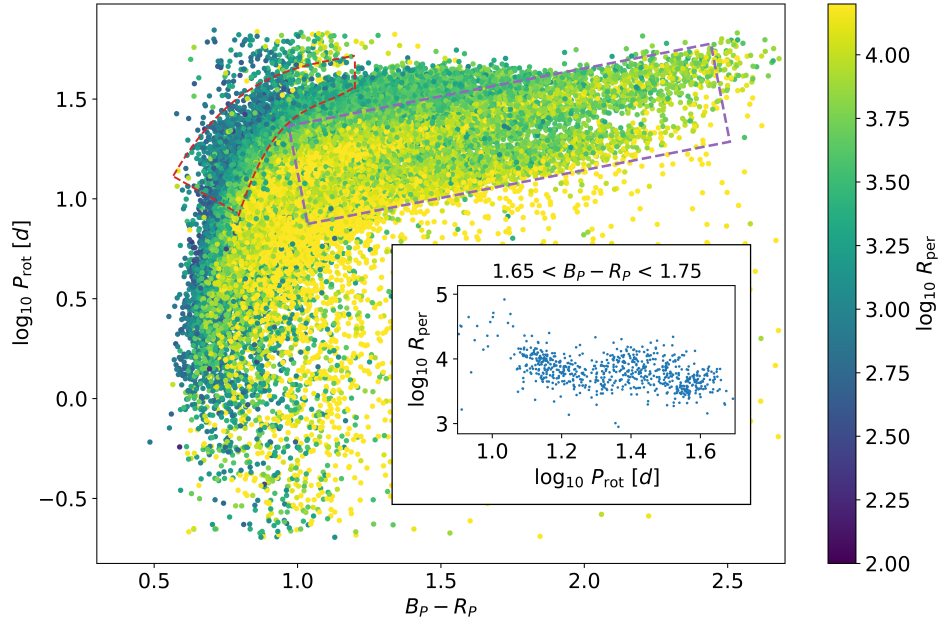


FIGURE 1.4: A scatter plot showing *Gaia DR3* $B_P - R_P$ colour against logarithm of the *Kepler* [McQuillan et al. \(2014\)](#) rotation period sample, coloured by the logarithm of the photometric variability (R_{per}). Highlighted in this Figure is the intermediate period gap (region surrounded by a purple dashed line) and the long-period pile-up (region surrounded by a red dashed line). **Inset:** Logarithm of R_{per} against logarithm of rotation period for stars $1.65 < B_P - R_P < 1.75$. The dip in R_{per} at $\log_{10} P_{\text{rot}} \sim 1.25$ aligns itself with the intermediate period gap. R_{per} decreases towards the gap from above and below, suggesting the gap is representative of a minimum of observability of rotation period.

dependent on mass and approximately constant for a star’s main-sequence lifetime. The Rossby number is associated with the magnetic dynamo, (see, e.g., [Noyes et al., 1984](#); [Montesinos et al., 2001](#); [Augustson et al., 2019](#)). To simplify, a star can be thought of as a volume of charged particles. As a star rotates, so do the charged particles within it. Moving charged particles induce a magnetic field, creating a magnetic dynamo. As the star rotationally evolves, so does the magnetic dynamo.

The gap appears to align with a line of constant Rossby number, this may suggest that the gap is instead caused by an event in the evolution of the magnetic dynamo rather than an event in time. This is a notable result as the magnetic dynamo is associated with a number of stellar phenomena, such as magnetorotational instabilities (angular momentum transport processes associated with the magnetic field) and stellar activity. Prospective hypotheses for the intermediate period gap can be broken down into three categories: bursty star formation, modified angular momentum transport, and decreased observability of rotation periods.

While the bursty star formation hypothesis is not a currently favoured, it led early studies into the intermediate period gap. [McQuillan et al. \(2014\)](#) first proposed that the gap is the artifact

of a recent period of bursty star formation in the *Kepler* field, resulting in a young (< 50 Myr), fast rotating, population and an older, background slowly rotating, population. [Davenport \(2017\)](#) suggest that the fast and slow rotators in this sample also exhibit a different distribution in proper motion. Two kinematically separate groups would favour the explanation of two epochs of star formation in the *Kepler* field. This explanation is further supported by the work of [Davenport & Covey \(2018\)](#), who argued that the observation of the gap correlates with Galactic height, which is assumed to be related to stellar age.

The bursty star formation hypothesis would account for the overpopulation of observations below the gap. The dearth of observations would then represent the background observation rate of rotation periods within this period range. [Gordon et al. \(2021\)](#) provided evidence against this hypothesis through analysis of *K2* data. They found that the intermediate period gap is present in the multiple pointings of the *K2* mission, suggesting that recent bursty star formation is isotropic, and that clusters with different ages contain stars that have crossed the gap.

The bursty star formation hypothesis suggests that all clusters universally went through a period of bursty star formation ~ 50 Myr ago. The two populations, above and below the gap, however, do not substantially universally differ in other spectroscopic and photometric observations. Furthermore, comparing Figures 1.3 and of 1.4, the gap has a sharper slope than the sequences associated with constant age populations from Praesepe ([Douglas et al., 2017, 2019](#)), NGC 6811 ([Curtis et al., 2019](#)) and Ruprecht 147 ([Curtis et al., 2020](#)). If the bimodal star formation scenario explained the gap, the gap should have the same shape and position for each cluster and the entire *K2/Kepler* sample. This suggests that a universal two-population bursty star formation mechanism is not favoured.

Let us now consider that the gap results from modifications to angular momentum transport. [McQuillan et al. \(2014\)](#) first proposed that the gap is the result of two variations to Skumanich rotational evolution: first stars below the gap undergo a period of stalled spin-down, resulting in the observed over-density of stars along the lower branch, followed by a period of accelerated spin-down, resulting in the dearth of stars in the gap. For some time there was very little evidence nor a proposed mechanism for the period of accelerated spin-down. Recent works by [Lu et al. \(2022\)](#) have shown that the gap is most apparent for stars less massive than $1.3 M_{\odot}$ and more massive than $0.4 M_{\odot}$. If we look closely at Figure 1.5 we can see that for the *ZTF* sample (black dots), the intermediate period gap is most apparent for stars $1.5 < B_P - R_P < 2.5$ and closes for low-mass ($B_P - R_P > 2.5$) stars. Stars redder than $B_P - R_P > 2.5$ are fully convective ([Amard et al., 2019](#)), suggesting that the gap may be another phenomenon related to the interplay between angular momentum transport between the radiative core and convective surface, and surface rotational braking along the main-sequence.

The proposed mechanism underlying this scenario is the mass-dependent decoupling and re-coupling of the core and the envelope proposed in [Lanzafame & Spada \(2015\)](#) and [Spada &](#)

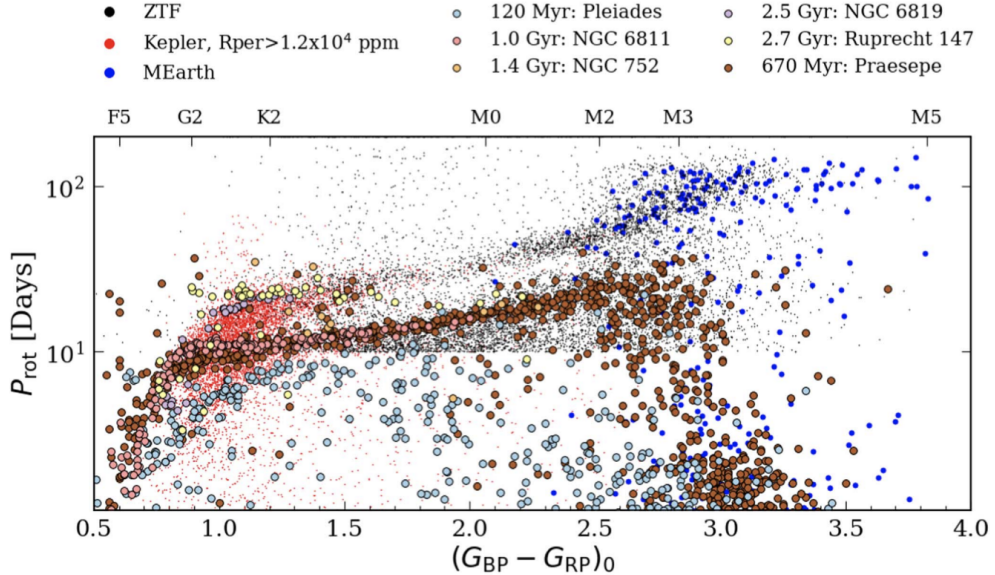


FIGURE 1.5: Rotation period against $Gaia B_P - R_P$ from *Kepler* *ZTF*, and *MEarth* (Irwin et al., 2011; Berta et al., 2012; Newton et al., 2018), overlayed with various open cluster measurements. Highlighted by this figure is the disappearance of the intermediate period gap above $B_P - R_P > 2.5$, the boundary where stars are fully convective. This suggests that the rotation period gap is related to the coupling of the core and surface of low-mass stars ($0.4 < M < 1.3 M_{\odot}$). Sourced from the top panel of Figure 8 in Lu et al. (2022).

Lanza (2020), discussed earlier in this work. Angus et al. (2020) suggest that the core envelope decoupling and recoupling may explain the period gap as a break between a “younger” pile-up regime ($R_o < 0.6$) in which surface rotation periods are relatively constant with time from core-surface angular momentum transport, and increase with decreasing mass from an “older” ($R_o > 0.6$) regime. The gap then represents a period of relatively fast spin evolution during the transition between the two. Proponents of this hypothesis suggest that the gap results from a period of enhanced spin-down following core and surface recoupling where stars “jump” the gap before resuming Skumanich spin-down, as is observed for older clusters. Models of rotational evolution (and, therefore, the mechanism underlying the gap) that reflect the proposed rapid spin-down are yet to be identified. Under this model, the gap reflects an under-density of stars but would not be empty. Curtis et al. (2020) observed five Ruprecht 147 stars in or just beneath the gap that may express evidence of enhanced magnetic spin-down, though these stars are yet to be thoroughly investigated.

The final current explanation is that the gap results from a lack of observations of rotation periods. Observing the rotation period of *Kepler* stars requires that stars express photometric oscillations from stellar spots. However, stellar spots can both increase or decrease stars’ bolometric luminosity. Reinhold & Reiners (2013) and Reinhold et al. (2019) propose stars transition in stellar spot structure from spot to faculae dominance in the photosphere: resulting in a decrease in photometric variability of stars and thus decreased observation of stars within the gap. In the McQuillan et al. (2014) sample, stellar rotation periods are measured from photometric

variability due to stellar spots. Suppose the bolometric flux does not vary due to stellar spots in the gap region. In that case, the amplitude of periodic variability would decrease within this region. [Reinhold et al. \(2019\)](#) suggests that the gap is full of stars and represents a minimum in the detectability of rotation periods.

Supporting this hypothesis, in both the *Kepler* and *K2* fields, the variability amplitude (R_{per}) decreases towards the gap from both lower and higher rotation periods. This can be seen in the [McQuillan et al. \(2014\)](#) rotation period distribution shown in Figure 1.4, which is coloured by the logarithm of R_{per} , and is highlighted in the inset plot of the logarithm of R_{per} against the logarithm of the rotation period. While there is evidence that stars undergo spot-to-faculae dominance, e.g. the Vaughan-Preston gap ([Vaughan & Preston, 1980](#)), this occurs much later in a star's lifetime ($R_o \sim 1$). Further, there is evidence that stars above and below the gap are both spot-dominated ([Lockwood et al., 2007](#); [Reinhold et al., 2019](#)). [Reinhold et al. \(2019\)](#) speculate that activity cycles that vary the spot-to-faculae brightness contributions on rotational timescales could be the process underlying the rotation period gap.

Observations of open cluster rotational distributions beyond the gap suggest that low-mass stars ($< 1 M_\odot$) that have crossed the gap ($R_o > 0.6$) continue to spin-down and follow the Skumanich-like rotational evolution until they leave the main-sequence. On the other hand, there is an apparent overabundance of stars at large ($P_{\text{rot}} \sim 30$ d) rotation periods (dependent on their mass). Above this rotation period is a lack of observations for stars hotter than 5500 K. Stars with higher masses also appear to have lower rotation periods on the pile-up than their less massive counterparts. This results in what is known as the long-period pile-up, as noted in Figure 1.4. The long-period pile-up aligns itself in the [McQuillan et al. \(2014\)](#) period distribution with Rossby number ($R_o = 2.08$) ([van Saders et al., 2019](#)).

[van Saders et al. \(2019\)](#) suggest that the long-period pile-up could result from decreased magnetic braking precisely at this Rossby number, resulting in an over-density of stars and a lack of observations of larger rotation periods, or that we simply do not observe stars with larger rotation periods. They propose variations to the stellar spot activity to explain the decrease in observed periods¹². They argue that the error in observed periods can smooth out the over-density in stars, suggesting that the long-period pile-up is an observational artifact. Further supporting this explanation [David et al. \(2022\)](#) found that photometric variability significantly decreases above the long-period pile-up. This suggests that there is unobserved population of stars with longer rotation periods.

Under the weakened magnetic braking model, [David et al. \(2022\)](#) suggest that stars $1 M_\odot < M < 1.3 M_\odot$ in this temperature regime may spend half of their main-sequence lifetimes at the long-period pile-up, with only modest variances to their rotation period. Below this mass regime, stars

¹²These explanations are similar to those that have been invoked to explain the intermediate period gap and for the sake of brevity we will not repeat them.

appear to continue to lose angular momentum through wind braking following the Skumanich relation. This results in stars with large rotation periods when they enter the post-main-sequence. While the evolution of surface rotation period of main-sequence stars was initially thought to be quite simple, indeed it is becoming apparent just how complex that evolution is.

1.2.2 Post-main-sequence

Rapid changes to the internal structure in the post-main-sequence result in variations to their rotation profile. While qualitatively, the rotation follows basic theoretical relations (e.g., compression of the core and expansion of the surface resulting in faster and slower rotation respectively, through conservation of angular momentum) there are discrepancies between what we observe and what models predict.

For low-mass ($1.1 - 1.5 M_{\odot}$) stars during the post-main-sequence, angular momentum transport between the core and the surface can be probed. While surface rotation periods can be measured for post-main-sequence stars through photometric variations due to stellar spots (McQuillan et al., 2014; Ceillier et al., 2017) and spectroscopic line broadenings, asteroseismic inference of both core and surface rates through asteroseismic rotational splittings is the standard for probing rotation evolution in this regime (Deheuvels et al., 2014; Gehan et al., 2018; Deheuvels et al., 2020; Fellay et al., 2021). This results from a combination of the expression of mixed modes, shorter mode lifetimes, and increased core rotation rates.

Following the main-sequence, low-mass stellar rotation varies with the evolutionary phase. Models of rotating stellar evolution (see, e.g., Maeder & Meynet, 2000; Heger et al., 2000) predict the following qualitative evolutionary pathway. Towards the end of the main-sequence the rotation profile is largely flat. Assuming conservation of angular momentum as hydrogen core burning stops, pressure in the core drops, resulting in core contraction while the convective surface region expands. Resultingly, the core is spun-up while the surface is spun-down. The core should continue to spin-up as the core contracts along the RGB until entering the red clump (low-mass core-He burning). The core burning re-introduces core pressure, and the resulting expansion of the core decreases the core rotation rate. When core-He burning ceases, the core pressure drops again, resulting in a spun-up white dwarf (relative to the core rotation rate of red clump stars). We highlight the qualitative rotation evolution of post-main-sequence stars in Figure 1.6. Observations suggest that low-mass stars follow this pathway (Mosser et al., 2012; Deheuvels et al., 2014, 2015; Hermes et al., 2017a; Gehan et al., 2018; Deheuvels et al., 2020).

Observations of young subgiants suggest that terminal age main-sequence stars' rotation profiles are relatively flat (Deheuvels et al., 2020), while older subgiants have differentially rotating cores and surfaces (Deheuvels et al., 2014). The measured core and surface rotation rates of older subgiants suggest core-to-surface rotation rate ratio of subgiants (Ω_c/Ω_s) are one to two

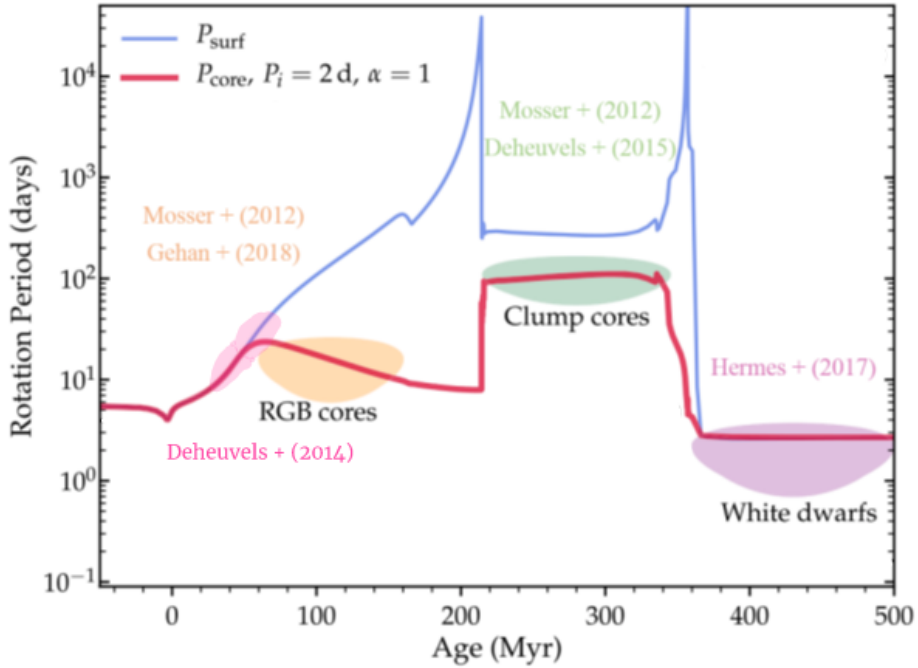


FIGURE 1.6: Core (red) and surface (blue) rotation rates with additional angular momentum transport following the prescription of Spada et al. (2016). Coloured sections denote evolutionary milestones and the works that have provided constraints to these milestones: subgiant core and surface rotation rates (pink), RGB cores (orange), clump core (green), and white dwarf surface (purple) rotation rates. Adapted from Figure 3 in Fuller et al. (2019)

orders of magnitude smaller than models predict (Deheuvels et al., 2014; Spada et al., 2016; Moyano et al., 2022), suggesting the need for additional angular momentum transport in rotating post-main-sequence models (Fuller et al., 2015; Spada et al., 2016; Ouazzani et al., 2019; Eggenberger et al., 2019). While core rotation rates were first believed to decrease along the RGB¹³ (Mosser et al., 2012), revised measurements, and larger sample size, revealed that the core rotation rates of RGB stars appear constant during a period when the contraction of the core should spin them up (Mosser et al., 2012; Gehan et al., 2018; Moyano et al., 2022). The core rotation rates of early RGB and red clump stars suggest a continued excess angular momentum transport during this phase of evolution (Cantiello et al., 2014; Moyano et al., 2022). On the other hand, the angular momentum of white dwarfs agree with the core angular momentum of clump stars, assuming conservation of angular momentum (Cantiello et al., 2014; den Hartogh et al., 2019). Cantiello et al. (2014) suggests that this feature may be owing to the short evolutionary timescale between the red clump and white dwarf phases, rather than indicative of a decrease in the excess angular momentum transport.

¹³Indeed when core rotation rates of red giants are plotted against $\log g$, a proxy for evolution, they do appear to decrease with evolution. When plotted against the more appropriate scale of mixed mode coupling (see Equation 10 in Gehan et al. (2018) and compare Figures 12 and 13 in this work), they are constant with evolution.

The physical mechanism underlying the excess angular momentum transport is currently unidentified. However, several notable relations with mass and evolutionary state have been determined by calculating the excess angular momentum transport required to match observations. [Spada et al. \(2016\)](#) quantified the increased angular momentum transport required to match the observed subgiant core and surface rotation rates measured in [Deheuvels et al. \(2014\)](#). They introduced an additive angular momentum diffusion coefficient to the transport of angular momentum equation in the radiative zone, which obeys an advection-diffusion equation ([Zahn, 1992](#); [Maeder & Zahn, 1998](#); [Eggenberger et al., 2008](#))

$$\rho \frac{d}{dt} (r^2 \Omega(r)) = \frac{1}{5r^2} \frac{\partial}{\partial r} (\rho r^4 \Omega(r) U(r)) + \frac{1}{r^2} \frac{\partial}{\partial r} \left(\rho (D_{\text{shear}} + v_{\text{add}}) r^4 \frac{\partial \Omega(r)}{\partial r} \right), \quad (1.2)$$

where r and ρ are the characteristic radius and density on an isobar. $\Omega(r)$ is the mean rotational rate, and $U(r)$ is the velocity of meridional currents in the radial direction. D_{shear} is the diffusion coefficient for the angular momentum shear instability (see Equation 10 in [Eggenberger et al. \(2010\)](#)) and v_{add} is the additional viscosity corresponding to the excess angular momentum transport. Their results suggest that the additional angular momentum transport decreases as stars ascend the subgiant branch and increases with mass. The suggested scale of excess angular momentum transport they propose is on the order of $10^3 - 10^4 \text{ cm}^2 \text{s}^{-1}$. Which is similar to D_{shear} close to the convective envelope, but rapidly decreases to the order of $10^1 \text{ cm}^2 \text{s}^{-1}$ in the stellar core. Comparing Figures 1.7 and 1.8 we see that the introduction of additional viscosity to the model term results in agreement with the core to surface rotation fraction in the [Deheuvels et al. \(2014\)](#) sample.

[Moyano et al. \(2022\)](#) performed a similar analysis but with the core rotation rates of RGB and red clump stars measured in [Mosser et al. \(2012\)](#) and [Gehan et al. \(2018\)](#). They found that the same order of magnitude additional viscosity term was required to explain the approximately constant core rotation rates of red giant and red clump stars. Qualitatively, they found that the additional angular momentum transport becomes stronger when the star evolves up the RGB through shell hydrogen burning. Angular momentum must be redistributed between two to three orders of magnitude more efficiently for red clump stars than for red giants closer to the main-sequence turn-off, consistent with [den Hartogh et al. \(2019\)](#). Figures 1.8 and 1.9 highlight that models of red-giant evolution, with the additional viscosity introduced in this work, now agree with the observed core rotation rates observed in [Gehan et al. \(2018\)](#).

Mechanisms underlying the excess angular momentum transport have also been proposed. [Barker et al. \(2019, 2020\)](#) studied the role of the Goldreich-Schuber-Fricke (GSF) instability ([Goldreich & Schubert, 1967](#); [Fricke, 1967](#)) in angular momentum transport for post-main-sequence stars. They suggest that the GSF instability can introduce additional viscosity up to $10^4 \text{ cm}^2 \text{s}^{-1}$ for low-mass stars but is two orders of magnitude too small to reflect the rotation of higher mass stars.

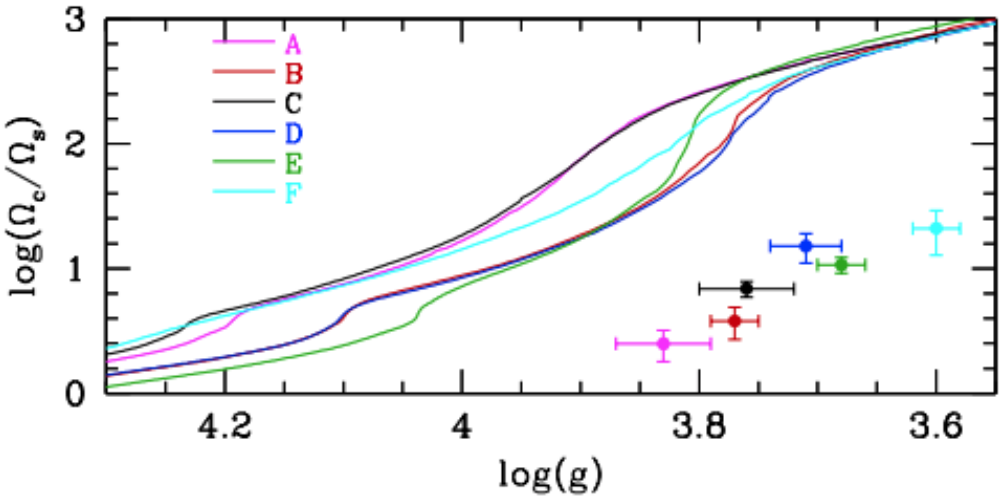


FIGURE 1.7: Logarithm of core to surface rotation rate against stellar surface gravity. Observed core-to-surface rotation rate ratio of the six subgiants measured in the [Deheuvels et al. \(2014\)](#) sample (A, B, C, D, E, and F) are shown with scatter points with error bars. Core-to-surface rotation rate ratios of rotating models of the stars in that sample without additional angular momentum transport ([Eggenberger et al., 2019](#)) are shown with lines. The observed core-to-surface rotation rates are much smaller than models predict. This implies additional angular momentum transport than is currently accounted for models. Sourced from Figure 2 in [Eggenberger et al. \(2019\)](#).

Magnetorotational instabilities constitute another candidate to explain the internal rotation of evolved stars. Two potential candidates are azimuthal magnetic rotational instabilities (AMRI; see [Ruediger et al., 2014; Rüdiger et al., 2015](#)) and the Tayler-Spruit instability (see [Spruit, 2002](#)). [Rüdiger et al. \(2015\)](#) suggest AMRIs can increase molecular viscosity to the magnitude required to explain observations. On the other hand, there is no evidence to suggest that this instability reflects the trends with mass and evolution. The Tayler-Spruit instability does introduce excess angular momentum transport in the post-main-sequence ([Fuller et al., 2019](#)), however, it cannot simultaneously reflect the observations of both subgiants and red giants ([Eggenberger et al., 2019; den Hartogh et al., 2019](#)).

[Spada et al. \(2016\)](#) propose the efficiency of angular momentum transport may be related to the core to surface rotation rate to some power $(\Omega_c/\Omega_s)^\alpha$, which can be related to magnetorotational instabilities. This work suggests that an α of reflects the core rotation rates of red giants claimed in [Mosser et al. \(2012\)](#). [Moyano et al. \(2022\)](#) revisited this prescription and found that $\alpha = 3$ more accurately reflects the approximately constant rotation core rotation rates of red giants observed by [Gehan et al. \(2018\)](#). [Spada et al. \(2016\)](#) was limited to a single model with a mass of $1.25 M_\odot$. No investigation into the parameterisation with mass could therefore be performed.

Other physical mechanisms have been suggested to have a role in excess angular momentum transport, such as angular momentum transport by internal gravity waves ([Pinçon et al., 2017](#)) or mixed-modes ([Belkacem et al., 2015](#)). However, the scale of their introduced additional

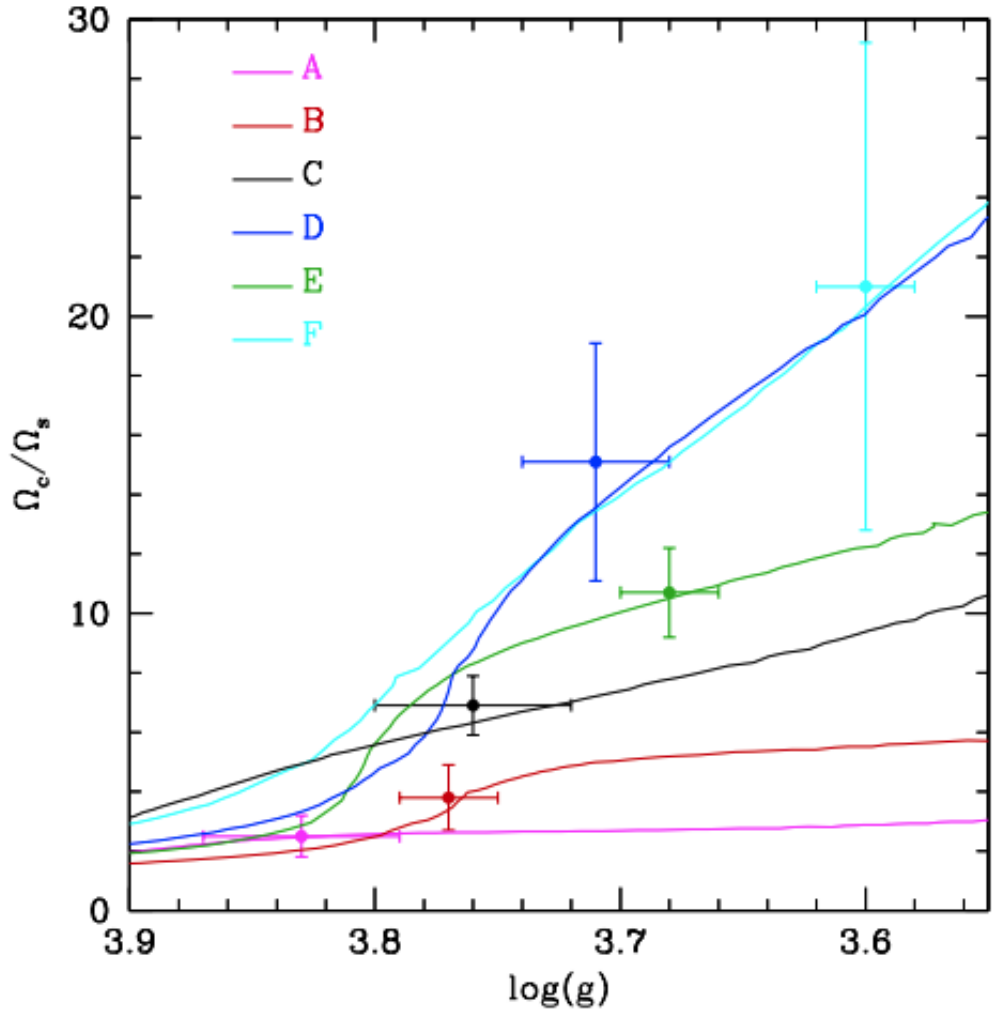


FIGURE 1.8: Same as Figure 1.7 but with additional angular momentum transport introduced for the models to reflect the observations. Sourced from Figure 3 in [Eggenberger et al. \(2019\)](#).

viscosity is yet to be investigated. Disentangling each of these proposed mechanisms' relative importance to the additional angular momentum transport required to explain the observations requires much more data.

We speculate that the simultaneous measurement of subgiants' core and surface rotation rates may be the best probes for constraining the excess angular momentum transport. A few pathways exist to further probe the mechanism underlying excess angular momentum transport through asteroseismology alone. Either more stars need to have their core and surface rotation rates measured through asteroseismology (ensemble fitting), or stronger constraints must be placed on the rotation profile between the core and the surface (single star constraints).

If more stars have their core and surface rotation rates observed, then more measurements of the excess angular momentum are required for state-of-the-art models to match. The excess angular momentum transport required to match observations appears to depend on mass and

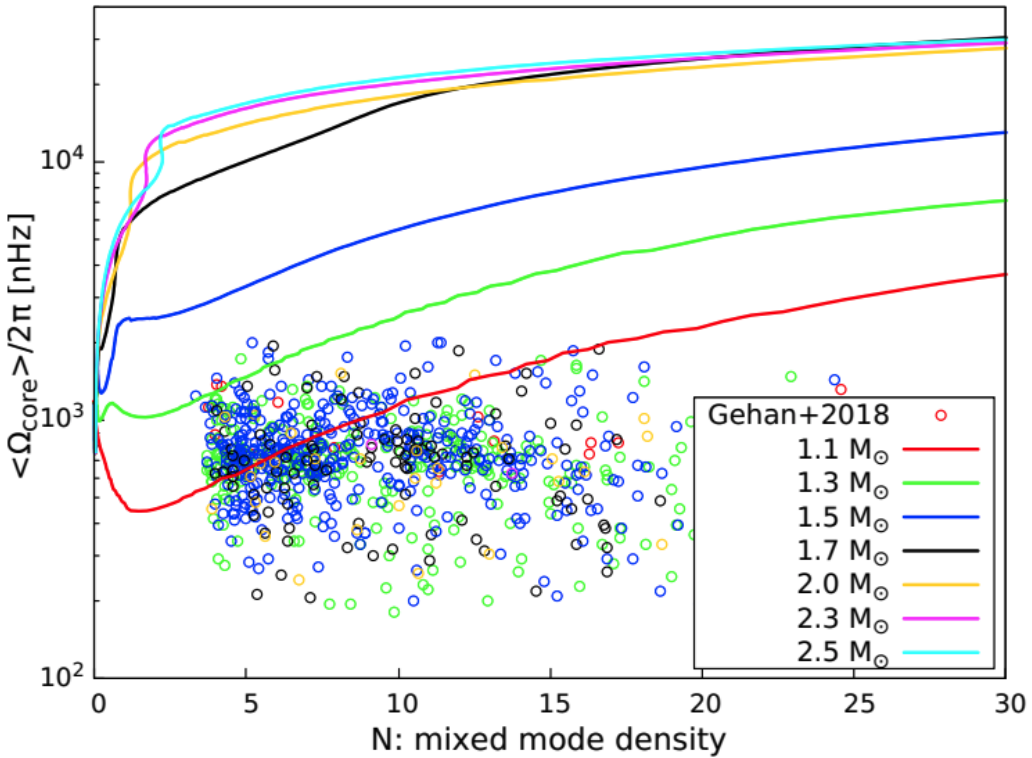


FIGURE 1.9: Average core rotation rates of red giants against mixed mode density (a proxy for evolution). **Dots:** Observed core rotation rates from Gehan et al. (2018) **Lines:** rotating models of the stars in that sample without additional angular momentum transport (Moyano et al., 2022). The observed core rates are much smaller than models predict, implying excess angular momentum transport is required for the models to reflect the observations. Sourced from Figure 6 in Moyano et al. (2022).

evolution. Stronger constraints on the dependency of the excess angular momentum transport on these quantities provide information about the underlying mechanism. The Kepler asteroseismic data currently available suggests that the efficiency of the excess angular momentum transport increases with the star’s mass (Eggenberger et al., 2019). However, the efficiency of angular momentum transport decreases with evolution during the subgiant phase. Consequently, a transport process with an efficiency that depends on the angular momentum gradient between the core and the surface cannot be at play in subgiants. Identifying, with more precision, the dependency of excess angular momentum transport on stellar quantities would provide evidence for or discredit proposed mechanisms.

The internal shape of the rotation profile of subgiants reflects the underlying mechanism that created it. Therefore, evidence for or against particular shapes of rotation profiles constrains possible mechanisms. A strong gradient in the rotation profile in the core of a subgiant, for example, is incompatible with angular momentum transport through deep fossil magnetic fields (Gough & Thompson, 1990), as they would likely smooth out sharp features. This is because differential rotation is expected to be damped along poloidal field lines (Garaud, 2002; Strugarek

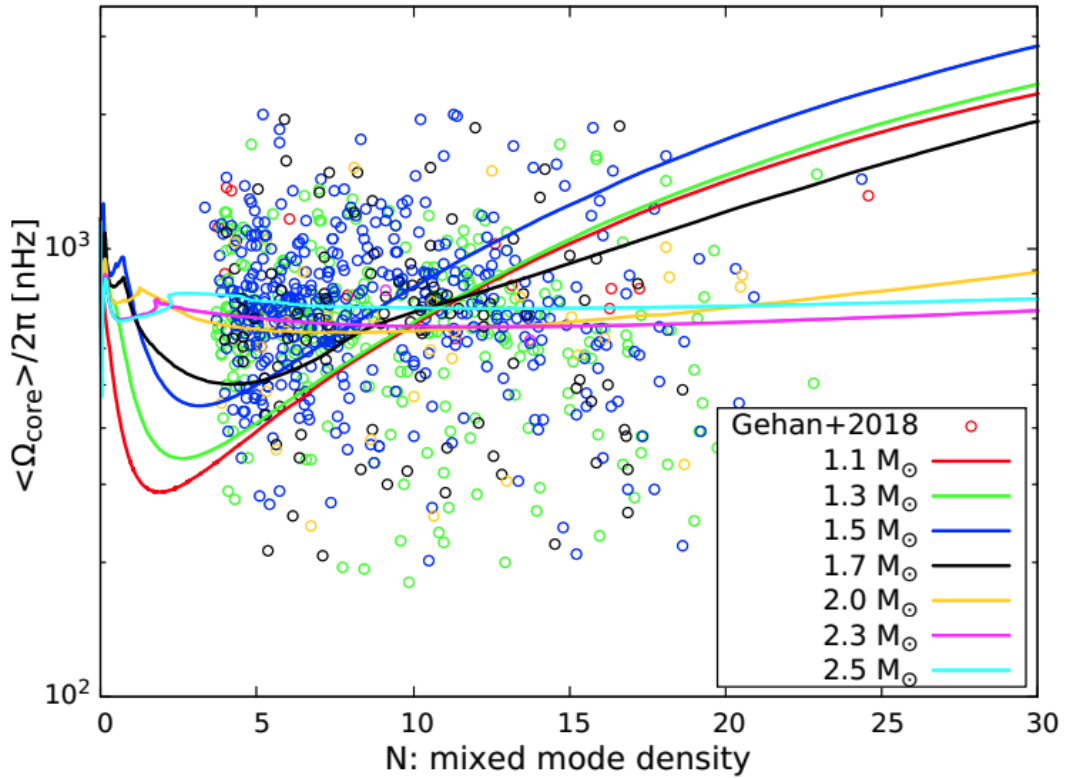


FIGURE 1.10: Same as Figure 1.9 but with additional angular momentum transport introduced for the models to reflect the observations. Sourced from Figure 7 in Moyano et al. (2022).

et al., 2011). Internal gravity waves, on the other hand, are expected to be efficient during the advanced phases of stellar evolution (Charbonnel & Talon, 2008). Internal gravity waves can give birth to localised weak gradients in the rotation profile, as a result of extraction and deposit of angular momentum (Charbonnel & Talon, 2005). A sharp rotational gradient could also potentially trigger magneto-rotational instabilities that would transport angular momentum (Balbus & Hawley, 1994; Arlt et al., 2003; Menou & Mer, 2006; Fuller et al., 2015, 2019; Moyano et al., 2022). Evidence of a strong angular momentum gradient towards the core of a subgiant quickly constrains the number of possible angular momentum transport mechanisms that could solve the angular momentum transport problem.

Two obvious problems impede the single-star pathway: the need for observations of high signal-to-noise higher degree modes, and the results of methods used to measure rotation profiles being unstable to high-resolution inversions. Constraints on the rotation profile in intermediate points between the core and surface require the observations of oscillation modes of $l \approx 10$ (Ahlborn et al., 2020). For reliable measurements of such oscillations, much longer observation periods, longer than *CoRoT* and *Kepler*, of subgiants are required.

Both of these pathways require much more asteroseismic data than is currently available. For ensemble fitting to be viable, many subgiants would need to be observed over long baselines

with short-cadence observations. If the *Kepler* mission is exemplary, then the baseline required for high-signal-to-noise asteroseismic observations is on the order of ~ 4 years per star.

Of order thirty subgiant lightcurves have measurable rotational splittings (Li et al., 2020a,b), though the rotational splitting data is yet to be released and analysed. The results will be undoubtedly informative, though we will not speculate on the extent to which they will solve the subgiant excess angular momentum transport problem. Hatt et al. (2023) suggests that there are of order four thousand stars in the *TESS* short-cadence catalogue with observable solar-like oscillation features. The measured frequency of peak oscillation power (v_{\max}) of stars in this sample suggests that some of these stars are subgiants. While no rotational splittings of these stars have been reported, some of these stars may lay in the continuous viewing zone. This means their baselines are approaching 4 years and may soon offer a separate sample of subgiants with observations of asteroseismic rotational splittings. While we could speculate about future asteroseismic-focused missions, it will be some time before any new asteroseismic rotation signals in subgiants are made.

Independent constraints can also be placed on the evolution of the surface rotation of subgiants. Santos et al. (2021) measured the surface rotation of 4,500 subgiants using photometric oscillations from stellar spots. The measured rotation periods against their effective temperature are shown in Figure 1.11. Within this figure, there are a few notable features. While subgiants are definitionally older than their main-sequence counterparts, there is a sample of fast-rotating stars coincident with the fast rotators on the main-sequence. This could be explained by most of the stars in this sample having a higher mass than the Kraft break. They have passed through the main-sequence with fast rotating surfaces, entering the subgiant phase; their effective temperatures decrease and are shifted to the right in this diagram relative to their main-sequence counterparts. The high density of fast-rotating stars could also result from an observational bias. Long rotation periods require longer baselines to recover and thus have a decreased observed fraction. Among the sample is a group of slow-rotating ($P > 60$ days) targets with T_{eff} between 5000 and 6000 K. These are consistent with more evolved subgiants, as the slowest of these targets are located close to the RGB. This work also suggests that the decreased observation of rotation periods >60 days, a feature of the long-period pile-up, is the result of a lack of observations of main-sequence stars rather than an inherent lack of long-period probing power by *Kepler*.

Ceillier et al. (2017) measured the surface rotation periods of 361 red giants from stellar spot photometric variability. The measured rotation periods against their mass are shown in Figure 1.12. Compared to the subgiant analysis of Santos et al. (2021), the surface rotation period of red giant stars is greater than their subgiant counterparts. They suggest that the surfaces of these stars rotate faster than models predict (Tayar et al., 2015). They conclude that the large percentage of rapid rotators must result from interactions of red giants with other bodies. This

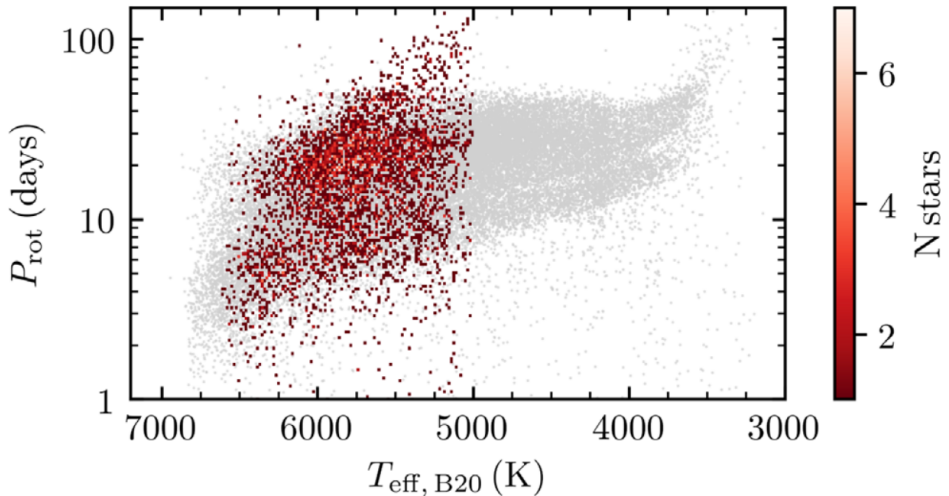


FIGURE 1.11: Surface rotation period against effective temperature of subgiants in the [Santos et al. \(2021\)](#) sample overlayed over the [Kepler McQuillan et al. \(2014\)](#) sample. Sourced from the bottom panel of Figure 5 in [Santos et al. \(2021\)](#).

work, however, is older than the revised excess angular momentum transport research discussed earlier. Their results need to be reexamined within the context of excess angular momentum transport.

Finally, we discuss the rotating remnants of low-mass post-main-sequence evolution: white dwarfs. White dwarfs do not evolve rotationally, though their observed rotation rates constrain angular momentum during the red clump phase. [Hermes et al. \(2017a\)](#) suggest that the rotation periods of white dwarfs decrease with the progenitor's mass. As previously discussed, the surface rotation rates of white dwarfs are consistent with angular momentum conservation following the red clump ([den Hartogh et al., 2019; Cantiello et al., 2014](#)). This is because the time scale of angular momentum transport is longer than the timescale of evolution from red clump star to a white dwarf. [den Hartogh et al. \(2019\)](#) suggest that mass-dependent angular momentum transport must decrease with evolution along the red clump such that the angular momentum of terminal red clump rotation cores agree with the angular momentum of white dwarf stars.

Latitudinal differential rotation

Another facet of rotation is latitudinal rotation. This phenomenon refers to the observation that the rotation profiles of stars vary depending on their latitudes. This phenomenon was initially discovered in the Sun, where the equator completes a rotation in 25 days, while the poles take 38 days for a full rotation. The Sun is therefore expressing equator-fast (relative to the rotation rate at the poles) differential rotation. Helioseismic measurements indicate that this surface latitude dependence of rotation diminishes near the base of the convective zone, but measurements beyond this point become less reliable due to decreased sensitivity in seismology ([Howe, 2009](#)).

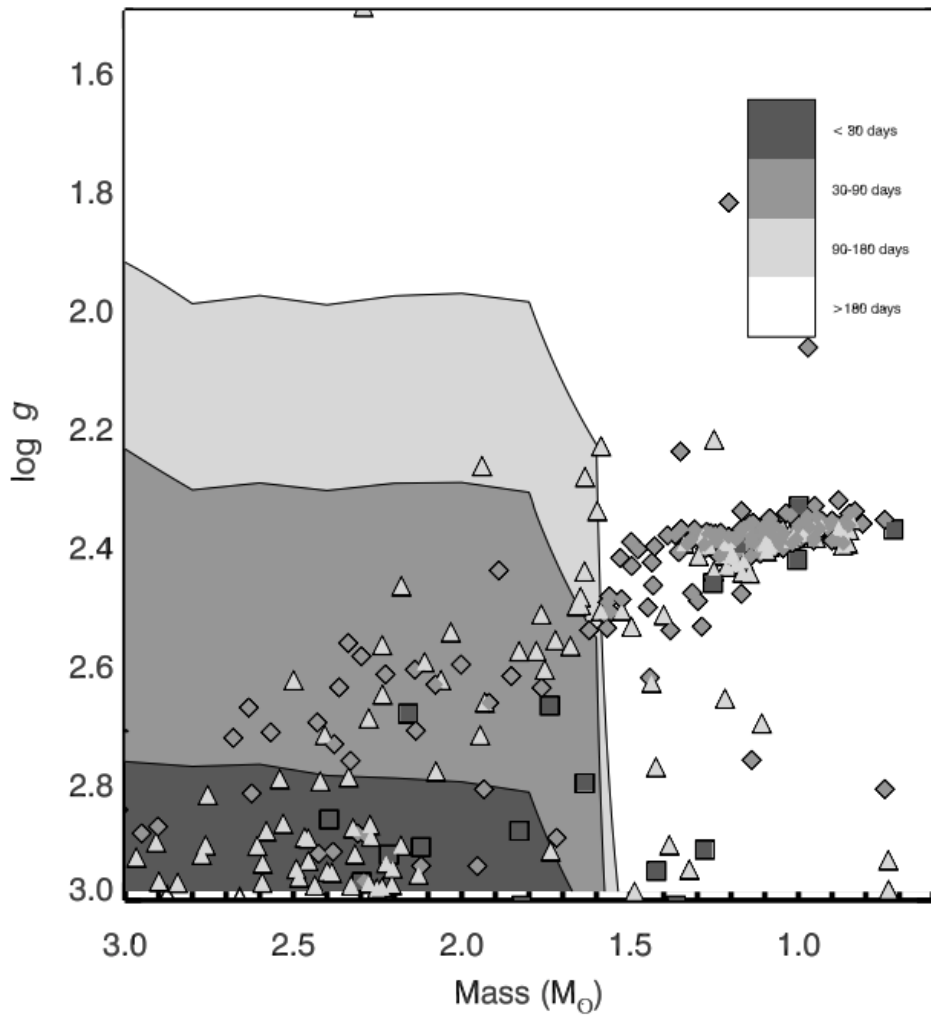


FIGURE 1.12: Surface rotation period against mass of red giant stars from [Ceillier et al. \(2017\)](#). Sourced from the top panel of Figure 7 in [Ceillier et al. \(2017\)](#).

While the internal latitudinal differential rotation of stars, other than the Sun, remains unknown it is believed that they also undergo solid-body rotation within the base of the convective zone. Hence, in this thesis, the term ‘latitudinal differential rotation’ specifically pertains to surface latitudinal differential rotation.

Studies based on rotating-magnetohydrodynamic models of stars ([Brun et al., 2022](#)) suggest that stars with $R_o < 0.5$ tend to exhibit latitudinally-flat, or perhaps cylindrical, rotation profiles. However, it’s worth noting that the term ‘latitudinally-flat’ is somewhat misleading: observations indicate that very rapidly rotating stars ($R_o < 0.5$) in fact, express equator-fast latitudinal dependence on rotation rate, with the scale of the shear being just smaller than the arbitrary limit set for considering it as ‘significant’ latitudinal differential rotation. Intermediate rotators ($0.5 < R_o < 2$) are predicted to express equator-fast (relative to the poles) differential rotation profiles, while stars where $R_o > 2$ are predicted to exhibit equator-slow (again, relative

to the poles) rotation profiles. Recent work ([Benomar et al., 2018](#)) suggest that observations of the latitudinal differential rotation of solar analogues increase with R_o , while observations of young, fast-rotating stars using time-series Doppler imaging are consistent with latitudinally-flat differential rotation (see, e.g., [Lanza & Rodono, 1996](#)). Definitive observational evidence confirming latitudinally-flat or anti-solar-like differential rotation is yet to be established. The post-main-sequence evolution of latitudinal differential rotation is also a currently unexplored field of study. We do not know if post-main-sequence stars do express latitudinal differential rotation or if they are expected to theoretically.

The study of the mechanisms behind differential rotation remains an active and ongoing field of research. In the surface convective region of low-mass stars, there are four believed mechanisms responsible for redistributing angular momentum: latitudinal and radial flows from meridional circulation, convective flow in the radial direction, magnetic forces, and viscous diffusion. The exact positions in the convective region and relative strengths of these mechanisms are currently uncertain and require further investigation to understand their impact on the evolution of latitudinal differential rotation.

Unfortunately, our understanding of the evolution of latitudinal differential rotation in low-mass stars is still limited, primarily due to the shortcomings of the current techniques used for analysis. These methods often suffer from inaccuracies, lack precision, or are applicable only to specific stars, making it challenging to infer the evolution of differential rotation accurately.

One of the early techniques used in this research involved studying the effect of stellar spots on spectral line features, known as Doppler imaging. By observing the perturbations caused by spots on the spectroscopic line profile and analysing the position of these spots, researchers could estimate the rotation rate at different latitudes and thereby measure the surface differential rotation. However, this method has its limitations. It requires high-cadence long baseline time-series spectroscopy, which may not always be readily available. Additionally, the interpretation of surface features and their positions on stars can be ambiguous, leading to potential degeneracy in the results. [Collier Cameron \(2007\)](#) has raised concerns about underestimated errors associated with this method.

[Reiners & Schmitt \(2002\)](#), on the other hand, developed a Fourier-transform-based method to determine latitudinal differential rotation from a single observation of the spectroscopic line shape. The method uses the deviation of line profiles from a rigidly rotating surface to estimate the latitudinal differential rotation. While the benefit of requiring a single spectroscopic observation of a star is obvious, the applicability is limited. The method is limited to magnetically active fast rotators ($v \sin i > 10 \text{ km s}^{-1}$), where line-broadenings are large enough to be well resolved. [Barnes et al. \(2005\); Reiners & Schmitt \(2002\)](#) adopt this method and confirm that latitudinal differential rotation increases with increasing temperature for young, rapidly rotating, magnetically active stars. The observation of differential rotation using this method is limited

to young stars, hence the evolution of differential rotation with age cannot be probed using this method.

Another prospect for measuring differential rotation arises through the latitudinal variation in the position of stellar spots and thus the measurement of multiple periods in a light curve (see, e.g., [Walkowicz & Basri, 2013](#); [Reinhold et al., 2013](#)). Measuring latitudinal differential rotation in this way is straightforward in theory: if multiple surface features appear at different latitudes then multiple peaks in the power spectrum arise from which the different rotation periods can be measured. The difference between the two periods provides a measure of the surface rotational shear. The latitudes at which the surface features arise cannot be probed using this method and the distribution of stellar spots on the surface of a star is unknown. Therefore, the surface rotation profile cannot be probed.

If surface rotational shear is relatively small, then closely spaced peaks arising from latitudinal differential rotation can appear as a single broad peak in realistic observations. The broadness of a feature in Fourier space is also related to the lifetime of that feature in period space, limiting the inference of latitudinal shear from time series integrated photometry. [Aigrain et al. \(2015\)](#) compared methods of measuring rotation period and latitudinal shear using synthetic *Kepler* data. They found that no state-of-the-art method (e.g., those adopted by [Reinhold et al., 2013](#); [McQuillan et al., 2014](#); [Garcia et al., 2014](#)) are able to disentangle the effects of latitudinal differential rotation from the surface feature lifetime. Surface differential rotation cannot be accurately measured through this method.

Asteroseismic inversions of latitudinal differential rotation prove to be somewhat fruitful in measuring the evolution of latitudinal differential rotation. [Benomar et al. \(2018\)](#); [Bazot et al. \(2019\)](#); [Hall et al. \(2021\)](#) were able to perform inversions of the rotational splittings of main-sequence stars using *Kepler* data. Their combined sample includes 14 stars with significant detection of equator-fast differential rotation. They also report a number of other stars investigated show limited evidence of equator-fast and equator-slow latitudinal rotation. The significance of detection is related to the scale of the latitudinal shear. This complicates the inference of the evolution of latitudinally-flat and equator-slow differential rotation profiles, which tend to express small scales of latitudinal shear. Further, their investigations are limited to a small number of stars that have long-baseline time-series photometric observations that express solar-like oscillations below the Nyquist frequency of *Kepler*. This limits our understanding to, essentially, solar analogues.

1.2.3 Effects of rotation on low-mass evolution

Compared to high-mass rotating stellar evolution, the indicators of low-mass rotating stellar evolution are minimal (see, e.g., [Heger et al., 2000](#); [Maeder & Meynet, 2000](#)). The rotation rate

is the main observable property of the evolution of rotation in stars. As this was discussed in length in Section 1.2, we will focus here on the impact of rotation on other observable quantities and stellar evolution.

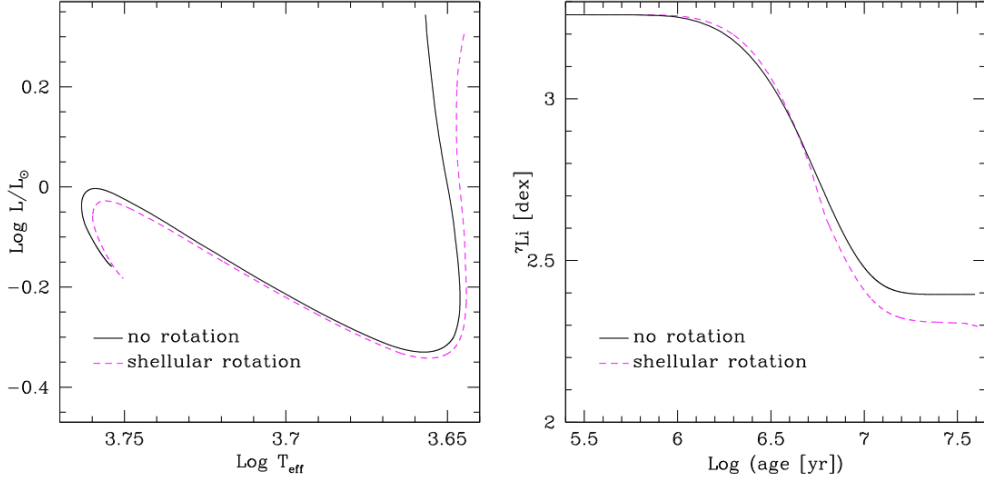


FIGURE 1.13: Effect of rotation on post-main-sequence evolution of stars. Left: PMS HR diagram tracks of $1 M_{\odot}$ solar metallicity models with and without rotation. The continuous line corresponds to a non-rotating model, while the dashed line corresponds to a rotating model with $\Omega = 20 \Omega_{\odot}$. The tracks end when the ZAMS is reached. Right: Surface lithium abundance with time during the PMS for the same models. Sourced from Figure 1 in [Eggenberger \(2013\)](#)

Figure 1.13 (left) compares the evolutionary track of a rotating solar-type, $1M_{\odot}$, solar metallicity, star rotating with $20 \Omega_{\odot}$ (twenty times the mean solar surface rotation rate), against a non-rotating model of the same mass and metallicity. Because of the introduction of the centrifugal force, the star's path on the Hertzsprung-Russel (HR) diagram is slightly shifted towards lower effective temperatures and luminosities than a non-rotating star.

During the pre-main-sequence, both the changes to the rotation impact the observed lithium abundances, which are dependent on the treatment of angular momentum transport ([Dumont et al., 2021](#)). Figure 1.13 (right) displays the evolution of surface lithium abundance during the PMS phase for rotating and non-rotating models. The zero-age-main-sequence (ZAMS) surface lithium abundance of the rotating model is lower than that of the non-rotating model, indicating that including rotational effects increases lithium depletion during the PMS. However, during the beginning of the lithium depletion phase, the rotating model shows a slightly higher lithium content than the non-rotating model due to the centrifugal force lowering the temperature at the base of the convective envelope.

As the star develops a radiative zone at its centre, rotational mixing becomes the dominant factor in transporting lithium to deeper and hotter regions, where it is efficiently destroyed. This leads to a lower surface lithium abundance for the rotating model on the ZAMS compared to the

non-rotating model, due to the increase in differential rotation in the stellar interior during the PMS.

The duration of the disk-locking phase, which enhances differential rotation in the radiative zone, significantly impacts the sensitivity of the lithium content in rotating models. Longer disklifetimes lead to lower surface lithium abundances on the ZAMS due to increased angular velocity gradients below the convective envelope, which enhance rotational mixing (Eggenberger et al., 2012). Moreover, as the star loses more angular momentum during the longer disk-locking phase, it reaches the ZAMS with a lower surface rotational velocity, resulting in lower lithium abundance. Therefore, a correlation between the surface velocity and lithium abundance on the ZAMS exists: stars with lower rotation rates on the ZAMS are expected to be more depleted in lithium than fast rotators on the ZAMS.

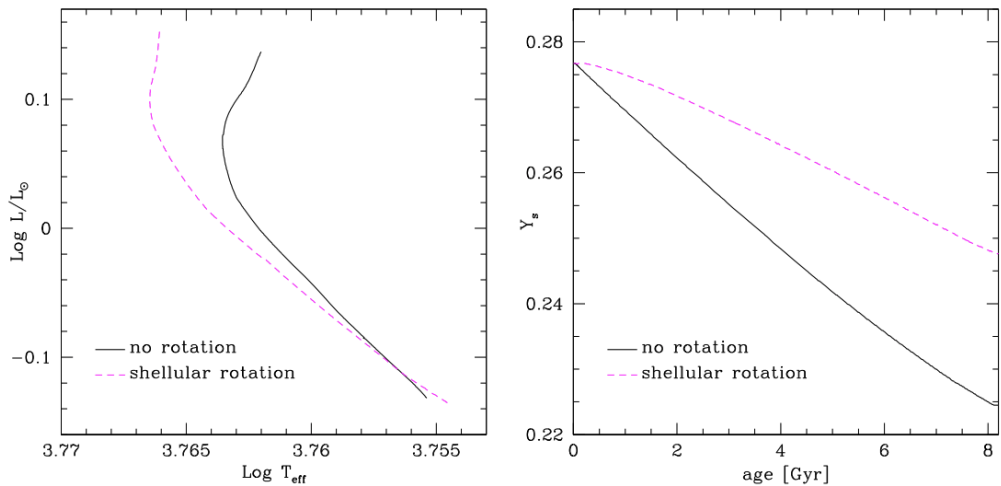


FIGURE 1.14: Left: MS HR diagram tracks of $1 M_{\odot}$ solar metallicity models with and without rotation. The continuous line corresponds to a non-rotating model, while the dashed line corresponds to a rotating model with ZAMS surface velocity 50 km s^{-1} . The tracks end when the ZAMS is reached. Right: Surface He abundance with time during the MS for the same models.

Sourced from Figure 3 in Eggenberger (2013)

During the main-sequence, rotational mixing begins to play a key role by changing a number of global stellar properties. This is illustrated in Figure 1.14 (left), which shows the main-sequence evolution for two $1 M_{\odot}$, solar metallicity models computed with and without rotation. The rotating model has an initial surface velocity of 50 km s^{-1} . The rotating model is, like the PMS model, characterised by higher effective temperatures and slightly higher luminosities than the non-rotating model. Figure 1.14 (right) highlights that the presence of rotational mixing counteracts the impact of atomic diffusion in the star’s outer layers. This leads to higher He surface abundances for the rotating model than the non-rotating model. Consequently, the opacity in the external layers of the rotating model decreases, causing a shift towards the blue region of the HR diagram, as illustrated in Figure 1.14 (left). The differences in He content between rotating

and non-rotating stars become increasingly pronounced during the main-sequence, resulting in significant distinctions in the HR diagram.

The inclusion of rotation affects the properties of the central layers of the star. H is transported to the central core through rotational mixing, leading to a higher central H-mass fraction for rotating models than for models without rotation at a given age. This leads to an increase in their main-sequence lifetime.

Within the post-main-sequence, the rotation effects are similar to the main-sequence. When rotational effects are considered, the core-He-burning phase is shifted to higher luminosity values. These changes are due to rotational mixing, which brings fresh H into the convective core and transports He and other H-burning products in the radiative zone.

There are no other significant enhancements in chemical abundances (see Table 2 in [Lagarde et al., 2012](#)). Rotation can, however, substantially affect the asteroseismic properties of low-mass red-giant stars ([Lagarde et al., 2012](#); [Eggenberger et al., 2010](#)). In particular, rotation decreases the derived stellar mass and increases the age. Observation and identification of non-radial oscillation modes for red giants with moderate surface rotational velocities may be complicated due to non-negligible values of rotational splitting, which can be reached depending on the assumed rotation law in the convective envelope and the star's initial velocity.

Chapter 2

Constraining the Rotation Profile in a Low-Luminosity Subgiant with a Surface Rotation Measurement

Preamble

Asteroseismic inference of the core and surface rotation of low-luminosity subgiants reveals that the core-to-surface rotation rate ratio is much smaller than state-of-the-art models of rotating stellar evolution predict (Deheuvels et al., 2014; Cantiello et al., 2014; Eggenberger et al., 2019). This result implies that there is missing physics in our treatment of angular momentum transport. One way to determine the source of the missing angular momentum transport is to look for signatures of those mechanisms in the shape of the rotation profile. However, due to the limited number and low precision of observed rotational splitting of low-luminosity subgiants, constraints to the rotation profile are usually limited to two-zone (core and surface rotation rate) inferences (Deheuvels et al., 2014).

We find, assuming a model-motivated step-function rotation profile, a consistent degeneracy between the surface rotation rate and radial position of a strong rotational gradient when performing asteroseismic inference using the observed rotational splittings of a low-luminosity subgiant. We show that we can leverage this degeneracy to place stronger constraints on the position of the strong rotational gradient with independent measurements of the surface rotation rate assuming representative precision. Furthermore, we apply this approach to the observed rotational splittings and surface rotation rate of low-luminosity subgiant KIC 12508433 and obtain stronger constraints to the internal rotation profile. We find decreased support for rotation profiles with strong rotational gradients in the core and $r/R > 0.4$, which suggests the data disfavours angular momentum transport via internal gravity waves (e.g., Pinçon et al., 2017)

or magnetorotational instabilities (e.g., Spada et al., 2016; Menou & Mer, 2006). The method applied in this work can readily be adopted in other works to more tightly constrain the internal rotation profiles of post-main sequence stars without the requirement for more data.

The content of this chapter was originally published as:

[Wilson, Casey, Mandel, Ball, Bellinger & Davies \(2023\)](#)

and is presented here in the form of a chapter for stylistic purposes in accordance with Monash University's thesis by submission guidelines.

Abstract

Rotationally-induced mode splitting frequencies of low-luminosity subgiants suggest that angular momentum transport mechanisms are 1-2 orders of magnitude more efficient in these stars than predicted by theory. Constraints on the rotation profile of low-luminosity subgiants could be used to identify the dominant mechanism for angular momentum transport. We develop a forward model for the rotation profile given observed rotational splittings, assuming a step-like rotation profile. We identify a consistent degeneracy between the position of the profile discontinuity and the surface rotation rate. We perform mock experiments that show the discontinuity position can be better constrained with a prior on the surface rotation rate, which is informed by star spot modulations. We finally apply this approach to KIC 12508433, a well-studied low-luminosity subgiant, as an example case. With the observed surface rotation prior, we obtain a factor of two increase in precision of the position of strong rotation gradient. We recover the literature values of the core and surface rotation rates and find the highest support for a discontinuity in the radiative zone. Auxiliary measurements of surface rotation could substantially improve inferences on the rotation profile of low-luminosity subgiants with already available data.

2.1 Introduction

All stars rotate. The rotation rate and distribution of angular momentum throughout a star evolves with time. The effects of rotation on the structure and evolution of a star are substantial (e.g. [Heger, 1998](#); [Maeder & Meynet, 2000](#)), and accurate prescriptions of rotation in stellar models are important to reproduce observations, particularly asteroseismic measurements of oscillation modes.

Low-mass subgiants and low-luminosity red giants pulsate in mixed modes, which are sensitive to structure in both the core and envelope. Mixed modes result from the near-surface convection, which drives the oscillation modes to amplitudes that are detectable in space-based photometry missions like *CoRoT* ([Baglin, 2003](#)) and *Kepler* ([Borucki et al., 2010](#)). Rotation lifts the degeneracy of oscillation modes of the same angular degree and azimuthal order. The change to the frequency of rotationally split modes is related to the rotation profile. For this reason, measuring rotational splittings allows us to constrain the rotation profile.

Current measurements of rotational splittings place low precision constraints on the core and surface rotation rates ($\approx 10\%$ and 30% respectively (e.g. [Deheuvels et al., 2014](#); [Fellay et al., 2021](#))) and have little capability to constrain the shape of the rotation profile connecting the core and the surface. These observations, however, present some notable results. Subgiants demonstrate solid-body rotation early in their transition off the main-sequence (MS), like their

MS counterparts (Deheuvels et al., 2020; Noll et al., 2021). However, later in their post-MS evolution, the cores of more evolved subgiants and low-luminosity red giant branch (RGB) stars rotate much faster than their envelope. The core-to-surface rotation ratio can grow to ≈ 20 for stars leaving the subgiant phase (Deheuvels et al., 2014; Gehan et al., 2018; Eggenberger et al., 2019).

Stellar models predict differential rotation between the core and the surface to be two to three orders of magnitude greater than observations suggest (Eggenberger et al., 2012; Cantiello et al., 2014). The surface rotation rates of white dwarfs agree well with the core rotation rates of RGB stars (Gough, 2015; Hermes et al., 2017b), suggesting an angular momentum transport mechanism that is much more efficient throughout the first ascent of the RGB, and nowhere else (Eggenberger et al., 2012; Marques et al., 2013; Ceillier et al., 2013; Fuller et al., 2015; Spada et al., 2016; Ouazzani et al., 2019).

The angular momentum transport mechanism sets the rotation profile. The core-to-surface rotation ratio and the position and strength of the gradient of rotation rate can characterise the rotation profile. Fellay et al. (2021) suggest that tighter constraints can be made on angular momentum transport mechanisms through more precise measures of the core-to-surface rotation ratios of post-MS stars (Deheuvels et al., 2014), and of the position and strength of a rotation rate gradient (Di Mauro et al., 2018). For example, a rotation profile with a constant rotation rate internal to the base of the convective zone (BCZ), and a decreased rotation rate that is inversely dependent on radius in the convective zone, could be indicative of angular momentum transport from deep fossil magnetic fields (Gough & Thompson, 1990; Kissin & Thompson, 2015; Takahashi & Langer, 2021). This results from differential rotation being damped along poloidal field lines (Garaud, 2002; Strugarek et al., 2011). On the other hand, a steep rotational gradient near the H-burning shell of a subgiant would indicate turbulent angular momentum transport. This could be in the form of internal gravity waves (Pinçon et al., 2017), leading to localised shallow gradients in the profile (Charbonnel & Talon, 2005) or through magneto-rotational instabilities which arise from steep angular momentum gradients (Spada et al., 2016; Balbus & Hawley, 1994; Arlt et al., 2003; Menou & Mer, 2006). The gradient of the rotation profile of subgiants is not well constrained through current asteroseismic data (Deheuvels et al., 2014).

In this work, we consider the constraints to the position of a steep rotational gradient, where we show that $\ell = 1, 2$ rotational splittings may be sufficient to make valuable inferences about the rotation profiles of low-luminosity subgiants if a precise auxiliary measure of surface rotation rate is available. We specifically investigate the impact of employing surface rotation periods from photometric variability owing to stellar spots (e.g. those measured in McQuillan et al., 2014; Garcia et al., 2014; Santos et al., 2021). In adopting these values, we utilise a data set that overlaps with the subset used to measure asteroseismic rotational splittings. We deem it

appropriate to employ both constraints simultaneously due to the distinct methods of measuring these quantities.

In Section 2.2 we describe a forward model to infer rotation profile parameters given observed rotational splittings, assuming a step rotation profile. We perform tests using mock data generated by three hypothetical profiles to show the differences in constraining the rotation profile with realistic independent measures of surface rotation rate from stellar spot brightness modulations. Finally, we perform inference on the observed rotational splittings of KIC 12508433 with different priors and compare the constraints on the rotation profile. The implications are discussed in Section 2.4, and summarised in Section 2.5.

2.2 Method and results

2.2.1 Rotational splittings

Stellar oscillations can be decomposed into oscillating spherical harmonic modes. Individual modes frequencies ($v_{n,\ell,m}$) are characterised by their radial order (n), angular degree (ℓ) and azimuthal order (m). Low-luminosity subgiants have much longer rotation periods (of order 10^1 days (Deheuvels et al., 2014)) in the fast rotating core than the average oscillation period (on the order of hours (Aerts et al., 2010)). We can therefore treat rotation as perturbative to the structure. The effect of stellar rotation on oscillation mode frequencies can be approximated as perturbations to the non-rotating mode frequencies from $m = 0$ to $m = -\ell$ and $m = \ell$. This is a widely employed approximation in the field of asteroseismic inversions of rotation (e.g. Deheuvels et al., 2014, 2015; Fellay et al., 2021). For more detail on this approach see Unno et al. (1979); Aerts et al. (2010). To first order, the rotationally split oscillation frequencies are

$$v_{n,\ell,m} = v_{n,\ell,0} + \delta v_{n,\ell,m} \quad (2.1)$$

$$= v_{n,\ell,0} + m \delta v_{n,\ell} \quad (2.2)$$

where $v_{n,\ell,m}$ is the frequency of the n, ℓ, m mode, $v_{n,\ell,0}$ is the frequency in the non-rotating case, and $\delta v_{n,\ell,m}$ is the change in oscillation frequency due to rotation, known as the rotational splitting. The difference between the $m = 0$ and $m \neq 0$ mode frequency is the m 'th multiple of the $\delta v_{n,\ell}$ rotational splitting. In practice we are usually only able to observe $\ell = 1$ and $\ell = 2$ modes with $m = 1$ and $m = -1$ rotational splittings in low-luminosity subgiants from photometric time series data (Benomar et al., 2013; Deheuvels et al., 2014).

Rotational splittings are scaled averages of the rotation profile. The scaling is different for each oscillation mode and is quantified using a so-called rotational kernel. The rotational kernels are inherent to the thermodynamic structure of a star (see Aerts et al., 2010, for a derivation of these

kernels). Assuming spherical symmetry, the n, ℓ rotational splitting is given by

$$\delta v_{n,\ell}(\Omega) = \beta_{n,\ell} \int_0^R K_{n,\ell}(r) \Omega(r) dr \quad (2.3)$$

where $K_{n,\ell}$ is the rotational kernel of the n, ℓ mode (determined from a stellar model), $\Omega(r)$ is the scaled average, with respect to the polar axis, 1D rotation profile along the radial axis, $\beta_{n,\ell}$ is a normalisation constant, and R is the outermost radius of the star. The rotational kernel, and thus scaled averaged frequency shift, changes with each oscillation mode. Changes to the rotation profile therefore result in distinct variances for each rotational splitting. Some rotation profiles are more likely to result in measurable rotational splittings than others. As a result we are able to use forward modelling to determine the set of likely rotation profiles given some observed rotational splittings.

2.2.2 Forward model

A forward model requires a set of rotation kernels to predict rotational splittings given some profile. In this work, we use rotational kernels of the low-luminosity subgiant KIC 12508433, a well-studied asteroseismic target (e.g., [Deheuvels et al., 2014](#)). Models of KIC 12508433 indicate that it is early in its evolution off the MS, which is supported by a relatively low core-to-surface rotation ratio. It is the earliest star known in its post-MS evolution with evidence of differential rotation.

We were provided with a model of KIC 12508433 from [Ball & Gizon \(2017\)](#) generated using the ASTERO module of the Modules for Experiments in Stellar Astrophysics (*MESA*) evolutionary code (r7624; [Paxton et al., 2010, 2013, 2015, 2019](#)). The model was found by simultaneously matching the non-seismic properties of KIC 12508433 (T_{eff} , $\log g$, and [Fe/H] in Table 2.1), the global seismic quantities - the frequency where peak power of the Gaussian asteroseismic power envelope occurs, v_{max} , and the frequency spacing between consecutive radial order modes with the same angular degree, Δv - and the observed mode frequencies (see Tables 1 and 3 in [Deheuvels et al., 2014](#)) to those predicted by the model. Mode frequencies were calculated using ADIPLS ([Christensen-Dalsgaard, 2008](#)), with combined surface effect corrections to the frequencies ([Ball & Gizon, 2014, 2017](#)).

Most of the observed and best-fit model quantities agree to within $1-\sigma$. The exceptions are T_{eff} and L where the agreement is within $2-\sigma$. Our model T_{eff} is closer to the reported T_{eff} from the infrared flux method ([Casagrande et al., 2010](#)) (5302 ± 124 K from [Deheuvels et al. \(2014\)](#)), but fully consistent with the spectroscopic effective temperature. L is not included in the χ^2 fitting of the model (M , R and L are outputs of the model) and the value from [Deheuvels et al. \(2014\)](#) was estimated from scaling relations. This level of deviation varies with surface modelling assumptions ([Ball & Gizon, 2017](#)), is consistent with previous works (e.g. [Deheuvels](#)

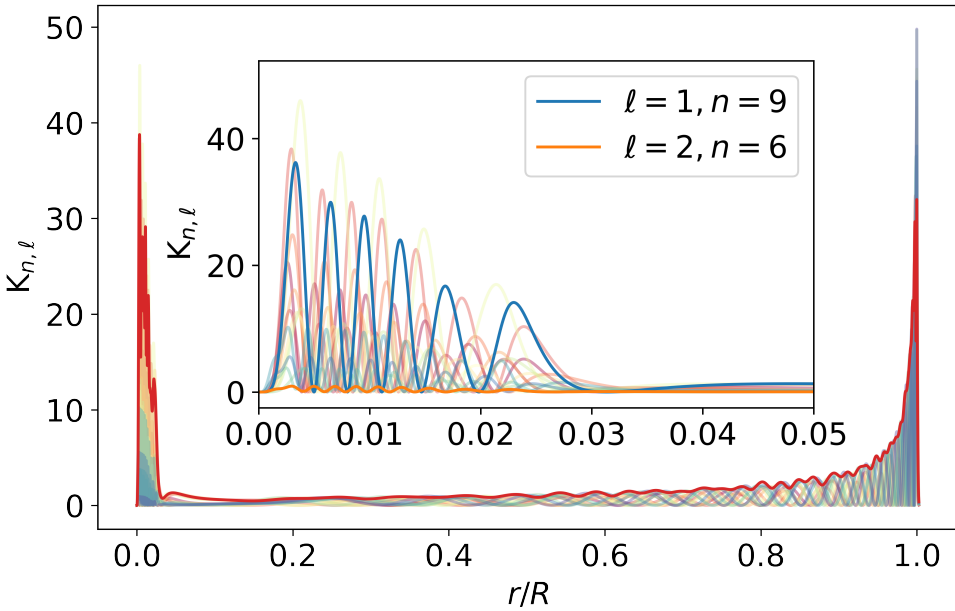


FIGURE 2.1: Rotational kernels for the best-fitting model of KIC 12508433. The red curve shows three times the local standard deviation of the set of observed kernels (kernel deviation). Regions with large kernel deviation are expected to be sensitive to the rotation profile following forward modelling. In this model these regions can be seen in the H-burning shell core ($r/R < 0.05$) and nearing the surface ($r/R > 0.8$). The inset shows the same kernels with two modes highlighted: the $\ell = 1, n = 9$ mode (blue) is sensitive to core rotation and the $\ell = 2, n = 6$ (orange) is sensitive to surface rotation.

	KIC 12508433	Model
$M(M_\odot)$	1.20 ± 0.16	1.293
$R(R_\odot)$	2.20 ± 0.10	2.277
$L(L_\odot)$	3.25 ± 0.45	4.065
$\log g(\text{ cms}^{-2})$	3.83 ± 0.04	3.834
$T_{\text{eff,spec}}(\text{K})$	5248 ± 130	5434
[Fe/H] (dex)	0.25 ± 0.23	0.06

TABLE 2.1: Measured properties of KIC 12508433 (Deheuvels et al., 2014), and those of the best-fitting stellar model from which the rotation kernels are generated.

et al., 2014; Li et al., 2020a), and while rotational inversions of subgiants can be dependent on model uncertainties (Schunker et al., 2016) this discrepancy is unlikely to affect the results of this work.

We used this model of KIC 12508433 to calculate the rotational kernels for all observable rotational splittings. Radial positions with both high kernel magnitude and inter-kernel variance (represented by the standard deviation of kernel magnitudes, shown in red in Figure 2.1) are most sensitive to the rotation profile. For KIC 12508433 these regions are near the core and at $r/R > 0.8$.

[Deheuvels et al. \(2014\)](#) concluded that it is difficult to distinguish between smooth and discontinuous rotation profiles of low-luminosity subgiants using current data. Consequently, we assume a simple form of a rotation profile $\Omega(r)$ using three parameters of the following form:

$$\Omega(r) = \begin{cases} \Omega_c & r/R \leq p \\ \Omega_s & r/R > p \end{cases} \quad (2.4)$$

where Ω_c and Ω_s describe the core and surface rotation rates respectively, and p is the position of the step (in units of r/R). We discuss the implications of the assumed step-function form of the rotation profile further in Section 2.4. Initially we will assume weak uninformed, uniform priors on the core and surface rotation rate and a uniform prior on p :

$$p \sim \mathcal{U}(0, 1) \quad (2.5)$$

$$\Omega_s/2\pi \sim \mathcal{U}(0, 600) \text{ nHz} \quad (2.6)$$

$$\Omega_c/2\pi \sim \mathcal{U}(0, 1000) \text{ nHz} \quad (2.7)$$

where $\mathcal{U}(x, y)$ denotes a uniform prior between x and y . We calculate the expected rotational splitting frequencies $\delta v_{n,l}$ for all observable $\{n, l\}$ modes given a model $\Omega(r)$ and the rotational kernels $K_{n,\ell}(r)$ using Eq. 2.3, and assume the observed splitting frequencies are normally distributed with a log-likelihood

$$\ln \mathcal{L}(\boldsymbol{\delta v} | \Omega_c, \Omega_s, p, \mathbf{K}(\mathbf{r}), \boldsymbol{\sigma}_{\boldsymbol{\delta v}}) \propto -\frac{1}{2} \sum_{n,l} \left(\frac{\delta v_{n,l} - \delta v_{\text{obs } n,l}}{\sigma_{\delta v_{n,l}}} \right)^2 \quad (2.8)$$

where $\delta v_{\text{obs } n,l}$ is the observed rotational splitting frequency for mode n and l , and its associated uncertainty is $\sigma_{\delta v_{n,l}}$. The vector-valued symbols $\boldsymbol{\delta v}$, $\mathbf{K}(\mathbf{r})$, and $\boldsymbol{\sigma}_{\boldsymbol{\delta v}}$ indicate that the log-likelihood depends on the corresponding values for all of the observed rotational splittings. We constructed this model using PYMC3 ([Salvatier et al., 2016](#)) and used the ‘No U-Turn Sampler’ ([Hoffman & Gelman, 2014](#)) to draw samples from the posterior.

2.3 Results

2.3.1 Mock data experiments with three hypothetical rotation profiles

We begin by generating mock data with our forward model to test the impact of independent measures of surface rotation rate. We chose three rotation profiles with extreme differences in the position of a strong rotational gradient, which represent hypothetical angular momentum transport mechanisms that could result in step-like rotation profiles. The three step positions are: in the H-burning shell (purple); in the radiative zone (blue); and at the base of the convective

zone (red) as shown in Figure 2.2. The mock rotation profiles are motivated by, but not representative of, various angular momentum transport processes. The BCZ step rotation profile (red) is a signature of angular momentum transport by fossil magnetic fields, which results in solid body rotation in the radiative region and inverse rotation rate on radius in the convective region (Kissin & Thompson, 2015; Takahashi & Langer, 2021). The H-burning step rotation profile (purple) is indicative of turbulent angular momentum transport through internal gravity waves (Pinçon et al., 2017) or magneto-rotational instabilities (Spada et al., 2016; Balbus & Hawley, 1994; Arlt et al., 2003; Menou & Mer, 2006) which result in a strong gradient in rotation rate close to the core. The radiative zone step profile (blue) corresponds to delocalized angular momentum transport from the core into the radiative zone and is not indicative of a specific angular momentum transport process.

The core and surface rotation rates will be realistically different for each profile/angular momentum transport process. To account for this for each profile, we fixed the step position and evaluated the log-likelihood (given the observed splittings of KIC 12508433) at each combination of (Ω_c, Ω_s) and set the rotation rates to those with the maximum log-likelihood. The resulting rotation profiles are shown in Figure 2.2: radiative-zone step (blue: $p = 0.2$), a BCZ step (red: $p = 0.5$), and the H-burning shell step (purple: $p = 0.05$). The rotational splitting frequencies of these profiles were then calculated using (Eq. 2.3). We adopted uncertainties on those expected values given the precision of mode frequencies measured in KIC 12508433 (Table 3 of Deheuvels et al. (2014)). This provides us with three mock data sets to consider the rotation profile's effect on the observations.

We treated the mock data generated by each step profile as if it were real data and performed inference using the model and sampler described in Section 2.2.2. We performed inference twice: first with a flat prior on surface rotation and then with a Gaussian prior on surface rotation with mean equal to the injected surface rotation rate, and a standard deviation 10% of the mean value. Here we have chosen 10% as representative of the average uncertainty on state-of-the-art measurements of main-sequence and subgiant stellar rotation from photometric variation (Santos et al., 2021). We discuss this choice further in Section 2.4. We drew 20,000 posterior samples in each case. The 1D marginalised posterior samples with a flat and informed prior are compared in Figure 2.3. The full posteriors are shown in the Appendix (Figures 2.6 to 2.11).

When sampling with a uniform prior on surface rotation (Figures 2.6 to 2.8), we identify multimodality and a strong correlation between Ω_s and p : smaller Ω_s values tend to coincide with higher p values. The inferred step position p is very uncertain in all three cases, showing nearly uniform probability throughout the domain.

The impact of an auxiliary surface rotation rate measure on the posterior distributions is evident when comparing the normalised posterior density when using an uninformed prior (thin dashed) to the informed prior (thick solid) in Figure 2.3. When the informed prior is introduced, the

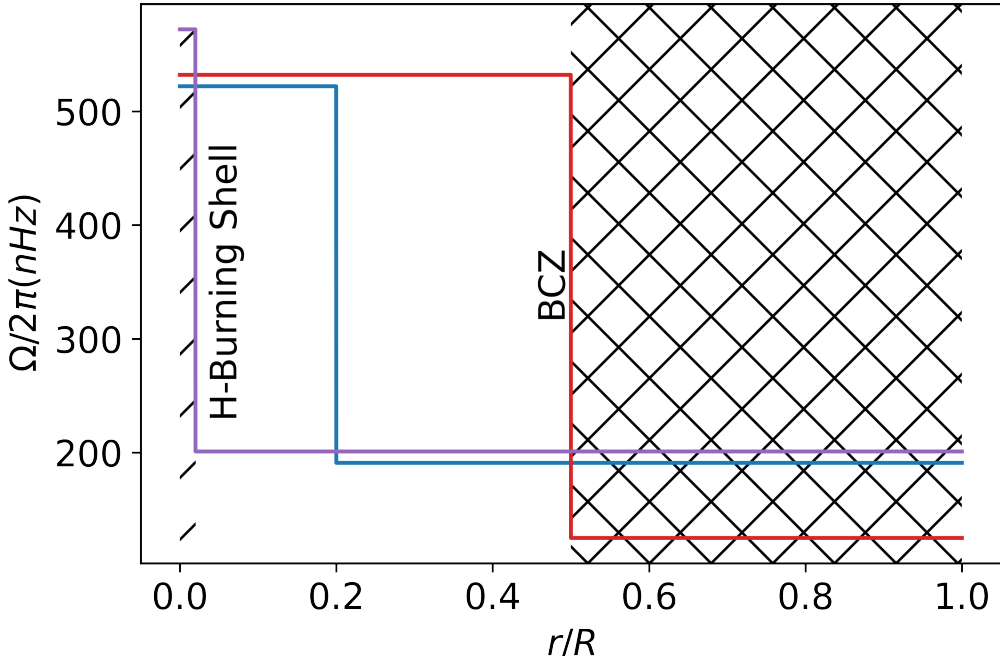


FIGURE 2.2: Three rotation profiles used in the mock data experiments. These profiles represent the extreme consequences of different angular momentum transport mechanisms in low-luminosity post-MS stars. Cross-hatching represents the convective surface region and diagonal-hatching represents the H-burning shell. See Section 2.3.1 for descriptions of each profile.

degeneracy between surface rotation rate and p is broken and the surface rotation rate and p are better recovered. In the H Shell step (purple) and radiative step (blue) experiments, the prior has collapsed support for $p > 0.4$. The introduction of the prior does not, however, allow us to differentiate between rotation profiles deeper in the star. We find that for profiles where $p \lesssim 0.2$, multi-modality remains and the introduction of the prior on Ω_s increased support for p closer to the core (and closer to the true value). Indeed the introduction of the informed prior for the H shell and radiative step experiments has constrained the posterior on p , but the 1σ range on these values overlaps significantly. We could not differentiate between these profiles using this method and state-the-art data. This is not the case for the BCZ mock data experiment. Introducing the informed surface rotation prior allows us to place more significant constraints on p . The posterior on p was flat with an uninformed prior and the BCZ step. In contrast, with a surface rotation rate prior, the posterior is now a single peak centred at the injected value with a percentage standard deviation of the median value of about 18%. This illustrates the constraining power on p of the independent measures of Ω_s in specific circumstances.

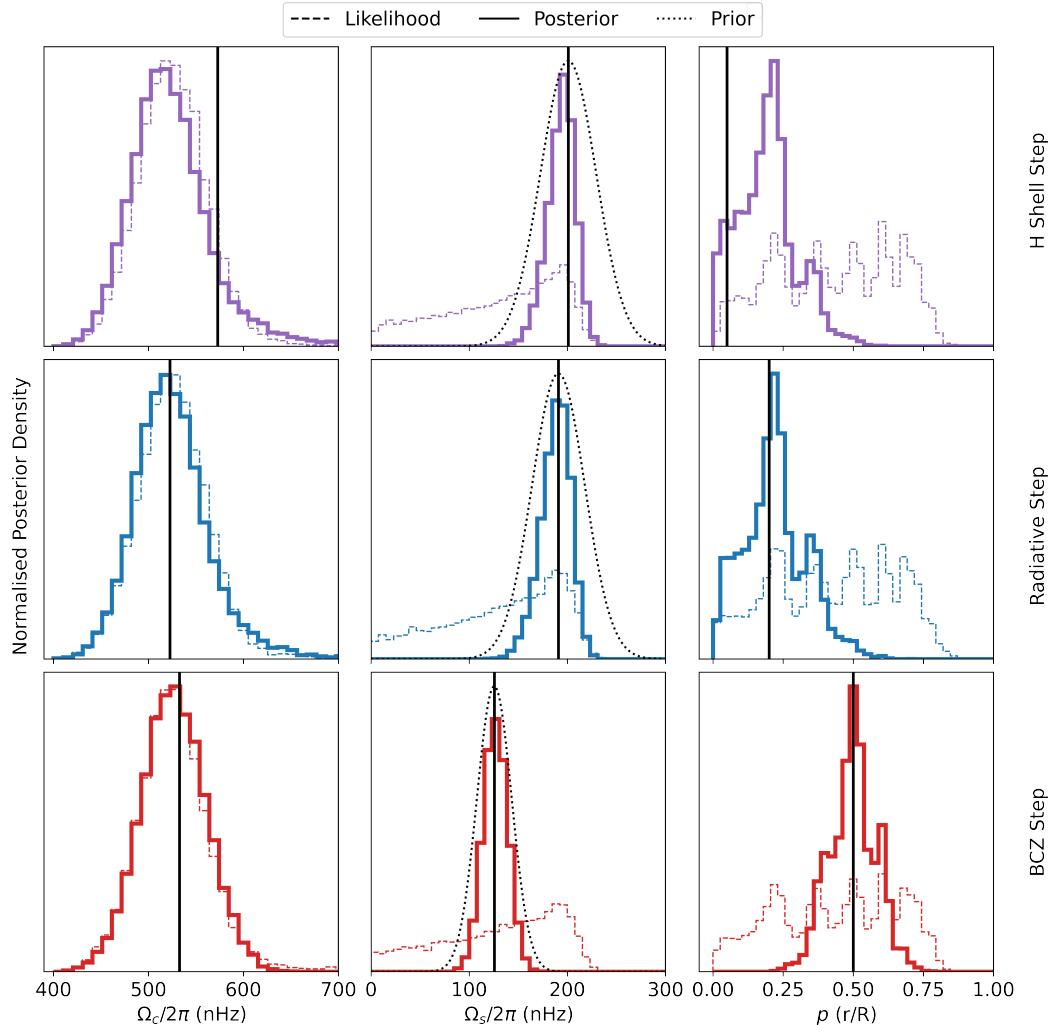


FIGURE 2.3: Normalised posterior density following sampling for each *mock* rotational splitting experiment. From left to right the normalised posterior density of each of the parameters of the rotation profile model are shown: surface rotation rate ($\Omega_s/2\pi$), core rotation rate ($\Omega_c/2\pi$), and position of rotational gradient (p). Thin coloured dashed lines are samples with no prior on the surface rotation rate, thin dotted black lines correspond to the introduced prior on surface rotation rate and thick coloured lines correspond to samples when the informed surface rotation prior was introduced. Vertical black lines correspond to the input values for each of the rotation profile parameters used to generate the mock rotational splittings. From top to bottom each row displays the result of sampling a different set of rotational splittings with the same colours as the rotation profiles used to generate the mock data in Figure 2.2: the H-burning shell step (purple), radiative zone step (blue) and base of convective zone step (red).

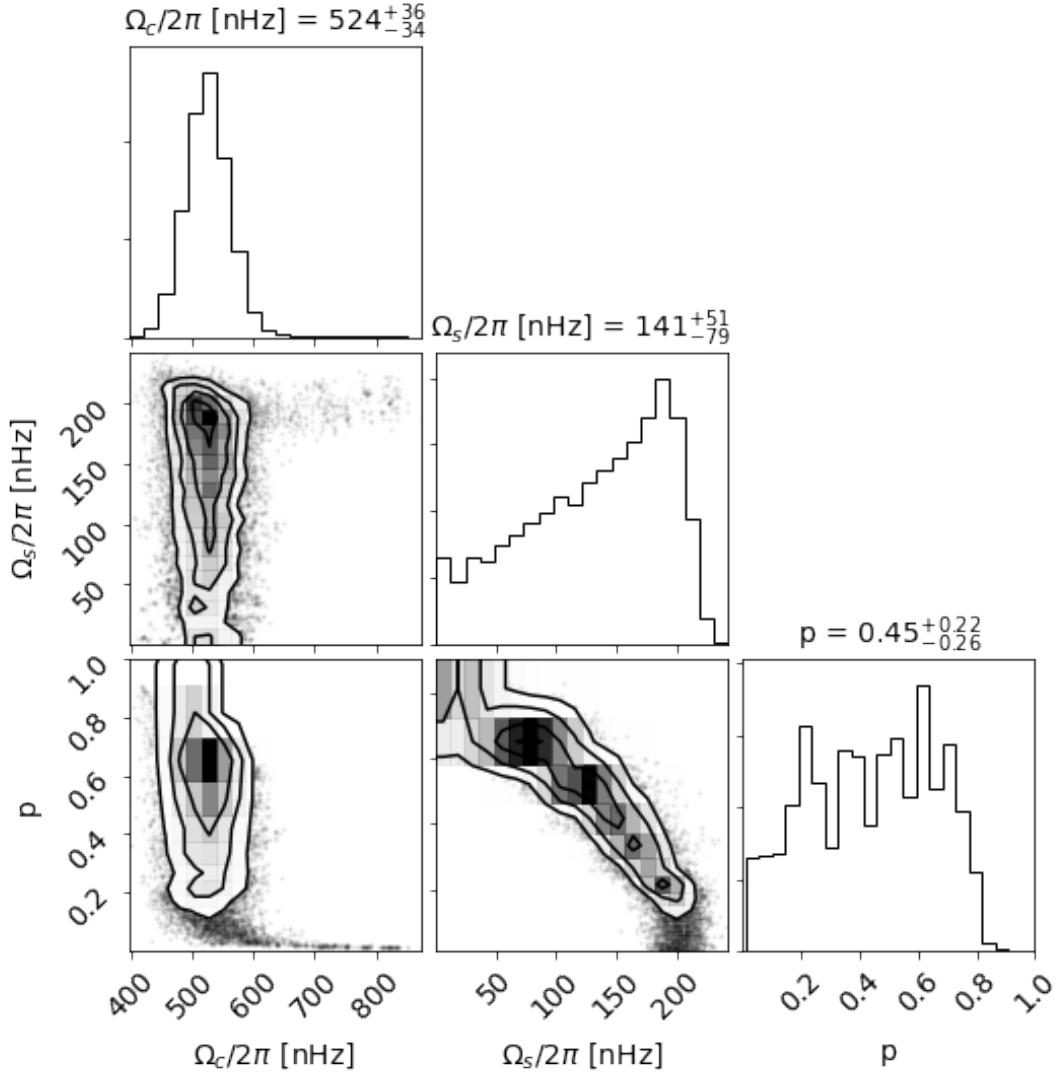


FIGURE 2.4: Posterior distributions of the core rotation rate Ω_c , the surface rotation rate Ω_s , and the discontinuity position p (Eq. 2.4) given the observed $l = \{1, 2\}$ rotational splittings of KIC 12508433 and assuming a rotation profile with a step function.

2.3.2 KIC 12508433

Our mock data experiments confirm that a realistic measure of surface rotation rate, treated as a prior during inference can better constrain the internal rotation profile. We now apply this method to observed rotational splittings of KIC 12508433 (Deheuvels et al., 2014). First with a uniform prior on surface rotation between 0 and 600 nHz, and then with an independent surface rotation rate (measured by Garcia et al., 2014, from photometry) treated as a Gaussian prior on the surface rotation rate with mean 172 nHz and standard deviation 21 nHz. The posteriors are shown in Figures 2.4 and 2.5. The best-fitting values and credible intervals of the rotation profile parameters for each prior are shown in Table 2.2 and are compared to the results of optimally localised average (OLA) inversions performed in Deheuvels et al. (2014).

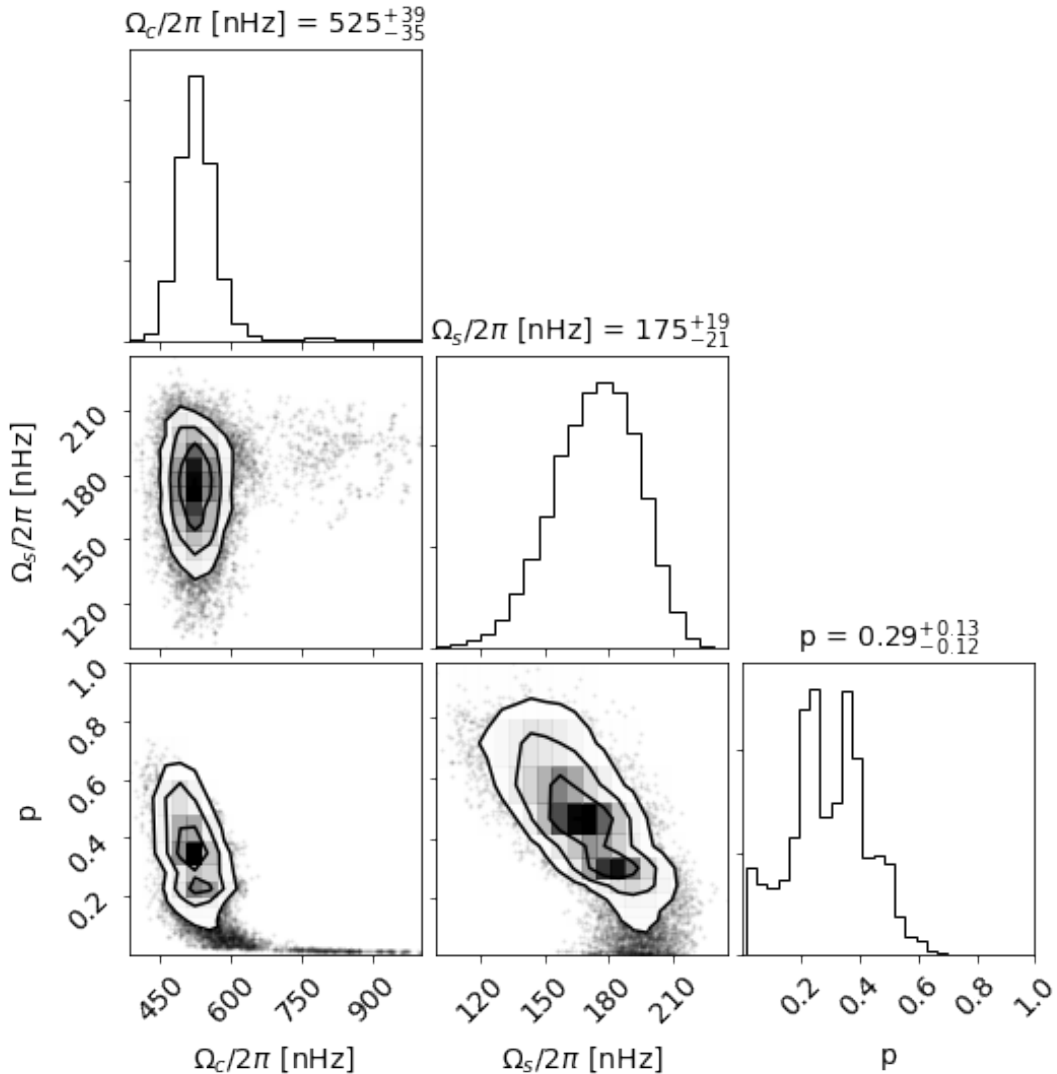


FIGURE 2.5: Posteriors on step profile parameters given the rotational splittings of KIC 12508433 and informed prior on surface rotation rate from (Garcia et al., 2014).

	$\Omega_c/2\pi$ (nHz)	$\Omega_s/2\pi$ (nHz)	p (r/R)
Deheuvels et al. (2014) (OLA)	532 ± 79	213 ± 26	...
Sampling - Flat Ω_s Prior	524^{+36}_{-34}	141^{+51}_{-79}	$0.45^{+0.22}_{-0.26}$
Sampling - Informed Ω_s Prior	525^{+39}_{-35}	175^{+19}_{-21}	$0.29^{+0.13}_{-0.12}$

TABLE 2.2: Best-fitting rotation profile parameters given observed $\ell = 1$ and 2 rotational splittings of KIC 12508433 from optimally localised averages (OLA) (Deheuvels et al., 2014) and forward modelling with flat and informed ($\Omega_s/2\pi = 172 \pm 21$ nHz) priors. OLA does not place constraints on the rotation profile outside the g- and p-mode cavities in the core and at the star's surface, respectively. p is more precisely measured with the introduction of the informed prior when forward modelling.

With a uniformed prior, the median of the posterior on the core and surface rotation rates and corresponding 16th and 84th percentile credible intervals are $\Omega_c/2\pi = 524^{+36}_{-34}$ nHz and $\Omega_s/2\pi = 141^{+51}_{-79}$ nHz, with the maximum a posteriori or MAP point at $\Omega_c/2\pi \approx 520$ nHz and $\Omega_s/2\pi \approx 170$ nHz. With the informed surface rotation rate prior the 16th and 84th percentile credible intervals are $\Omega_c/2\pi = 525^{+39}_{-35}$ nHz and $\Omega_s/2\pi = 175^{+19}_{-21}$ nHz. The inferences agree with each other, as well as the inversions performed in [Deheuvels et al. \(2014\)](#). Those authors use OLA to estimate the mean rotation rate in the g-mode cavity to be $\langle \Omega_g \rangle / 2\pi = 532 \pm 79$ nHz and the mean rotation rate in the p-mode cavity to be $\langle \Omega_p \rangle / 2\pi = 213 \pm 26$ nHz. Taking their Ω_g and Ω_p as analogues for Ω_c and Ω_s , respectively, both sets of quantities agree within about one joint standard deviation, without considering that the *mode* of the Ω_s posteriors are closer to $\langle \Omega_p \rangle$ than the median of Ω_s .

Like in the mock data experiments, the independent surface rotation measure removed support for discontinuities close to the BCZ (comparing Figures 2.4 and 2.5), but two peaks remain: $p \approx 0.25$ (closest to the median posterior value and a peak in the posterior when considering a flat prior on Ω_s) and a much smaller peak closer to the core. Rotation profiles with a discontinuity located $p > 0.4$ for KIC 12508433 is strongly disfavoured, and a discontinuity in the radiative region $0.2 r/R$ is favoured. Comparing the confidence intervals when applying a flat and informed prior, we obtain a factor of approximately two increase in measurement accuracy on p .

2.4 Discussion

We find that a surface rotation rate measured from star spot modulations can substantially improve inferences on the rotation profiles of low-luminosity subgiants. This takes advantage of a degeneracy between Ω_s and p , found by performing inference using mock experiments with different discontinuity positions.

Including an independent measure of surface rotation as a prior in the analysis of KIC 12508433 yields increased support for step-like profiles with rotational gradients in the radiative zone and decreased support for step-like rotation profiles with $p \gtrsim 0.4$.

In our mock data tests, we proposed that a step-like rotation profile with a rotational gradient at $0.5 r/R$ (BCZ profile) is motivated by, but not representative of, angular momentum transport by fossil magnetic fields. However, the simplified step rotation profile does not accurately recreate the inverse dependency of rotation rate with radius beyond the BCZ indicative of this angular momentum transport process. Further, the signature rotation profile becomes most apparent in the red giant branch ([Takahashi & Langer, 2021](#); [Fellay et al., 2021](#)). Therefore, we are not

proposing a lack of support for eliminating fossil magnetic fields as a possible explanation for the subgiant angular momentum transport problem.

The auxiliary measure of surface rotation we adopt as a surface rotation rate prior requires some discussion. The 'data' we use are rotational splitting frequencies measured from a Fourier transform of a photometric time series. The measured surface rotation rate from [Garcia et al. \(2014\)](#) also uses some subset of the same photometric time series data. The two sets of measurements are not strictly statistically independent, such that there is a risk that we are 'stealing information'. The two approaches do use subsets of the same data set, but the methods are sufficiently distinct that we consider it reasonable to use the surface rotation rate here.

[Santos et al. \(2021\)](#) suggest that the average percentage uncertainty on photometric surface rotation measurements is $\sim 10\%$ for main-sequence and subgiant stars. The precision varies with temperature, and peaks around 6000 K (the Kraft break). Those authors also concluded that only about 20% of subgiants with long and precise photometric observations from *Kepler* have measurable rotation periods. Subgiants may express smaller, shorter-lived active regions, which, when combined with long rotation periods, would present a smaller observable fraction and less precise measures of the surface rotation rate when compared to main-sequence counterparts. On the other hand, observing rotational splittings in subgiants requires a long observation time, which may lend itself to a higher fraction with measurable surface rotation rates.

It's difficult to precisely measure the surface rotation rate without using photometry. Rotational velocity ($v \sin i$) only requires a single high-resolution spectrum, but requires an estimate of the inclination angle and the star's radius, which is quickly changing in the post-MS and is strongly model dependent.

We assumed a step-like (discontinuous) function for the rotation profile, consistent with other works (e.g., [Fellay et al., 2021](#)). Realistically this may not reflect the true shape of the rotation profile of any low-luminosity subgiant. Asteroseismic forward modelling of the stellar rotation profile is an ill-posed problem. The observed rotational splittings alone do not uniquely determine the shape of a star's rotation profile. An assumption of the rotation profile's shape is necessary for the rotational splittings to constrain the range of possible rotation profile parameters. A much more flexible model than the step-like rotation profile could be employed. However, the inferences must be interpreted in the context of the realistic evolution of angular momentum transport. Ultimately, our work exemplifies that introducing an informed surface rotation prior further reduces the potential rotation profiles already constrained by asteroseismic data. Combining state-of-the-art asteroseismic and surface rotation data is a practical method to obtain more substantial constraints to the evolution of rotation from already available data.

In this work, we take KIC 12508433 as an example of a low-luminosity giant with asteroseismic observations. It is not yet clear whether the degeneracy between surface rotation and step

position generalises across all subgiants of different masses, metallicities, and ages. Very few subgiants are known to have mode measurements suitable for this kind of inference. Further work is needed.

2.5 Conclusions

We investigate the impact of independent surface rotation rate priors on inference of the rotation profile of subgiant stars. We perform forward modelling of the rotation profile given observations of rotational splittings assuming a step function rotation profile. Under these assumptions, we identify a degeneracy between the surface rotation rate and the position of the strong gradient. Mock experiments show that the introduction of a prior on surface rotation breaks the degeneracy, allowing us to place stronger constraints on the position of the gradient.

We introduce an independent measure of surface rotation from star spot photometric modulations as a prior when performing inference on the rotation profile of KIC 12508433. We find that introducing the independent measure of surface rotation increases the measurement precision on the position of the rotational gradient by a factor of two and that the data strongly disfavours discontinuities outside $r/R = 0.4$ in KIC 12508433. Including auxiliary surface rotation measurements when performing asteroseismic forward modelling of the rotation profile is a simple way of extending what we can learn from each star with existing data.

Appendix

Sampling Results

Here we provide the posteriors following sampling of each set of rotational splittings.

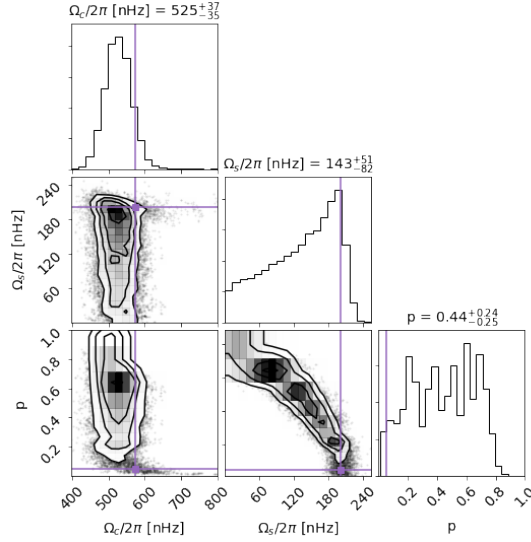


FIGURE 2.6: Posterior distributions using mock data generated with a step function aligned with the H burning shell ($r/R = 0.05$, purple profile in Figure 2.2). True values are indicated in purple. There is considerable multi-modality and degeneracy present.

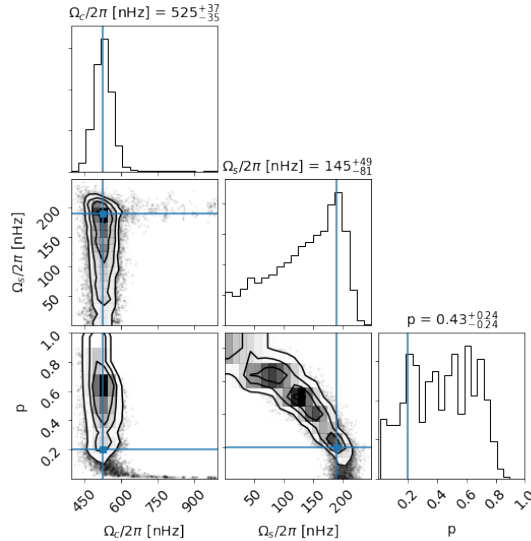


FIGURE 2.7: Posterior distributions using mock data generated with a step function in the radiative region ($r/R = 0.2$, blue profile in Figure 2.2) and realistic uncertainties. True values in blue.

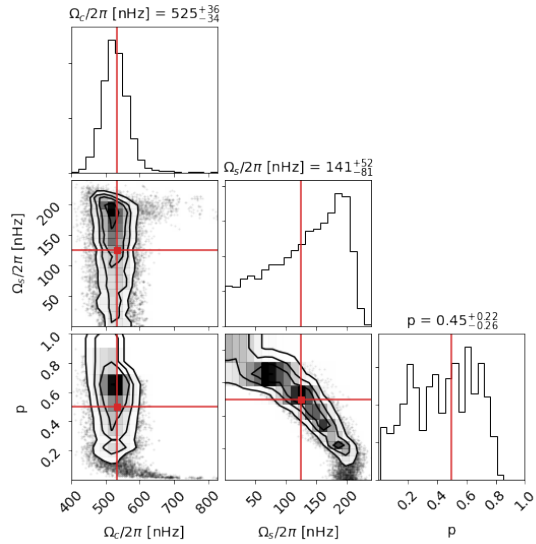


FIGURE 2.8: Posterior distributions using mock data generated with a step function at the BCZ ($r/R = 0.5$; red profile in Figure 2.2), and realistic uncertainties. True values in red.

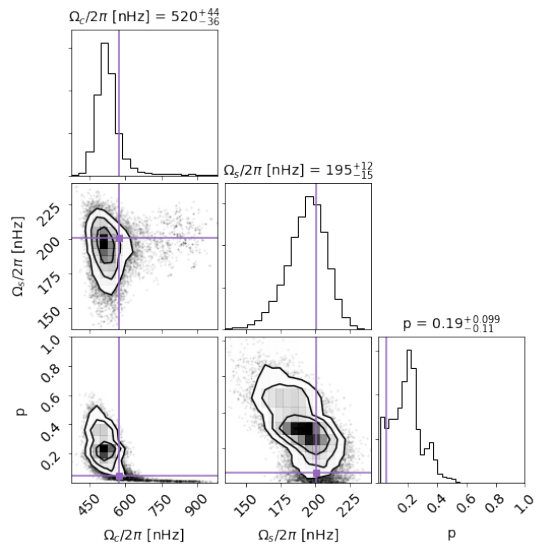


FIGURE 2.9: Posterior distributions using mock data generated with a step profile at the g-mode cavity ($r/R = 0.05$; purple profile in Figure 2.2), with realistic uncertainties, and a 10% prior on surface rotation Ω_s . There is still degeneracy between p and the rotation parameters (e.g., Figure 2.6), but the prior has collapsed all other modes.

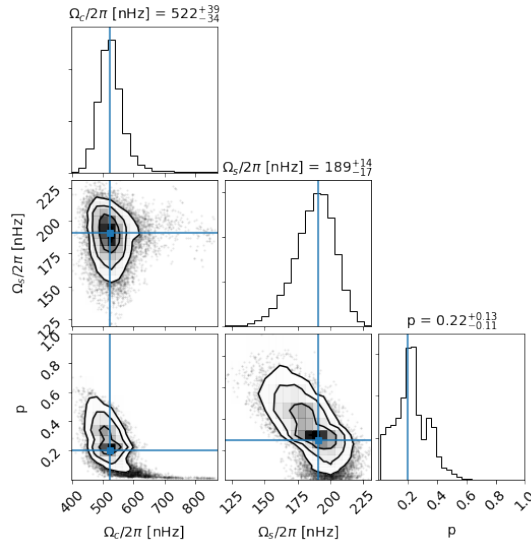


FIGURE 2.10: Posterior distributions using mock data generated with a step profile in the radiative region ($r/R = 0.20$; blue profile in Figure 2.2), with realistic uncertainties, and a 10% prior on surface rotation Ω_s (compare with Figure 2.7).

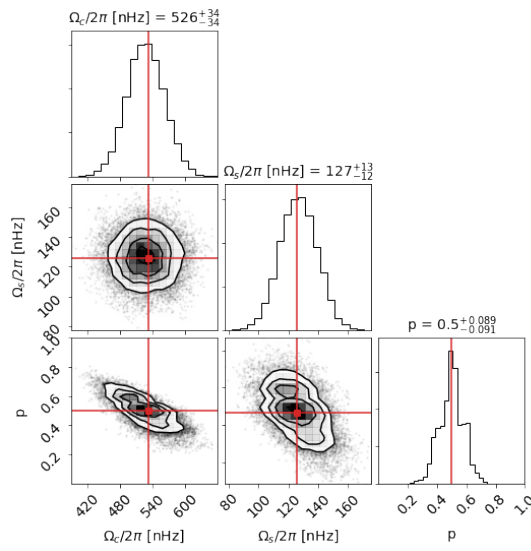


FIGURE 2.11: Posterior distributions using mock data generated with a step profile at the BCZ ($r/R = 0.50$; red profile in Figure 2.2), with realistic uncertainties, and a 10% prior on surface rotation Ω_s (compare with Figure 2.8).

Chapter 3

Stellar spots cause measurable variations in atmospheric metallicity

Preamble

The effects of rotation can permeate astronomy in unexpected ways. The number of stellar spots expressed by stars is directly tied to the surface rotation rate through increased magnetic field strength. Stars with relatively fast rotation rates express larger surface spot coverage than those with slow rotation rates (Cao & Pinsonneault, 2022). While stellar spots are useful in determining the surface rotation of stars, through periodic brightness variations, they have also been obtrusive in other areas. For example, they can mimic transits of exoplanets in light curves.

In this work, we investigate the effect of stellar spots on the inferred atmospheric parameters of stars through spectroscopy. We adopt a simple two-temperature model of the stellar atmosphere to reflect the impact of stellar spots on the stellar atmosphere. With this model, we generate synthetic spotted spectra of a population of stars with physically motivated stellar and spot parameters. Then, we investigate the effect of fitting spotted spectra with non-spotted models of the stellar atmosphere. We find that even in this simple model, stellar spots can introduce bias and scatter to inferred atmospheric parameters. The introduced scatter is particularly impactful to the precise measurement of stellar metallicity, as it impacts high-precision differential studies, where it is not known whether one or both stars exhibit spots.

The content of this chapter was originally published as:

[Wilson & Casey \(2023\)](#)

and is presented here in the form of a chapter for aesthetic purposes in accordance with Monash University's thesis by submission guidelines.

Abstract

To accurately measure a star’s atmospheric parameters and chemical abundances, it is crucial to have high-quality spectra. Analysing the detailed chemical abundances of groups of stars can help us better understand nucleosynthesis, galactic chemical enrichment, and stellar evolution. In this study, we explored whether stellar spots can affect a star’s inferred metallicity and, if so, where the impact is the strongest. To investigate this, we created synthetic infrared spectra that included stellar spots for a sample of main-sequence stars. We then applied two models to the data: one that accounted for spots and one that did not. From this, we can determine the bias introduced when fitting spotted spectra with a non-spotted model and how this bias varies with different parameters. Our findings revealed that fitting spotted spectra with a non-spotted model can introduce a scatter of up to 0.05 dex in the inferred metallicity, especially for stars with high levels of spot coverage. This bias is similar in magnitude to other relevant effects, such as atomic diffusion, radiative levitation, or non-local thermodynamic equilibrium. We also found that the effect is most pronounced in young stars and decreases with age. These results suggest that stellar spots can introduce a systematic uncertainty in metallicity that is not currently accounted for in spectroscopic analysis. This could potentially limit scientific inferences for population-level studies and differential abundance analyses.

3.1 Introduction

It is widely assumed that the elemental abundances in a star’s atmosphere accurately reflect the abundances of the material from which the star formed (Gibson et al., 2003; Pagel, 2009; Salaris & Cassisi, 2017). This assumption is critical for chemical tagging (Anders et al., 2016; Randich et al., 2022), understanding galactic formation (Gibson et al., 2003), and the synthesis of elements across cosmic time (McWilliam & Rauch, 2004; Johnson et al., 2020). Precise measurements of elemental abundances are essential in many areas of astrophysics. For example, chemical tagging allows us to track the history of the galaxy, which would be impossible with biased measures of abundance. Differential abundance techniques (Reggiani et al., 2016) – employed for solar twins and planet-hosting stars – claim very precise abundance measurements, which are essential for probing planet formation (Tayar et al., 2022). Similarly, when determining cluster ages (Bensby et al., 2004; Pont & Eyer, 2004), the turn-off age of a star is particularly useful for this purpose because a small change in colour/magnitude, which depends on metallicity, indicates a relatively large change in age compared to the main-sequence.

Recognising that surface abundances may change over a star’s evolution is important. The surface abundances can change due to numerous processes. Atomic diffusion and radiative levitation introduce surface abundance variations on the scale of 0.05 dex, with a magnitude and

bias that depends on the element and the stellar effective temperature (Önehag et al., 2014). Enhanced mixing can also cycle material to the surface. Nuclear reactions, such as lithium depletion (Pinsonneault et al., 2002) or CNO cycling (Crowther, 2007)) enhance and deplete specific surface abundances and isotopic ratios. Accretion can enhance surface metallicity and vary particular elemental abundances for a short time depending on the companion type (Pasquini et al., 2007; Maldonado et al., 2019; Laughlin & Adams, 1997). For example, mass loss can strip away H-rich surface regions in Wolf-Rayet stars (Crowther, 2007) - increasing the observed stellar metallicity or carrying away surface metals which will have a small to negligible decrease of surface metals on the main sequence.

These effects are usually ignored when estimating a star's stellar parameters and chemical abundances. Most spectroscopic analyses usually adopt some simplifying assumptions to make the computation time tractable. For example, we usually assume the stellar photosphere can be represented in one dimension (1D) and that baryonic matter can be described by thermal distributions in small regions (local thermal equilibrium; LTE). These assumptions can particularly influence the measured stellar parameters (e.g., Blanco-Cuaresma, 2019). Both can lead to an over-estimate of the temperature gradient in the atmosphere and an underestimation of the density, which can result in an over-estimate of the abundance. We also typically ignore magnetic activity, but recently Spina et al. (2020) showed it has a measurable impact on the chemical abundances of young, fast-rotating stars. While these assumptions simplify inference, it is important to consider their effects when reaching conclusions.

Stars have spots, which are important indicators of the rotational rate of stars, especially along the main sequence (McQuillan et al., 2014; Santos et al., 2021). The properties of stellar spots vary with evolution: age, rotation rate, mass, and metallicity. Spot properties can be generalised by: their coverage across the stellar surface, the temperature difference relative to the surrounding, and the occurrence pattern. Cao & Pinsonneault (2022) recently quantified the spot parameters of stars in the Pleiades and M67. They found that young or fast rotating stars tend to be more magnetically active and have a greater spot coverage than their older, slower counterparts.

The spotted areas of the star can be thousands of degrees cooler than the surrounding areas. A spotted star's stellar spectra are more complex than their non-spotted counterparts (Morris et al., 2019). Accurate inference of stellar parameters requires a model that reflects the stellar spectra well. In this work, we quantify the effect of fitting spotted spectra with non-spotted models and identify the parts of the main sequence where the effect is most prevalent. In Section 3.2, we outline the generative model for stellar spectra with spots and describe our choices of stellar parameters before outlining the fitting procedure used. In Section 3.3, we present the difference in the recovered stellar parameters with the spotted and non-spotted models. We discuss parts of the main sequence where the effect is most prevalent. Finally, in Section 3.4, we place those

results in the context of other significant effects on measured stellar metallicity and provide recommendations for high-precision spectroscopic investigations in specific regions of stellar evolution.

3.2 Method

3.2.1 Stellar parameters for a population of fake stars

We prepare a sample of stellar spectra that spans the main sequence to estimate the impact that stellar spots can have on the accuracy of inferred stellar parameters. This sample is intended to be indicative of a possible population of main-sequence stars but not intended to represent which stars would, or would not, have spots. We generate 1500 spectra of main-sequence and early post-main-sequence stars with various values of mass, age, metallicity, $v\sin i$, f_{spot} , and x_{spot} across the HR diagram. We drew masses from a Salpeter initial mass function (Salpeter, 1955) between 0.5 and $1.5 M_{\odot}$ with $\alpha = 2.35$. This limits our range of masses to those with a radiative surface and convective core and reaches beyond the Kraft break (Kraft, 1967). Metallicity is drawn from a distribution to approximately reflect what is observed in the Milky Way. Specifically, we defined a variable ϕ to be drawn from a Beta distribution

$$\phi \sim \mathcal{B}(\alpha = 10, \beta = 2) \quad (3.1)$$

and applied a transform from ϕ to [Fe/H] by requiring the metallicities be bounded between $[\text{Fe}/\text{H}]_{\min} = -2$ and $[\text{Fe}/\text{H}]_{\max} = +0.5$. We also required that the mode of ϕ , defined as $\frac{\alpha-1}{\alpha+\beta-2}$ for a Beta distribution, occurs at Solar metallicity. This leads to the transform:

$$[\text{Fe}/\text{H}] = \left([\text{Fe}/\text{H}]_{\max} - [\text{Fe}/\text{H}]_{\min} \right) \left(\phi - \frac{\alpha-1}{\alpha+\beta-2} \right) \quad . \quad (3.2)$$

The stars we generate mock data for in this work span from the zero-age main sequence (ZAMS) to low-luminosity subgiants. We draw equivalent evolutionary phase (EEP) values from a uniform distribution $\text{EEP} \sim \mathcal{U}(200, 450)$, where $\mathcal{U}(x,y)$ denotes a uniform prior between x and y . The bounds of this range (200 and 450) represent the ZAMS and the low-luminosity subgiant phase, respectively. Using the EEP, mass and metallicity, we interpolate a position along the MIST stellar isochrones (Morton, 2015) to calculate the expected T_{eff} and $\log g$ for each random star. We also obtain the star's age (post-ZAMS) that we can use in conjunction with the other stellar parameters to determine rotational properties (see below). We have limited the age of the stars we consider in this work up to the age of the Sun. This is the range available for rotational

rate and convective turnover timescales from the sources we draw from in this work. This limits the post-MS stars we consider to more massive stars. We briefly discuss bias' which may introduce in Section 3.4.

The surface rotation period is interpolated from stellar cluster-tuned rotational isochrones given the stellar age and mass (Table A1 in [Spada et al. \(2016\)](#)). Rotational broadening $v \sin i$ can then be calculated by combining the rotational period, the radius from the interpolated isochrone model, and an inclination angle. We have drawn inclination from a uniform distribution in $\cos i \sim \mathcal{U}(0, 1)$.

f_{spot} is related to the Rossby number, R_o , which is defined as the ratio of the surface rotational period to the convective turnover timescale (τ_{conv}). τ_{conv} is interpolated from Table 1 in [Landin et al. \(2010\)](#) given the stellar age and mass. Combining this value with the rotational period, we obtain R_o . f_{spot} is then calculated from the relationship between f_{spot} and R_o identified in [Cao & Pinsonneault \(2022\)](#) (Eq. 5):

$$f_{\text{spot}} = \begin{cases} 0.278, & \log R_o \leq -0.729 \\ 0.0623 R_o^{-0.881}, & \log R_o > -0.729 \end{cases}. \quad (3.3)$$

There is some scatter in f_{spot} which is not accounted for by this relation (see left panel of Figure 7 in [Cao & Pinsonneault \(2022\)](#)). For this reason, we add random noise to our calculated f_{spot} which is drawn from a normal distribution with a standard deviation of 0.1 it is clear that there is some scatter in f_{spot} About

We assume x_{spot} is drawn from a uniform distribution $x_{\text{spot}} \sim \mathcal{U}(0.8, 1.0)$. This represents the limits set when fitting x_{spot} in ([Cao & Pinsonneault, 2022](#)), which is motivated by temperature bounds which they discuss in more detail in Section 2.2. x_{spot} does not appear to have a clear relationship with other stellar parameters, but it - and f_{spot} - may vary on multiple periodic timescales as they do for the Sun. The stochastic nature of stellar observations - and the admittedly simple nature of the model - means that f_{spot} and x_{spot} are random draws from the possible stellar spot parameters. We will eventually find that x_{spot} has little effect on the bias introduced by fitting spotted spectra with a non-spotted model, so move forward with the knowledge that we have good coverage when modelling over the range of possible parameters.

3.2.2 Spotted spectrum generative model

We build upon the work of ([Cao & Pinsonneault, 2022](#)), where a forward model is developed to model the effect of starspots and to estimate the fractional spot coverage of stars in the Pleiades and M67. Their model assumes that the spectrum of a spotted star can be broken into spotted

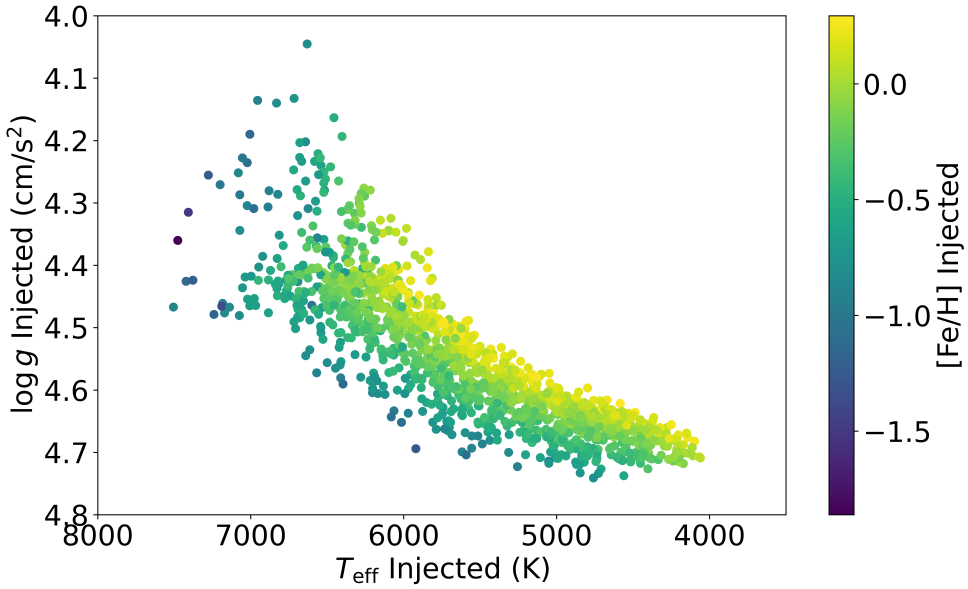


FIGURE 3.1: HR diagram of the 1500 sets of stellar parameters drawn from physically motivated distributions of mass, metallicity and age coloured by [Fe/H].

and non-spotted components. These two components have the same $\log g$, [Fe/H], microturbulent velocity, and the same surface rotational velocity ($v \sin i$), but the two components vary in temperature. The spot and ambient temperatures (T_{spot} and T_{amb}) are related by $T_{\text{spot}} = x_{\text{spot}} T_{\text{amb}}$, and are coupled to the effective temperature of the star following the approach of [Somers & Pinsonneault \(2015\)](#)

$$T_{\text{eff}} = T_{\text{amb}}(1 - f_{\text{spot}} + f_{\text{spot}}x_{\text{spot}}^4)^{\frac{1}{4}}, \quad (3.4)$$

where f_{spot} is the fractional surface spot coverage. From these relations, the set $\{T_{\text{eff}}, x_{\text{spot}}, f_{\text{spot}}\}$ define a pair of ambient and spot temperatures that preserve stellar luminosity.

We calculated a grid of synthetic spectra, which we interpolate between to generate the predicted spectra for a spotted or non-spotted model. The list of atomic and molecular transitions is from ([Shetrone et al., 2015](#); [Smith et al., 2021](#)). We used a grid of plane-parallel MARCS ([Gustafsson et al., 2008](#)) model photospheres that span dimensions in effective temperature, surface gravity, and metallicity.¹ Microturbulence was kept fixed based on surface gravity ([Holtzman et al., 2018](#))

$$\log_{10} v_{\text{micro}} = 0.37 - 0.091 \log g - 0.0008 \log g^2 + 0.0013 \log g^3, \quad (3.5)$$

and we assumed that $[\alpha/\text{H}]$ scales with [Fe/H] (i.e., the so-called ‘standard’ composition in MARCS). The abundance dimensions [C/M] and [N/M] were kept fixed at zero. We used Korg ([Wheeler et al., 2023](#)) to synthesise all model spectra at high resolution, which we then convolved and down-sampled to match the (uniform in log) pixel spacing used in the APOGEE

¹We calculated spectra using spherical models as well, but in practice, only spectra from plane-parallel models (i.e., main-sequence stars) are used in this work.

data reduction pipeline (Holtzman et al., 2018). The convolution kernel includes two components that enter multiplicatively: one assuming a constant spectral resolution $R = \lambda / \Delta\lambda$ of 22,500, and another representing rotational broadening $v \sin i$. We convolved each spectrum with a grid of $v \sin i$ values that were uniformly spaced in $\log v \sin i$ from 0-100 km s⁻¹ in order to match the setup for the APOGEE analysis pipeline. Naturally, for low $v \sin i$ values, the line spread function of the instrument will dominate.

With this grid of spectra and some given spectral parameters $\{T_{\text{eff}}, \log g, [\text{Fe}/\text{H}], \log v \sin i\}$, we interpolate the spotted and ambient spectra and combine them in a fractional manner with wavelength as if they were separate black-body spectra in order to produce a flux-preserving combined spectrum:

$$B(T_{\text{eff}}, \lambda) = f_{\text{spot}} B(T_{\text{spot}}, \lambda) + (1 - f_{\text{spot}}) B(T_{\text{amb}}, \lambda) . \quad (3.6)$$

In total, our forward model for predicting spotted spectra includes six parameters: T_{eff} , $\log g$, $[\text{Fe}/\text{H}]$, $\log v \sin i$, x_{spot} , and f_{spot} . This model is equally capable of predicting non-spotted spectra by fixing f_{spot} to zero or x_{spot} to unity.

Using the 1500 sets of parameters outlined in Section 3.2.1 we generated synthetic spotted stellar spectra. We also apply realistic noise at each pixel from a Gaussian distribution with standard deviation = 0.01, assuming a signal-to-noise ratio of 100. Continuum normalisation is performed by assuming a running mean of the spectra, and during fitting, this procedure is applied to the fake spectrum (data) and to the model spectrum.

We now have the tools to determine the effect of fitting spotted spectra with non-spotted models. We do this by finding the best-fitting stellar parameters given the synthetic spectra fitted twice: first with the model described in Section 3.2.2 and then with a non-spotted model (e.g., f_{spot} fixed at 0 and x_{spot} fixed at 1). Here we have performed least-squares fitting through the Levenberg-Marquardt algorithm implemented in SCIPY. We found that fitting the spotted parameters can be non-trivial. The likelihood surfaces are multimodal and degenerate, requiring informed choices about the initialisation of fitting. To resolve this issue, we performed a coarse evaluation of parameters (on a grid) before starting optimisation.

3.3 Results

We began by confirming that we could accurately recover the injected parameters. The best-fit parameters following fitting the synthetic spotted spectra with a spotted model are shown in Figures 3.2 and 3.3. T_{eff} , $\log g$, $[\text{Fe}/\text{H}]$, and $v \sin i$ are recovered accurately for every injected

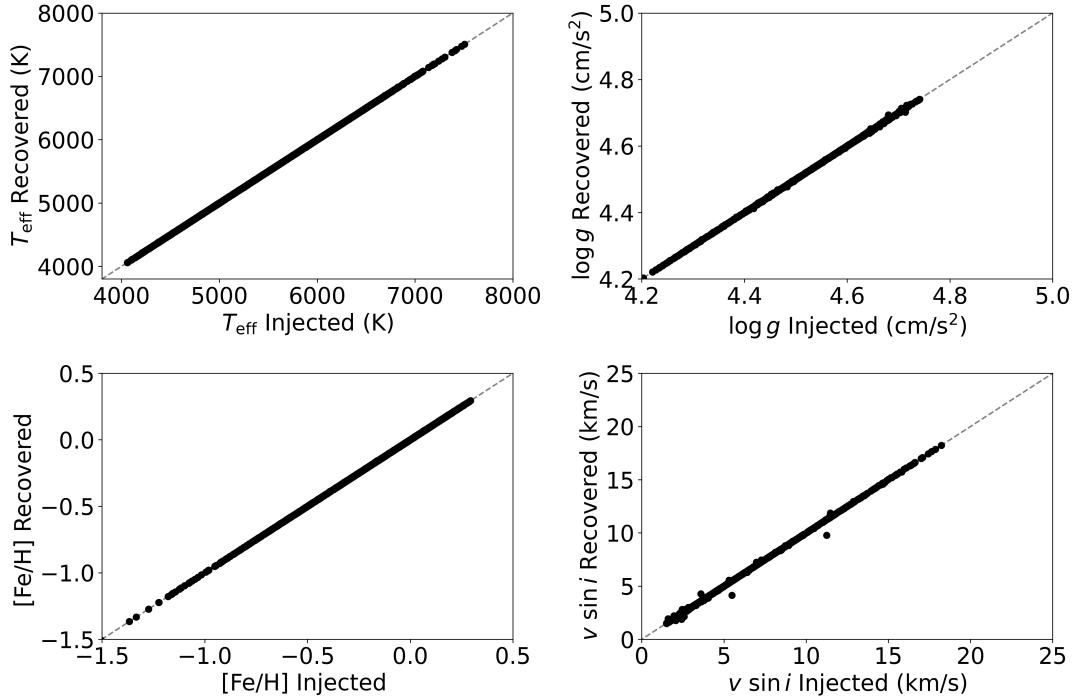


FIGURE 3.2: Recovered traditional stellar parameters (T_{eff} , $\log g$, $[\text{Fe}/\text{H}]$ and $v \sin i$) from fitting synthetic spotted spectra with a spotted model of the stellar atmosphere against the corresponding injected parameters. We consistently accurately recover each injected value when a spotted model of the stellar atmosphere is employed to fit the spotted synthetic spectra.

parameter set. While we identify scatter in recovered f_{spot} this appears not to affect the accuracy of the recovery of the traditional stellar parameters. We move forward confident that any difference in the recovered parameters between fitting with the spotted and non-spotted models results from the model differences rather than the fitting procedure employed in this work.

We now identify systematic effects in the recovered parameters when we fit the spotted spectra with an incorrect model of non-spotted spectra. The difference between the recovered parameters fitted with a spotted and non-spotted model of the stellar atmosphere are shown in Figure 3.4. A consistent scatter is introduced on each parameter when a non-spotted model is used to perform inference on a spotted spectrum. We calculate each parameter's average bias and scatter to quantify the effect. The injected parameters are separated into 10 bins, and we take the median and median absolute deviation of the difference between the spotted and non-spotted model's inferred parameters for each bin. We take the median as a measure of the average bias and the median absolute deviation as a proxy for the scatter.

In Figure 3.5 we show the effect of the injected parameters on the stellar spot spectra through the difference between the recovered spot and non-spot model T_{eff} . Fitting a spotted spectrum with a small x_{spot} with a non-spotted spectrum introduces a consistent bias to the inferred T_{eff} of about -25 K: a non-spotted model tends to underestimate the true effective temperature of a spotted spectrum. A scatter is also introduced T_{eff} on the scale of ~ 50 K for spectra with significant spot

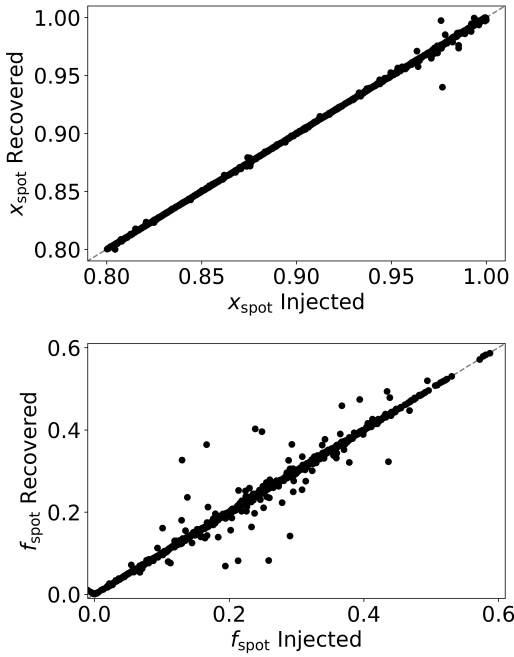


FIGURE 3.3: Recovered spot parameters (x_{spot} and f_{spot}) from the synthetic spotted spectra fitted with a spotted model of the stellar spectra against the injected parameters of the synthetic spectra. We identify that the spot parameters are not always accurately recovered through the fitting procedure. The recovered spot parameters are notably more inaccurate as x_{spot} approaches 1.

coverage (low x_{spot} and large f_{spot}). The other injected parameters do not appear to have any strong correlations or effects on the recovered non-spot T_{eff} . Their median values are zero, and MAD appears consistent at $\sim 25\text{K}$.

Figure 3.6 shows the effects of fitting spotted spectra with a non-spotted model on $\log g$ (orange) and $\log v \sin i$ (red), respectively. There appears to be no statistically significant bias introduced to both of the inferred parameters as the median of each bin of injected parameters is consistently about zero. However, a consistent scatter is introduced to both parameters. The MAD of $\Delta \log g$ and $\Delta \log v \sin i$ in each injected parameter bin have an average value of ~ 0.025 dex - corresponding to an average scatter on $v \sin i$ of $\sim 1 \text{ km s}^{-1}$. The scatter peaks for both recovered parameters at ~ 0.05 dex for stars with significant spot coverage - which corresponds to a maximum scatter on $v \sin i$ of $\sim 2 \text{ km/s}$. The scatter on recovered $v \sin i$ and $\log g$ is otherwise constant with the other injected parameters.

The effect of fitting spotted spectra with a non-spotted model is significant in the recovery of metallicity. This is seen in Figure 3.6 (green), where we compare the recovered [Fe/H] with a spotted and non-spotted model of the stellar atmosphere against the injected parameters of our spotted spectra. This process does not introduce a bias to the inferred metallicity of the spectra but does introduce a significant scatter to the recovered value, representing an intrinsic ‘minimum floor’ of systematic uncertainty if the effects of spots are not included (see Section 3.4).

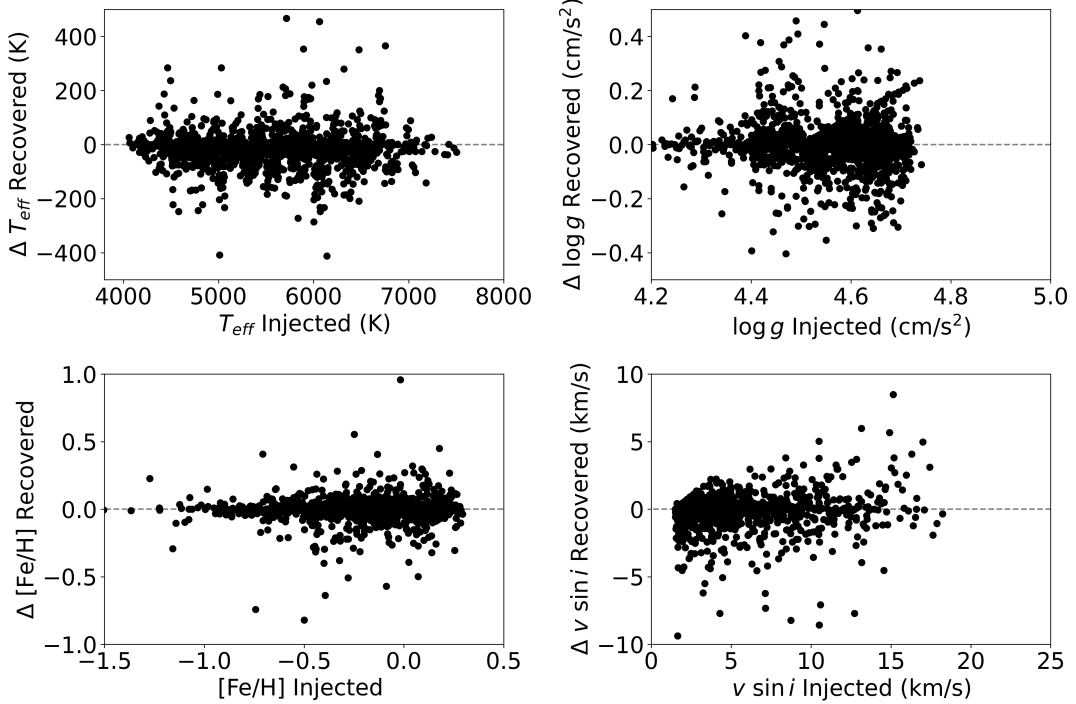


FIGURE 3.4: The difference between the recovered traditional stellar spectra parameters (T_{eff} , $\log g$, $[\text{Fe/H}]$ and $v \sin i$) from the synthetic spotted spectra fitted with both a spotted and non-spotted model of the stellar spectra against the injected parameters of the synthetic spectra (spotted model non-spotted model recovered parameter). We identify scatter introduced to each of the stellar parameters when fitting spotted spectra with a non-spotted model of the stellar atmosphere.

The scatter introduced to $[\text{Fe/H}]$ by fitting spotted spectra with a non-spotted model increases with injected f_{spot} . As f_{spot} approaches 1, the MAD of $\Delta[\text{Fe/H}]$ reaches a maximum of about 0.05 dex. Comparatively, as x_{spot} decreases, so does the MAD of $\Delta[\text{Fe/H}]$, peaking again at 0.04 dex. As the scatter in the other injected parameters is relatively constant, there is no significant relation between the other spectral parameters and $\Delta[\text{Fe/H}]$. The introduced scatter in $[\text{Fe/H}]$ is dominated by the spot parameters of spectra.

3.4 Discussion

The results in Section 3.3 indicate that using a non-spotted model to fit spotted stellar spectra introduces a systematic bias of up to -25 K in effective temperature and no substantial bias in other parameters. In their study of fitting a spotted stellar model to APOGEE spectra of members in the Pleiades and M67, [Cao & Pinsonneault \(2022\)](#) find a systematic 0.1 dex enhancement in observed $[\text{Fe/H}]$. The lack of bias we find here could be attributed to different stellar populations of stars (e.g., some stars are biased in one direction, but in our population, that effect is mitigated by biases in the opposite direction). We find that the effects of model mismatch (i.e., using a

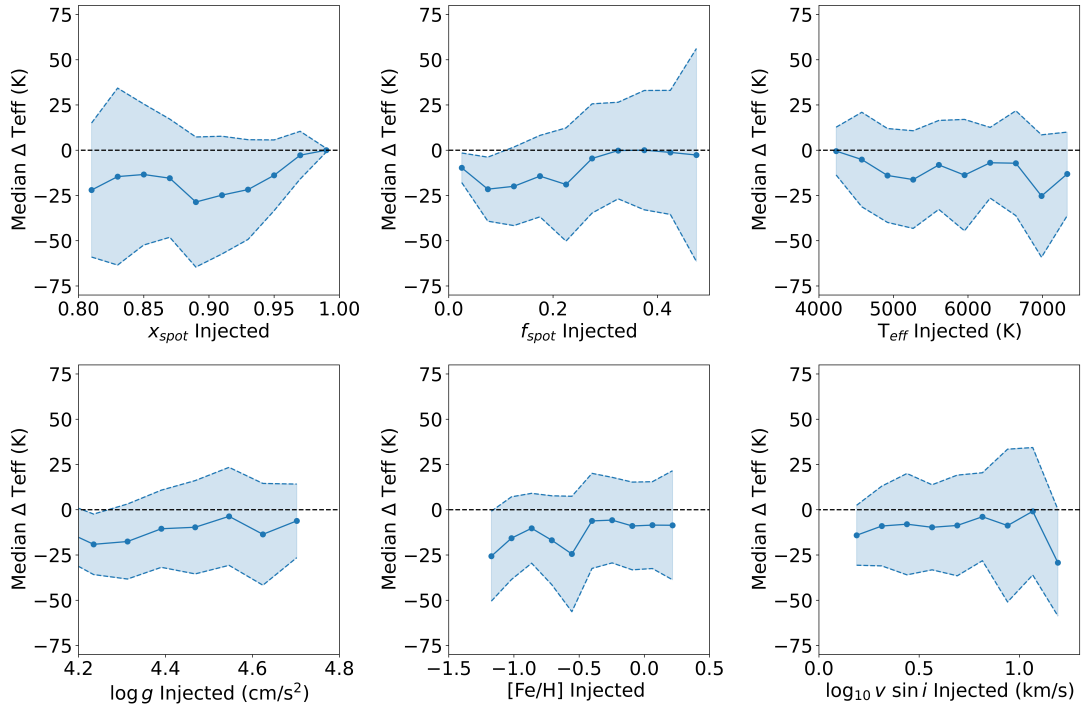


FIGURE 3.5: Bias introduced to T_{eff} (blue) when fitting spotted spectra with a non-spotted model against injected parameters of synthetic spectra. Each injected parameter is binned into ten bins across the range of injected parameters. The median and median absolute deviation of the difference between the spotted and non-spotted recovered T_{eff} (ΔT_{eff}) are then calculated in each bin. Scatter points show the median ΔT_{eff} for each bin in injected parameters. Filled areas show one maximum absolute deviation above and below the median value and dashed lines indicate the edge of this range. Inference of T_{eff} with a non-spotted model injects random scatter on average of the scale of $\sim 50\text{K}$ and introduces a consistent bias of order $\sim 25\text{K}$ for spectra with significant spot coverage.

non-spotted model to fit a spotted spectrum) can also introduce a scatter (measured by median absolute deviation) of about 50 K in effective temperature and 0.05 dex in other parameters. If we assume that the spot model we adopt is representative of reality, then these scatter values would represent a minimum systematic uncertainty in these parameters if the wrong model (a non-spotted model) is used. These deviations are comparable to the typical random uncertainties reported by the APOGEE survey (150K, 0.13 dex and 0.1 dex; [Heged  s et al., 2023](#)), although these random uncertainties will vary with signal-to-noise.

Systematic uncertainties (like model mismatches) will dominate in high signal-to-noise ratios, and the level of scatter we find in metallicity (0.05 dex) is comparable to the effects of radiative levitation, atomic diffusion ([  nehab et al., 2014](#)), and magnetic broadening of absorption lines ([Spina et al., 2020](#)). Unlike these effects, which can in part be mitigated through parameterisation with other stellar parameters, accounting for stellar spots requires a model that explicitly predicts their contribution to the emergent spectrum. This scatter in $[\text{Fe}/\text{H}]$ is significant as it is of the same order as the precision of spectroscopic inference of metallicity. In particular, a differential analysis of two Solar twins might report abundance uncertainties on the level of

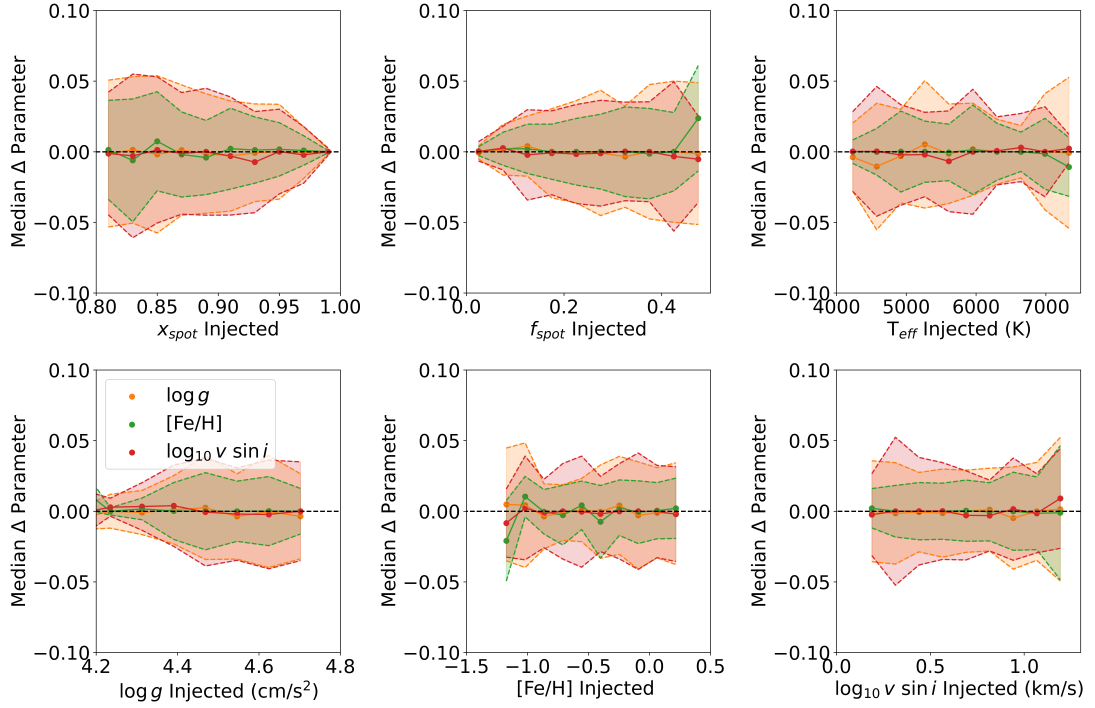


FIGURE 3.6: Bias introduced to $\log g$ (orange), $[\text{Fe}/\text{H}]$ (green) and $\log \nu \sin i$ (red) when fitting spotted spectra with a non-spotted model against injected parameters of synthetic spectra. Here we have plotted $\log \nu \sin i$ as the grid we perform interpolation over is distributed uniformly in $\log \nu \sin i$ and to make direct comparisons to the other stellar parameters ($[\text{Fe}/\text{H}]$ and $\log g$). Each injected parameter is binned into ten bins across the range of injected parameters. The median and median absolute deviation of the difference between the spotted and non-spotted recovered parameters (Δ parameter) are then calculated in each of these bins. Scatter points show each bin's median Δ parameter in injected parameters. Filled areas show one maximum absolute deviation above and below the median value and dashed lines indicate the edge of this range. Fitting spotted spectra with non-spotted models does not introduce a bias to the inferred parameters though it does introduce a scatter. This scatter increases with decreasing x_{spot} and increasing f_{spot} to a maximum median absolute deviation on the order of ~ 0.05 for $\log g$, $[\text{Fe}/\text{H}]$ and $\log \nu \sin i$ - which corresponds to a maximum scatter on $\nu \sin i$ of ~ 2 km/s. The scatter is otherwise approximately constant for all other parameters, and on average ~ 0.025 - which corresponds to an average scatter on $\nu \sin i$ of ~ 1 km/s

0.01-0.02 dex. While the two stars are selected to be extremely similar in order to mitigate systematic effects, those two stars could have very different coverages of stellar spots, which would introduce a systematic uncertainty floor.

3.4.1 Imperfect models

The results we show here are limited in their applicability. When generating the mock data, only a fraction of randomly drawn stellar parameters could be used to synthesise spectra, either because of limitations of stellar isochrones, the spectral grid, or limits in the procedure in estimating an appropriate rotational velocity and Rossby number. We also limit the ages of the

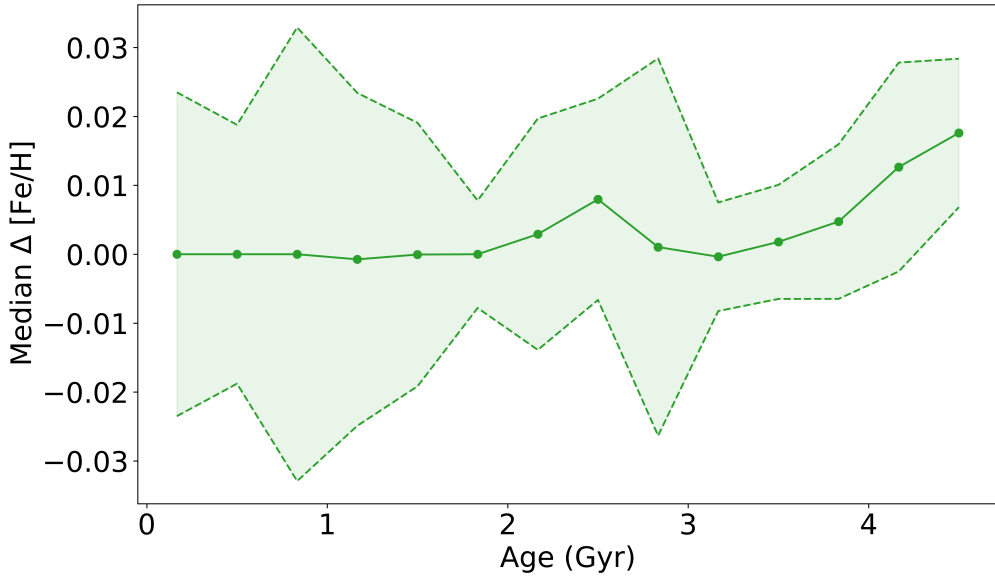


FIGURE 3.7: Bias introduced to [Fe/H] when fitting spotted spectra with a non-spotted model against the age of the model used to generate synthetic spectra. Age is binned into ten bins across the range of injected parameters. The median and median absolute deviation of the difference between the spotted and non-spotted recovered [Fe/H] (Δ [Fe/H]) are then calculated in each of these bins. Scatter points show the median Δ [Fe/H] for each bin in injected parameters. Filled areas show one maximum absolute deviation above and below the median value and dashed lines indicate the edge of this range. We find that the introduced scatter is greatest for stars younger than ~ 2 Gyr is ~ 0.02 while the bias is 0 for stars in this age range. The scatter decreases for older stars (>3 Gyr) to ~ 0.01 but the median Δ [Fe/H] increases with increasing age. This is like the result of the small number of stars in our sample in this age range rather than indicative of a trend.

stellar sample to 4.6 Gyr - the maximum ages of both the models used to determine the convective turnover timescale and grid of rotational periods set by observations. As a result, our sample is limited to relatively young stars, and there are hints of a bias in injected parameters towards higher f_{spot} . We have extensively probed the region where the effect should be most prevalent in terms of the scatter it introduces, but this is not intended to be a complete and representative population of main-sequence stars. The quantitative results may not be perfectly accurate for some regions of the HR diagram. However, by assuming spots are present everywhere across the main sequence, our analysis shows where the consequential effects are most or least prevalent.

The treatment of stellar spots in this work requires some discussion. Stellar spots are highly complex regions on the surface of stars.

The position of spots relative to the observer, their temporal evolution, and the inherent magnetic activity and faculae surrounding stellar spots, would all introduce complexity to the emergent spectra from these regions. The spotted model employed in this work is a first-order approximation of the average effect of spots on stellar spectra. The functional form of the temporal evolution of the stellar spots in stars other than the Sun is not well known. For a given f_{spot}

we could assume that x_{spot} varies on some periodic or temporal scale, even if we don't know the functional form of that variability. In this scenario with our model, x_{spot} is drawn from a uniform prior, which implicitly assumes that we are observing the star at some random time. This modelling of x_{spot} is relatively crude since, in principle, x_{spot} could vary as a function of other stellar parameters.

Investigations of the evolution of fractional spot coverage of stars is a developing field. For example, recent works have shown an enhancement in f_{spot} for stars undergoing core-envelope recoupling ([Cao et al., 2023](#)). For this reason, our results are only indicative rather than prescriptive. Applying this model to more stars APOGEE samples and time series spectroscopic observations of stars could elucidate the relationship between the parameters.

[Cao & Pinsonneault \(2022\)](#) suggest that young, magnetically active stars - stars with Rossby numbers < 0.4 - have f_{spot} greater than > 0.1 , saturating at $f_{\text{spot}} \sim 0.3$, with significant scatter, when $R_o < 0.2$. There is also a significant scatter in f_{spot} for these stars. The use of the Rossby number to reflect the magnetic/spot activity of stars should be treated with some care. The Sun expresses periodic evolution of its magnetic activity (time scale on the order of decades) and stellar spot expression (time scale on the order of years). The range of fractional spot coverages we observe in the Sun is on the order of [0, 0.12] without variations in the Rossby number. As a result, we draw the injected f_{spot} from relations with Rossby number and add a random scatter drawn from a Gaussian distribution with a standard deviation of 0.1.

Employing a non-spotted spectra model to fit spotted spectra can introduce a scatter to recovered parameters, but fitting a spotted model to non-spotted spectra has little to no effect on the recovered parameters. We recommend that a spotted model, if only as simple as the one used in this work, will consistently recover stellar parameters better than a non-spotted model while also providing a measure of the spot parameters of stars.

3.4.2 When should a spotted model of the stellar atmosphere be employed?

The scatter introduced to the recovered stellar parameters increases with fractional spot coverage. Fractional spot coverage is inversely related to the rotation rate of stars through R_o . Further, the rotation rate of stars decreases with time, owing to magnetic braking. As a result, the fractional spot coverage of stars is expected to decrease with age.

We can probe when the scatter introduced to the recovery of stellar parameters by stellar spots is most prominent by calculating the scatter in $\Delta[\text{Fe}/\text{H}]$ with bins of age. In Figure 3.7, we show the bias and scatter introduced to $\Delta[\text{Fe}/\text{H}]$ with respect to stellar age. The introduced scatter is greatest for stars younger than $\sim 2\text{Gyr}$ is ~ 0.02 , while the bias, measured through the median, is zero for stars in this age range. The scatter decreases for older stars ($> 3\text{Gyr}$) to ~ 0.01 , but

the median $\Delta[\text{Fe}/\text{H}]$ appears to increase with increasing age. The increase in the median value is most likely not indicative of a trend and rather the result of the low number of stars in the larger age bins.

The trends that we identify in this work are only qualitative - though they do allow us to make recommendations for future work. Our results indicate that fitting the spotted spectra of a star with a non-spotted model when $f_{\text{spot}} > 0.1$ will introduce a scatter to bias the recovered parameters. We suggest using a spotted model if a star is significantly photometrically variable due to stellar spots. [McQuillan et al. \(2014\)](#) calculated the rotation periods of low-mass main-sequence stars that are photometrically variable due to stellar spots. They were able to determine the rotation rates of stars across a wide mass range ($0.6 < M_{\odot} < 1.1$) at multiple points along the main sequence. These stars must therefore express stellar spots and may have the measured stellar parameters influenced by the effect we identify in this work. They estimated that $\sim 23\%$ of main-sequence stars exhibit definite rotational modulation from stellar spots, a lower bound due to observational effects. We, therefore, believe at least 1/4 of the main sequence stars may be affected by this bias.

3.5 Conclusions

Here we have shown that stellar spots can introduce measurable systematic bias and variance to inferred stellar parameters when a non-spotted model is used. The results demonstrate that spectra with strong spot features can introduce a scatter in inferred metallicity of order 0.05 dex. This emphasises the need for caution when performing spectroscopic analysis on stars with visible spots, particularly young, fast-rotating stars. Our findings highlight the importance of incorporating the effect of spots into spectroscopic models to ensure accurate and precise results.

The magnitude of this effect is comparable to others that plague stellar spectroscopy, including atomic diffusion, radiative levitation, and non-local thermodynamic equilibrium. However, the impact of this effect will vary depending on the scientific context. Turn-off ages of clusters are likely to be only minimally impacted, as the metallicity bias for old, slowly rotating stars is less than 0.01 dex. In contrast, a systematic error floor of 0.05 dex caused by spots on the main sequence would critically limit the capacity of strong chemical tagging ([Casamiquela et al., 2021](#)). Similarly, star spots could limit any inferences from differential abundance analyses of Sun-like stars, where the typical reported uncertainty is 0.01-0.02 dex (e.g., [Nissen, 2015](#)). While we have focused on the impact on overall metallicity and not on individual abundances, it will be important to examine these effects more closely at a per-element level. These results provide valuable insights for future studies on stars and their properties and underscore the need for continued research on the impact of spots on spectroscopic inference.

Chapter 4

The effect of Rossby number dependent latitudinal differential rotation on the observed rotation period distribution

Portions of this Chapter will form an upcoming publication.

Abstract

Photometric variability due to stellar spots allows astronomers to measure the surface rotation periods of stars. Within multiple missions’ rotation period samples (e.g. *Kepler*, *K2*, *ZTF*), there is a distinct dearth of observations of stars rotating at intermediate periods $15 \gtrsim P_{rot} \gtrsim 20$ days, known as the intermediate period gap. The position of this gap varies with the colour of the stars. Various mechanisms have been proposed from stars physically “jumping” the gap through enhanced wind-braking, to stars above and below the gap representing two populations of stars, to the gap representing a minimum probability of observing rotation periods. The exact cause of the gap is unknown. In this Chapter, we propose that the gap represents a sudden increase in the observed rotation period of stars through the onset of equator-fast latitudinal differential rotation. The rotation period gap can be reproduced by this mechanism with simple relations between equatorial and differential rotation evolution.

4.1 Introduction

Measurement of the rotation period of samples of stars allows us to understand internal mechanisms that we otherwise would not be able to probe. The intermediate period gap represents a minimum of observations of stars with particular rotation periods measured from photometric variability due to stellar spots first observed by [McQuillan et al. \(2014\)](#). The intermediate period gap is robust between different photometric observation missions ([McQuillan et al., 2014](#); [Davenport, 2017](#); [Davenport & Covey, 2018](#); [Lu et al., 2022](#)) and multiple period detection methods applied to these missions.

The rotation period here is inferred from periodic variations in the brightness of stars from active regions coming in and out of the observer’s line of sight from the rotation of its surface. It is unknown whether the intermediate period gap occurs in other techniques used to measure the rotation of stars; if it does, it would allow us to focus on particular explanations for the gap. Rotational splittings of low-mass stars where the gap is most apparent, have not been measured, and it is unknown whether the intermediate period gap is also a feature observed in spectroscopic observations of surface rotation velocity. While spectroscopic surface velocity has been measured for orders of magnitude more stars than surface rotation periods from stellar spots, the effect of unknown inclination angles and an uncertain stellar radius would smear out decreased densities of observations. Direct observation of the intermediate period gap from spectroscopic surface velocity has not been made.

The position of the gap varies in period with respect to mass. The quality cuts made to data sets in which rotation period is measured (e.g., removing binaries and subgiants as in the analysis of [McQuillan et al., 2014](#); [Claytor et al., 2023](#)) are not biased away from detecting stars within the gap. These factors suggest that the intermediate period gap represents a function of stellar evolution or an unaccounted-for problem in observing rotation periods through photometric oscillations from stellar spots.

The intermediate period gap is characterised by a number of features as shown in Figure 4.1. The density of stars above and below the gap is roughly constant; the density of observations drops swiftly in the gap. The gap also aligns with a line of constant Rossby number, suggesting a common phase of evolution rather than age. This is interesting because photometric variability drops toward the gap from below and above, suggesting a common phase of magnetic evolution. We also observe that the dearth is most apparent for lower mass ($T_{\text{eff}} < 4500$ K) stars. While not shown in this plot, they are nonetheless indicative of the nature of the gap: the intermediate period gap disappears for fully convective stars ([Lu et al., 2022](#)). Stars above and below the gap are otherwise not distinct in any observable other than rotation period. Further, [Lu et al. \(2022\)](#) argued that stars above and below the gap are of similar kinematic age. An explanation for the gap must explain all of these features.

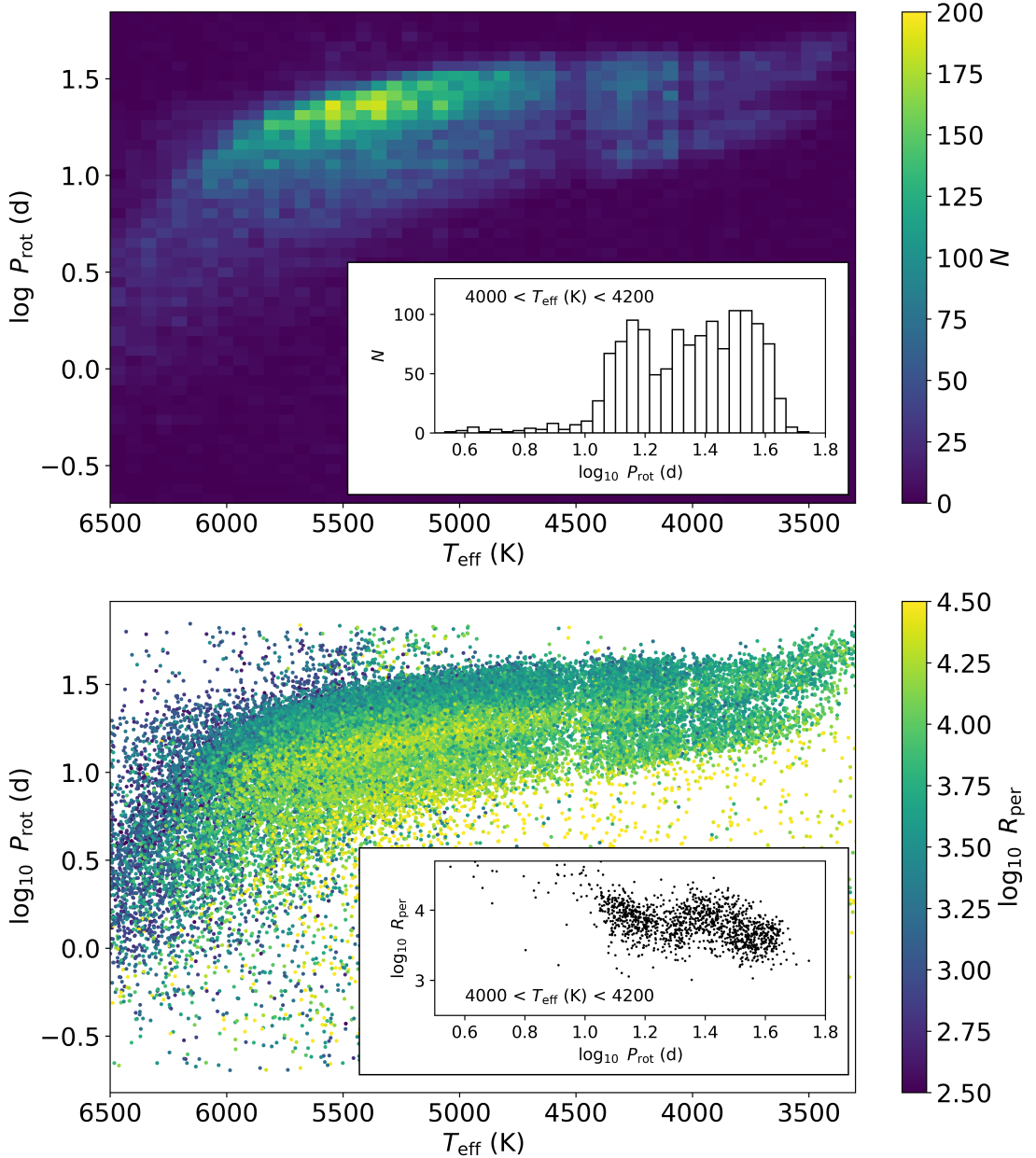


FIGURE 4.1: The rotation period distribution of the (McQuillan et al., 2014) sample highlighting the features of the intermediate period gap. **Top:** A 2D histogram of the logarithm of the rotation period against the effective temperature of the rotation period sample coloured by the number of stars in each bin (N). Here, we observe the dearth of observations of rotation period for stars with $T_{\text{eff}} < 5000$ (K) between $\log_{10} P_{\text{rot}} / d = 1$ and 1.5 , increasing in P_{rot} as T_{eff} decreases: the intermediate period gap. **Bottom:** The logarithm of the rotation period against the effective temperature of the rotation period sample coloured by the logarithm of R_{per} . The alignment of the minimum in R_{per} and the position of the intermediate period gap is also highlighted here. **Top inset:** a histogram of the logarithm of the rotation period for stars with $4000 < T_{\text{eff}} (\text{K}) < 4200$. Here, we observe the dearth of observations of stars in this effective temperature range occurs at $\sim \log_{10} P_{\text{rot}} / d = 1.2$. **Bottom inset:** The logarithm of the rotation period against the logarithm of R_{per} for stars with $4000 < T_{\text{eff}} (\text{K}) < 4200$. Comparing the two inset plots, it is clear that the intermediate period gap and the decrease in R_{per} align with the same position in regards to the period and effective temperature.

Multiple mechanisms have been proposed to explain the intermediate period gap. [McQuillan et al. \(2014\)](#) first proposed that the gap represents bimodal bursty star formation in the local *Kepler* field. They suggest that the lower rotation period (faster rotators) prong represents a younger population, and the upper rotation period prong represents an older population, with the gap representing a minimum in star formation at a particular time. [Davenport & Covey \(2018\)](#) support local bursty star formation hypothesis by separating the *Kepler* rotation period distribution by distance through *Gaia* parallaxes. They find that the gap appears to disappear for stars further away than 525 pc. At those distances, observations of stars are magnitude-limited to brighter high-mass stars ($M \geq 0.9 M_{\odot}$), where observations of the gap are tentative and period detection is much less precise. If the gap extends up to these high-mass stars, then its existence can be blurred out by the imprecision of these measurements. Their work may also support this explanation. In the full [McQuillan et al. \(2014\)](#) sample the gap disappears for high mass ($M \geq 0.8 M_{\odot}$, $B_P - R_P \leq 1.0$) stars. In the distance limited (≤ 525 pc) sample, the gap appears to permeate to these higher-mass stars. This can be seen in the rotation period-effective temperature distribution (known as the rotation period distribution) in the top two panels in Figure 2 of [Davenport & Covey \(2018\)](#) where distance is limited to 525pc.

More recent works significantly disfavour the bursty star formation hypothesis. [Gordon et al. \(2021\)](#) detected the gap in multiple pointings of the *K2* mission. [Curtis et al. \(2020\)](#) found that the open cluster Ruprecht 147 contains stars above and below the gap and a possible star detection within the intermediate period gap. This suggests that the gap is not a coeval feature but instead a feature of the rotational evolution of low-mass stars. [Curtis et al. \(2020\)](#) instead proposed that the gap aligns with a line of constant Rossby number (R_o) equal to ~ 0.5 . R_o is a rotation period and convective turn-over timescale scaled quantity and is associated with the magnetic activity of stars ([Brun, 2003](#); [Fang et al., 2018](#); [Cao & Pinsonneault, 2022](#)).

There are two leading explanations for the gap: the intermediate rotation period gap represents a sudden onset of extreme rotational braking, or the gap results from a low probability of observing stars within the gap. [McQuillan et al. \(2014\)](#) suggested another explanation for the intermediate period gap through a rapid spin-down - “jumping” across the gap quickly, resulting in decreased stars’ density in this region of period and effective temperature. For example, the rapid spin-down could be caused by core and convective envelope rotational decoupling at the upper edge of the lower prong near the rotation period gap. In this mechanism, the core and envelope evolve independently; the rotation rate of the envelope would drop swiftly compared to a core-envelope coupled star, where angular momentum transport from the core to the surface counteracts the loss of angular momentum from magnetic braking. Following the gap, the core and envelope recouple, exchanging angular momentum and returning to a normal rate of magnetic braking. [Gordon et al. \(2021\)](#) argued in favour of this hypothesis based on the rotation period distribution of *K2* data. [Curtis et al. \(2020\)](#) argued that two-zone angular momentum transport models, such as those by [Spada & Lanzafame \(2020\)](#) can reproduce a stalled braking behaviour required to

explain the lower prong of the intermediate rotation period gap. However, their model could not explain the rapid spin-down. This hypothesis is supported by the tentative observation of low-mass fully convective stars permeating the gap and the observed similar ages of stars above and below the gap ([Lu et al., 2022](#)).

[Chahal et al. \(2022\)](#) proposed that the gap results from the low magnetic activity of stars within the gap, resulting in very few expressed stellar spots and, thus, a low probability of observing stars in the gap. [Reinhold et al. \(2019\)](#) and [Reinhold & Hekker \(2020\)](#), however, proposed that the gap is caused by a transition in activity from spot dominance to bright faculae dominance¹. They suggest that as a star spins down and the magnetic field topology changes, the initially strong and long-lived spots are replaced by smaller, short-lived spots surrounded by bright faculae. In such a scenario, the photometric variability amplitude decreases because of the partial cancellation by the increase and decrease in brightness from the faculae and spots. Hence, the stars with small photometric variability will not be detected. These mechanisms are supported by the gap aligning with a line of constant Rossby number and by the photometric variability reaching a local minimum surrounding the gap.

If either of these theories proves correct, they significantly affect our understanding of the evolutionary processes governing stellar rotation and magnetic activity. However, it is important to note that there is currently limited empirical evidence to support the involvement of either theory in explaining the phenomena observed in the intermediate period gap of stars. We propose a previously unexplored mechanism to explain the intermediate period gap: the initiation of latitudinal differential rotation within stars.

Observational data, particularly for the Sun, demonstrates the existence of latitudinal differential rotation in stars. Stars exhibit spots distributed across their surfaces, raising an intriguing question: How should we define the “surface rotation period” of a star? Traditional, radially symmetric (1D) models of stellar evolution offer a means to calculate an “average” surface rotation period for stars. However, if the rotation profile varies across latitudes, the relation between the average rotation period and the latitudinal rotation profile becomes less clear. The measured rotation period of stars, as determined from the presence of stellar spots, generally represents the average rotation period where these spots are visible ([Santos et al., 2021](#)). [Aigrain et al. \(2015\)](#) qualified this idea. They performed a hare-and-hounds exercise with simulated light curves of rotating stars with latitudinal differential rotation and variable latitudinal distribution of stellar spots. Their simulations include a prescription for the latitudinal range of the spot distribution, as well as lifetime and the effect on the brightness of each stellar spot. While a range of rotation periods can be measured owing to latitudinal differential rotation and latitudinal distribution of stellar spots, they find that the “measured” (the period measured from the light curve analysis)

¹This work differentiates between the rotation brightness modulation and brightness modulation from the stellar activity cycle. Stellar activity modulation refers to the long-term evolution of average brightness due to stellar spots and faculae rather than variations on the rotational time scale.

rotation period tends to be dominated by the largest spots. Each spot was assigned a weight proportional to its effective area for direct comparison between the injected and measured range of rotation periods. The “observed” period was then defined as the median weighted period from the latitude of each spot. They found, in general, that the observed and measured rotation periods generally agree. Suggesting that the measured rotation periods of stars vary with latitudinal differential rotation and that if the scale of latitudinal differential rotation grows swiftly, then the measured rotation period will also grow swiftly. It is also worth noting that they found that the measurement of the scale of differential rotation is untenable with current data and methods (see Chapter 1).

For the sake of clarity, in this work, we will refer to the equatorial rotation period as the equatorial rotation period, the observed rotation period as the average rotation period of a star with latitudinal differential rotation scaled by a distribution of stellar spots, and the measured rotation period as the rotation period that is measured from analysis of periodic variation in light curves.

Observations (see, e.g., [Saar, 2011](#); [Benomar et al., 2015](#); [Benomar et al., 2018](#); [Bazot et al., 2019](#); [Hall et al., 2021](#)) and models of stars including latitudinal differential rotation (see, e.g., [Brun et al., 2022](#)) suggest three regimes of latitudinal differential rotation dependent on Rossby number. Their results suggest fast-rotating stars ($R_o < 0.45$) support quenched, latitudinally-flat² rotation profiles. In this regime, the scale of equator-fast differential rotation (which is defined in their work, and this work, as the absolute difference between the rotation rate at the equator and at a latitude of 60° divided by the equatorial rotation rate) increases with R_o . The scale of differential rotation swiftly grows in this regime until it saturates, resulting in intermediate rotating stars ($0.45 \leq R_o \leq 2$) expressing constant scale equator-fast differential rotation. As a star approaches $R_o \sim 2$, meridional transport of angular momentum from the equator to the pole is expected to slow the rotation rate near the equator ([Amard et al., 2016](#)). In combination with angular momentum loss through magnetised stellar winds, this transition is expected to result in a supposed transition from equator-fast to equator-slow latitudinal differential rotation³. The relationship between the scale of differential rotation in this regime is unknown due to a lack of observations of equator-slow differential rotation.

Interestingly, the transition from latitudinally-flat rotation profiles to equator-fast rotation profiles occurs near $R_o \sim 0.5$, the Rossby number where the rotation period gap occurs. If latitudinal differential rotation becomes significant at this point in the evolution of rotation of a star, then the rotation period gap may reflect a sudden increase in the measured surface rotation period from that onset. In this work, we investigate this as a possible mechanism underlying the intermediate period gap by creating a physically motivated observed rotation period distribution under the differential rotation relationships proposed by [Saar \(2011\)](#) and [Brun et al. \(2022\)](#). In

²Or rather, close to latitudinally-flat.

³While this transition is theoretically expected, however, equator slow differential rotation has not been observationally verified.

Section 4.2, we describe the adopted relationships between latitudinal differential rotation and Rossby number, our choices of stellar parameters, and our adopted method to calculate the observed rotation period. We show that the swift onset of equator-fast differential rotation can produce a dearth of observed rotation periods in the rotation period distribution. In Section 4.3, we present the observed rotation period distributions of the synthetic sample, compared to the measured *Kepler* rotation period distribution. Finally, in Sections 4.4 and 4.5, we place those results into context by discussing the implications of our discovery, discuss the impact of the uncertain model parameters, and propose extensions to this work.

4.2 Methods

4.2.1 Generative model

The scale and sign of differential rotation varies with R_o . To calculate R_o we require the first evaluate the convective turnover timescale (τ_c^{CS}) of main-sequence and early post-main-sequence stars using the scaling relation derived in [Cranmer & Saar \(2011\)](#),

$$\tau_c^{\text{CS}} = 314.24 \exp \left[-\frac{T_{\text{eff}}}{1952.5\text{K}} - \left(\frac{T_{\text{eff}}}{6250\text{K}} \right)^{18} \right] + 0.002d, \quad (4.1)$$

from this we calculate R_o ($R_o = P_{\text{surf}}/\tau_c^{\text{CS}}$).

We adopt three different piecewise functions to represent the evolution of the scale of differential rotation between the equator and at a latitude of 60° . The adopted piecewise functions reflect observation ([Saar, 2011](#)) and model-motivated ([Brun et al., 2022](#)) scalings of latitudinal shear with R_o : the effect that they have on the observed rotation period is physically motivated.

The first is the observational trend described in [Saar \(2011\)](#), where the scale of differential rotation grows with $R_o^{2.5}$ while $R_o \leq 0.45$ and is constant above this limit,

$$\frac{\Delta\Omega}{\Omega_{\text{eq}}} = \begin{cases} 0.2/(0.45^{2.5}) R_o^{2.5} & R_o \leq 0.45; \\ 0.2 & 0.45 \leq R_o < 1.3; \\ -0.2R_o^q / 1.6^q + 0.4 & 1.6 \leq R_o < 2.3; \\ -0.2 & R_o > 2.3, \end{cases} \quad (4.2)$$

where $\Delta\Omega$ is the difference between the equatorial rotation rate and the rotation rate at a latitude of 60° , Ω_{eq} is the equatorial rotation rate ($2\pi/P_{\text{eq}}$). We have ensured continuity between latitudinally-flat ($R_o \leq 0.45$), equator-fast rotation ($0.45 < R_o \leq 1.6$) with the prefactor $0.2 / 0.45^{2.5}$ as well as in the transition from equator-fast to equator-slow rotation ($R_o \sim 2$) through the introduction of the term $-0.2 R_o^q / 1.6^q + 0.4R_o$ when $1.6 \leq R_o < 2.3$. The term

$-0.2 R_o^q / 1.6^q$ slowly decreases $\frac{\Delta\Omega}{\Omega_{\text{eq}}}$ above $R_o = 1.6$. At the same time, the factor of 0.4 ensures a continuous transition when the scale of differential rotation transitions to saturated equator slow rotation at $R_o = 2.3$. Here, q is the solution to $0.2(2.3/1.6)^q + 0.4 = -0.2$, we adopt $q \approx 3.01$. This results in a transition from equator-fast to equator-slow rotation at $R_o \sim 2$.

The transition between equator-fast and equator-slow latitudinal differential rotation requires some discussion. There are no statistically significant observations of equator-slow latitudinal differential rotation. On the other hand, models predict a transition from equator-fast to equator slow-differential rotation around the solar Rossby number, $R_o \sim 2$, (Brun et al., 2022). However, the parameter space of rotation rates and stellar mass that have been investigated is small, owing to the large computational requirements needed to run these models. Therefore the exact nature of this transition is unknown. Our prescription for this transition is, therefore, not physically motivated. However, we have attempted to avoid what we believe to be an unphysical instantaneous transition by including the power law transition explained above. As this work constitutes a qualitative exploration of the effect of differential rotation on the observed rotation periods of stars, we will only comment on the general effects of this transition on the observed distribution of rotation periods under the effect of latitudinal differential rotation.

The other two relations we adopt reflect two cases for the transition of the scale of differential rotation that are steeper than the Saar (2011) relation that fall within the range suggested by the edges of the scale of differential rotation in Brun et al. (2022) (See Figure 8 in their work). These relations are:

$$\frac{\Delta\Omega}{\Omega_{\text{eq}}} = \begin{cases} 0.35 / (0.45^4)R_o^4 & R_o \leq 0.45; \\ 0.35 & 0.45 \leq R_o \leq 1.6; \\ -0.35 R_o^q / 1.6^q + 0.7 & 1.6 \leq R_o < 2.3; \\ -0.35/(2^2)R_o^2 & 2.3 \leq R_o, \end{cases} \quad (4.3)$$

and

$$\frac{\Delta\Omega}{\Omega_{\text{eq}}} = \begin{cases} 0.35 / (0.45^8)R_o^8 & R_o \leq 0.45; \\ 0.35 & 0.45 \leq R_o \leq 1.6; \\ -0.35 R_o^q / 1.6^q + 0.7 & 1.6 \leq R_o < 2.3; \\ -0.35/(2^2)R_o^2 & 2.3 \leq R_o, \end{cases} \quad (4.4)$$

we have ensured continuity between latitudinally-flat and equator-fast rotation regimes with the prefactors $0.35 / (0.45^8)$ and $0.35 / (0.45^4)$ and we have adopted again adopted continuous variation between the equator-fast and equator-slow regimes using the term $-0.35 R_o^q / 1.6^q + 0.7$ for $1.6 < R_o < 2.3$. Here, q retains the same value as in Equation 4.2. We have chosen these two relations to investigate the effect of the steepness of the relation between differential

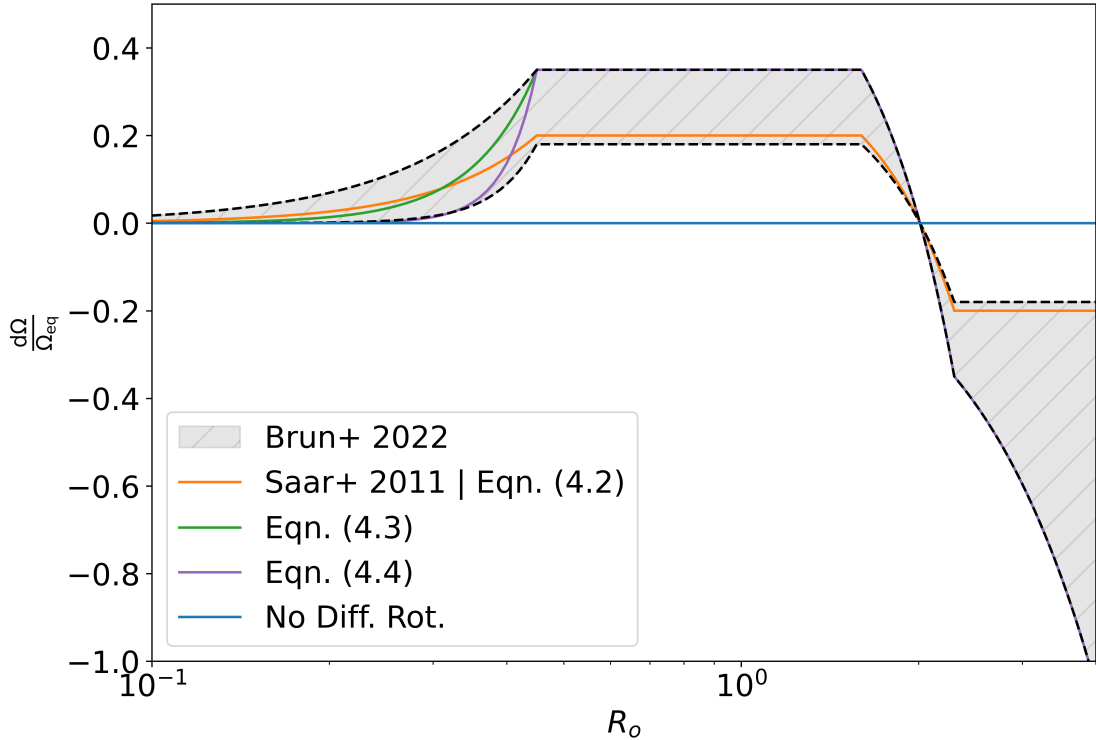


FIGURE 4.2: The relationships between latitudinal differential rotation and the R_o adopted in this work. We compare the observationally derived relation from [Saar \(2011\)](#) (Equation 4.2, orange) and two steeper relations (Equations 4.3 and 4.4, green and purple, respectively). The scale of differential rotation is greater for the latter two relations. Further, the scale of equator-slow differential rotation grows for $R_o \geq 2$. All three relations are consistent with the magnetohydrodynamic investigations into stellar differential rotation from [Brun et al. \(2022\)](#).

rotation and R_o on the observed rotation period distribution and the effect of an increase to the scale of equator-slow differential rotation for $R_o > 2$. These two relations are consistent with the range of the scales of differential rotation suggested by the magnetohydrodynamic models of [Brun et al. \(2022\)](#).

The relations we adopt in this work are shown in Figure 4.2, where we show the relation determined in [Saar \(2011\)](#) (Equation 4.2) in orange, and the two steeper relations (Equations 4.3 and 4.4) in green and purple respectively.

We adopt a second-order equator-fast differential rotation profile with the rotation rate with latitude, θ ,

$$\Omega(\theta) = \Omega_{\text{eq}} - \frac{\Delta\Omega}{\sin^2 60^\circ} \sin^2 \theta \quad (4.5)$$

where the factor $\frac{1}{\sin^2 60^\circ}$ ensures that the rotation rate is $\Delta\Omega + \Omega_{\text{eq}}$ at $\theta = 60^\circ$ (from the definition of $\Delta\Omega$). Given the equatorial rotation rate, this provides us with our expression for our stars' latitudinal differential rotation profile.

Calculating the observed rotation rate, and thus the observed rotation period, from this distribution requires some thought. We calculate the observed rotation rate from the integral of the

rotation rate distribution with θ divided by the surface area both over the maximum and minimum latitudes that the spots are expressed. Indeed, this value does not directly map to what would be measured by analysing the light curve. This is because, as suggested in [Aigrain et al. \(2015\)](#), the measured rotation period of stars can be dominated by stochastic, long-lived large stellar spots, so two stars with the same underlying spot probability distribution can have widely different measured periods, depending on when they are observed. Therefore, our calculation of the observed period here is a qualitative representation of the effect of latitudinal differential rotation on the measured rotation period.

An accurate prescription for variations in the latitudinal distribution of the stellar spots is also unknown. The latitudinal distribution of stellar spots on the surface of the Sun is well known (see, e.g., [Maunder, 1904](#); [Hathaway, 2015](#)). While we could adopt a solar distribution, this does not account for variations between stars. For example, the latitudinal distribution of active regions varies along the stellar magnetic cycle (see, e.g., [de Grijjs & Kamath, 2021](#), and references therein). Further, adopting such a distribution would not account for star-to-star variations with stellar mass, equatorial rotation rate, and the scale of differential rotation both radially and latitudinally. For this reason, the treatment of the distribution of stellar spots is a major source of uncertainty in our work. For now, we adopt a uniform distribution of stellar spots between the latitudes of 0° and 60° .

We will also assume here that all stars in our sample are viewed equator-on. While this is not the case for all stars, the rotation period gap is not an effect of the observation angle. Line-of-sight differences due to stellar inclinations can also introduce biases to the measured rotation periods. Stars must be viewed close to equator-on for stellar spots to introduce significant variations to the light curve as a star rotates. Further, inclination angles are uniformly distributed in $\cos i$, and therefore, most stars with measured rotation periods must be close to equator-on.

The observed rotation rate is then

$$\Omega_{\text{obs}} = \int_{\theta_{\min}}^{\theta_{\max}} \Omega(\theta) \cos(\theta)^2 d\theta / \int_{\theta_{\min}}^{\theta_{\max}} \cos(\theta)^2 d\theta, \quad (4.6)$$

where rotation rate is independent of radius and azimuthal angle, and their contributions cancel. Here θ_{\max} and θ_{\min} are the upper and lower bounds of the distribution of spots on the surface of the star. The factor $\cos(\theta)^2$ arises by accounting for the angle between the surface normal and line-of-sight ($\cos(\theta)$) and the spherical coordinate Jacobian ($\cos(\theta)$). As the rotation profile is symmetric about the equator of rotation, we only need to calculate the contribution to the rotation rate in one hemisphere.

We begin by comparing the effect of each of the chosen relations between differential rotation and R_o on the observed rotation period of a $0.7M_\odot$ star in Figure 4.3. Latitudinal differential rotation introduces significant biases to the observed rotation periods. The number of stars with

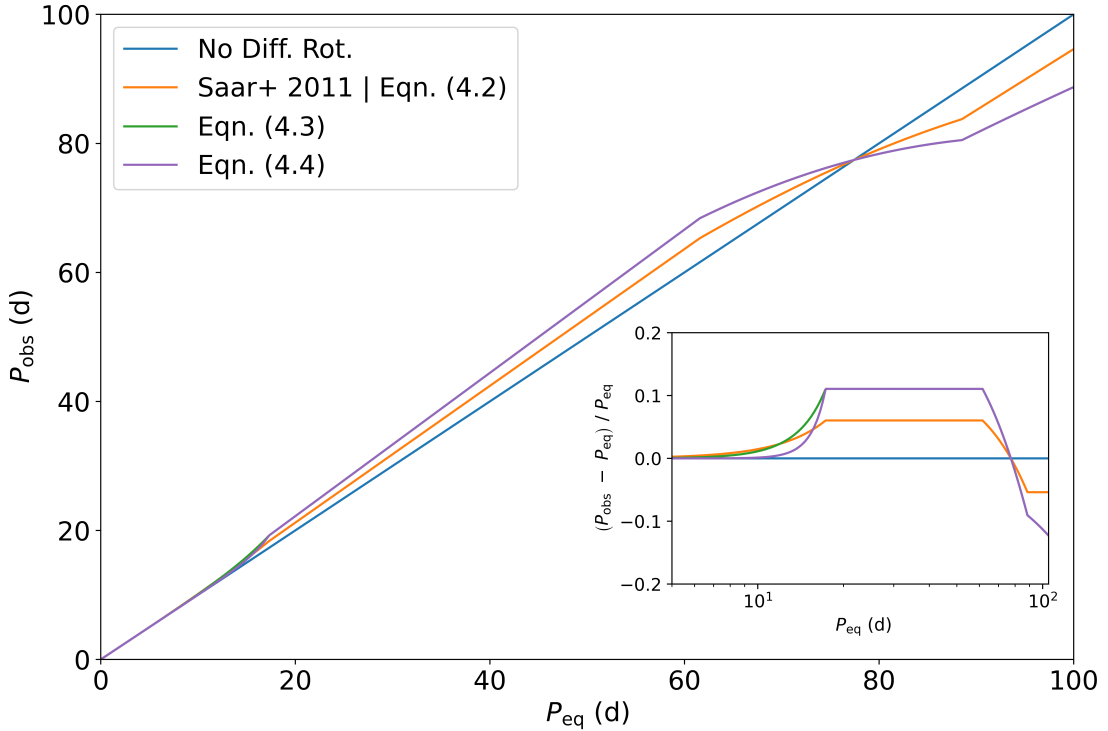


FIGURE 4.3: The effect of the differential rotation on the observed rotation period of a $0.7 M_{\odot}$ star against the equatorial rotation period. Here, the colour of the relations corresponds to the adopted differential rotation relation in Figure 4.2 compared to the observed rotation profile of a latitudinally-flat rotating star (blue), where the equatorial rotation period is the observed rotation period. At $R_o < 0.45$ for equatorial rotation periods (P_{eq}) less than 15 days, it is evident that steeper relations between R_o and the scale of differential rotation lead to more rapid growth in observed rotation periods for the same equatorial rotation period. Moreover, a steeper growth in the observed rotation period corresponds to a lower number of observed stars with that particular rotation period. The transition from equator-fast to equator-slow rotation occurs at $P_{\text{eq}} \sim 80$ days. The transition from the observed rotation period being greater than the equatorial rotation period results in a larger number of stars observed with similar rotation periods compared to the equator fast-regime **Inset:** The fractional period difference between the observed and equatorial rotation periods. The relation observed in this Figure is the same as is observed in Figure 4.2 but highlights the variance in the growth of the difference between the two steep relationships (green and purple), which is not visible when just comparing the observed and equatorial rotation periods. Despite being unable to differentiate between the two in this Figure, we will find that they introduce significant variations to the observed rotation period distribution.

similar observed rotation periods is related to the gradient of P_{obs} against P_{eq} : larger gradients result in an under-density of observations while smaller gradients result in an over-density of observations both relative to the equatorial period distribution. The growth of differential rotation below $R_o < 0.45$ occurs where $P_{\text{eq}} < 15$ d. Steeper relations of R_o with the scale of differential rotation in this domain result in a quicker growth in observed rotation periods for the same equatorial rotation period. The steeper the growth of the observed rotation period, the lower the number of stars that would be observed with that rotation period. The transition from equator-fast to equator-slow differential rotation is shown at $P_{\text{eq}} \sim 80$ d.

Now, we consider how the bias to rotation periods brought about by differential rotation affects the observed rotation period distribution. To do this, we assume a sample of stars that are uniformly distributed in effective temperature $\mathcal{U}(3500, 6000)$ and equatorial period $\mathcal{U}(0, 55)$ days, where $\mathcal{U}(a, b)$ denotes a uniform prior between a and b . The bounds of these distributions are not physically motivated; they only need to include the regimes where $R_o = 0.45$ and 2 to observe the effect that the transitions between latitudinally-flat, equator-fast, and equator-slow rotation have on the observed rotation period distribution. We draw 100,000 effective temperatures and equatorial periods from these distributions and calculate the observed rotation periods under the adopted relationships between differential rotation and R_o (Equations 4.2, 4.3, and 4.4). We plot the equatorial period and observed rotation periods under each of these relations as a 2D histogram in Figure 4.4. We have also indicated in each panel the transitions between latitudinally-flat to significant equator-fast differential rotation (dashed line, $R_o = 0.45$), and equator-fast to equator-slow differential rotation (dashed line, $R_o = 2$). Our models predict a dearth of observations, coincident with the intermediate period gap due to the transition from latitudinally-flat to significant equator-fast differential rotation. This can be seen by comparing the top left panel to the other three. The distinctness, or rather the decrease in density of stars within the gap, increases with the power on R_o (2, 4, and 8 for Equations 4.2, 4.3, 4.4 respectively) within the transition between latitudinally-flat to significant equator-fast differential rotation, $R_o \leq 0.45$. We also find that our models predict an over-density of observations where the transition from equator-fast to equator-slow latitudinal differential rotation occurs ($P = 25$ d, $T_{\text{eff}} = 6000$ K).

4.2.2 A physically motivated synthetic sample of observed rotation periods

We require a physically motivated synthetic sample of rotation periods to compare our model observed rotation periods to the measured rotation period distribution of [McQuillan et al. \(2014\)](#).

We adopt equatorial rotation periods (P_{eq}) from cluster-tuned rotational isochrones for a given stellar age and mass (these rotational isochrones are shown in Table A1 in [Spada & Lanza \(2020\)](#)). The ages of these isochrones are limited to the solar age (4.5 Gyr), placing an upper limit on the age of our population. The use of their rotation periods in this work warrants some discussion. In their work, they propose a model of rotation period evolution that a wind braking and 2-zone (core and surface) mass-dependent angular momentum transport. They tune the wind-braking and core-envelope coupling timescale through the measured rotation periods of young clusters: Pleiades (120 Myr; [Rebull et al., 2016](#)), Praesepe (700 Myr; [Douglas et al., 2017, 2019](#)), and NGC 6811 (1 Gyr; [Curtis et al., 2019](#)) as well as the rotation period of the Sun (4.5 Gyr). The adopted rotation period of the Sun in their work is also the average rotation period scaled by the latitudinal distribution of sunspots (26.9 d). This value is notably much closer to the Sun's equatorial rotation period (~ 25 d) than the polar rotation period (~ 31 d).

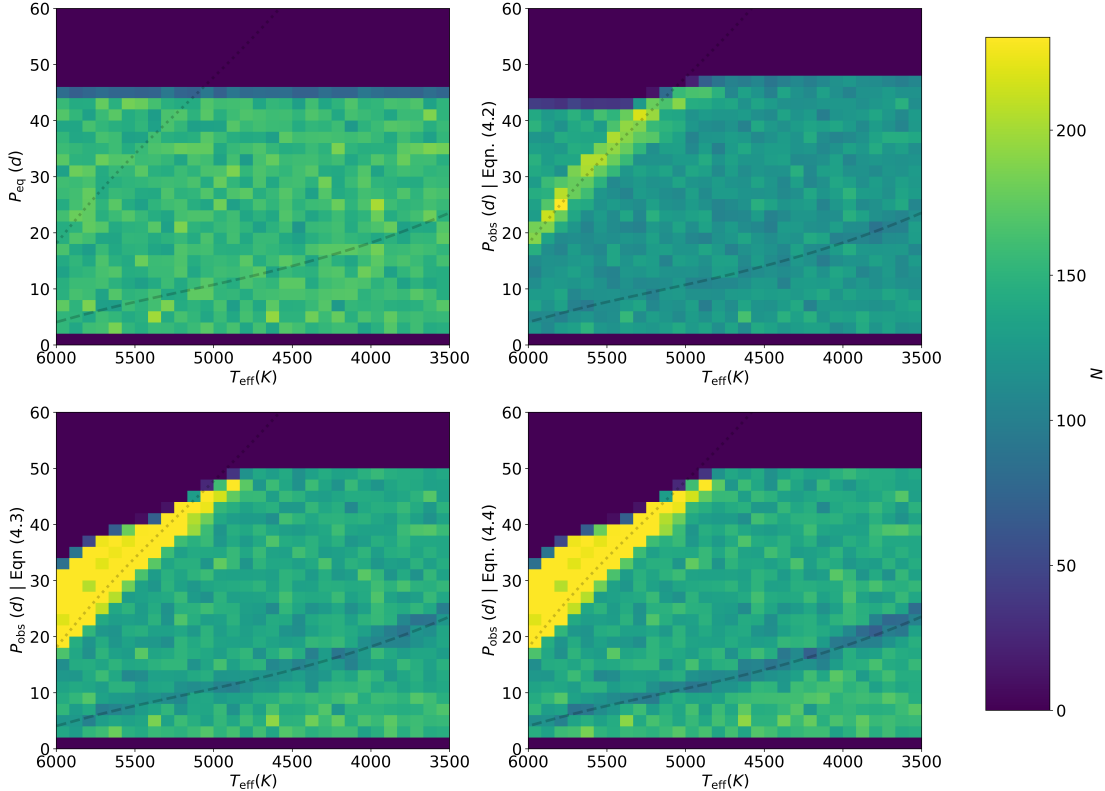


FIGURE 4.4: The effect of differential rotation on the observed rotation period distribution of a sample of stars with uniformly distributed effective temperature and equatorial rotation period. We show the 2D histograms of the equatorial rotation period (top left) against effective temperature as well as the observed rotation periods under each of the adopted differential rotation relations: Equations 4.2 (top right), 4.3 (bottom left), and 4.4 (bottom right). The transitions between latitudinally-flat to significant equator-fast differential rotation ($R_o = 0.45$), and equator-fast to equator-slow differential rotation ($R_o = 2$) are shown in dashed and dotted lines, respectively. Our models predict a dearth of observations, coincident with the intermediate period gap due to the transition from latitudinally-flat to significant equator-fast differential rotation and an over-density of observations at the transition from equator-fast to equator-slow rotation.

If we assume that latitudinal differential rotation introduces biases to the measured rotation period, then tuning models using measured rotation periods and not accounting for the bias (that latitudinal differential rotation may introduce) could result in inaccurate prescriptions of the evolution of rotation. The measured rotation periods used to tune our generative model of what we assume are equatorial rotation periods are shown in Figure 4.5. We have also plotted the line $R_o = 0.45$, where we assume equator-fast latitudinal differential rotation becomes significant and impacts the observed rotation period. Most high-temperature (> 5000 K) Pleiades and Praesepe members lay above this line. The measured rotation periods of high-mass stars in their work are not equatorial but, in fact, already the biased, measured rotation periods. We will introduce a bias to our sample’s potentially already biased rotation periods for high-mass stars. On the other hand, low-mass stars (> 5000 K) lay below this line. The measured rotation period of these low-mass stars is the equatorial rotation period, and the model may be tuned to only the

equatorial rotation periods of low-mass stars. Older (> 1 Gyr) low-mass rotation periods output by their model are projections of equatorial rotation periods. Given that the introduced dearth is most apparent for low-mass stars older than 1 Gyr, we believe adopting these values as the equatorial rotation periods is appropriate.

We also compare in this Figure the rotation period distributions of each cluster against the rotation periods of the [Spada & Lanzafame \(2020\)](#) model evaluated at the representative ages of each of the clusters (dashed lines). While this model generally agrees with the high-mass members of the clusters, it was tuned to (Pleiades, Praesepe, NGC 6811), as well as the high-mass members of NGC 6819 (2.5 Gyr; [Meibom et al., 2011](#)), and Ruprecht 147 (2.7 Gyr; [Curtis et al., 2020](#)), it significantly over-predicts the rotation periods of low-mass stars. This is especially pervasive for stars with effective temperatures less than 4000 K. This results in very few low-mass stars with rotation periods that place them on the lower branch of the intermediate period gap and an over-density of measured rotation periods of low-mass stars. We, therefore, exclude stars with effective temperatures less than 4000 K from our synthetic sample. While this leaves us with a small range of effective temperatures that we adopt in our work, where the output rotation periods from their model are the equatorial rotation periods, the gap is still apparent in this range: we can see, qualitatively, if the bias introduced by differential rotation produces a gap consistent with the measured rotation periods. We will revisit this assumption in reference to our conclusions in Section 4.4.

We generate 30,000 main-sequence and early post-main-sequence stars with various mass, age, metallicity and equatorial rotation period values. We drew masses from a uniform mass function $\mathcal{U}(0.65, 1) M_{\odot}$. This limits our range of masses to those with a convective surface and radiative core and an effective temperature greater than 4000 K. The gap is apparent in this range ($T_{\text{eff}} < 5000$ K). The choice of a uniform initial mass function here is motivated by the selection function of the *Kepler* mission being biased towards the observation of brighter stars. We assume that the selection function effectively cancels out the bias towards a larger number of low-mass stars of physically motivated initial mass functions like a Salpeter initial mass function.

Metallicity is drawn from a distribution to approximately reflect what is observed in the Milky Way. Specifically, we defined a variable ϕ to be drawn from a Beta distribution

$$\phi \sim \mathcal{B}(\alpha = 10, \beta = 2) \quad (4.7)$$

and applied a transform from ϕ to [Fe/H] by requiring the metallicities be bounded between $[\text{Fe}/\text{H}]_{\min} = -2$ and $[\text{Fe}/\text{H}]_{\max} = +0.5$. We also required that the mode of ϕ , defined as $\frac{\alpha-1}{\alpha+\beta-2}$ for a Beta distribution, occurs at Solar metallicity. This leads to the transform:

$$[\text{Fe}/\text{H}] = \left([\text{Fe}/\text{H}]_{\max} - [\text{Fe}/\text{H}]_{\min} \right) \left(\phi - \frac{\alpha-1}{\alpha+\beta-2} \right) \quad . \quad (4.8)$$

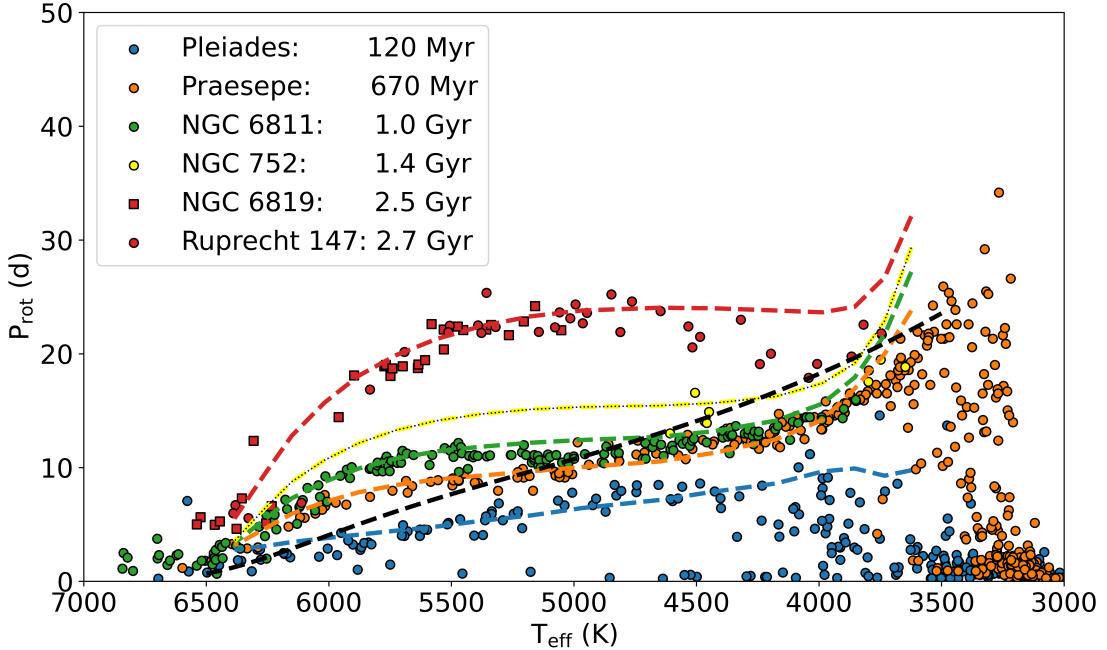


FIGURE 4.5: Scatter plot of clusters, Pleiades (blue, 120 Myr; Rebull et al., 2016), Praesepe (orange, 700 Myr; Douglas et al., 2017, 2019) and NGC 6811 (Curtis et al., 2019, green, 1 Gyr;), used to tune the rotational isochrones adopted in this work (Spada & Lanzafame, 2020) as well as the rotational period distributions of NGC 752 (yellow, 1.4 Gyr; Agüeros et al., 2018), NGC 6819 (red squares, 2.5 Gyr - projected forward to 2.7 Gyr: scaled through Skumanich spin-down, for direct comparison with the Ruprecht 147 sample; Meibom et al., 2011), and Ruprecht 147 (red circles, 2.7 Gyr; Curtis et al., 2020) against effective temperature. **Dashed lines:** (Spada & Lanzafame, 2020) rotational isochrones evaluated at the ages of each stellar cluster and coloured to match the scatter points. We have also shown the line $R_o = 0.45$ (black dashed), highlighting that the high temperature (5000K) Pleiades and Praesepe members may have significant latitudinal differential rotation, biasing the measured rotation periods, while low-temperature stars may not. Suggesting that the measured rotation period of these stars is the equatorial rotation period, and adopting the Spada & Lanzafame (2020) values as the equatorial rotation periods is appropriate for low-mass stars. We also show the rotation periods evaluated by the Spada & Lanzafame (2020) model evaluated at the representative ages of each cluster (dashed lines coloured by the cluster of the same age). While this model generally agrees with the high-mass members of the clusters, it was tuned to (Pleiades, Praesepe, NGC 6811), as well as the high-mass members of NGC 6819, it significantly over-predicts the rotation periods of low-mass stars. This is especially pervasive for stars with effective temperatures less than 4000K.

The stars we generate mock data for in this work span from the ZAMS to low-luminosity subgiants. We draw equivalent evolutionary phase (EEP) values⁴ from a uniform distribution of EEPs $\mathcal{U} \sim (200, 450)$. The bounds of this range represent the ZAMS and the low-luminosity subgiant phase, respectively. Using the EEP, mass, and metallicity, we interpolate a position along the MIST stellar isochrones (Morton, 2015) to calculate the expected T_{eff} , and luminosity of each star, as well as the post-ZAMS age. This results in a population biased towards younger (< 1 Gyr) stars. We found that after calculating the equatorial rotation periods under

⁴The principle of the EEPs is to define physically significant stages in stellar evolution (e.g. core-H burning, core-H depletion, RGB), and then subdivide each of these stages into a number of equal steps. See Morton (2015) for a more in-depth discussion of the definition of these values.

this population, the rotational period distribution had a much higher density of observations of low rotational periods than the [McQuillan et al. \(2014\)](#) sample, ensuring comparison between the two is not biased by the choice of age distribution. We sampled our population until we had a population uniform in age between 300 Myr and 4.5 Gyr, ensuring the sample was on the slow-rotator sequence but younger than the solar age. From these parameters, we can then calculate the observed rotation periods of our synthetic sample.

4.3 Results

The resulting distributions of observed rotation periods (blue, orange, green and purple) relative to the measured rotation period distribution of *Kepler* ([McQuillan et al., 2014](#)) (black) are shown in Figure 4.6. Here, the colour of each distribution corresponds to the same colour, showing the relation between differential rotation and R_o in Figure 4.2 and blue corresponds to the equatorial, or latitudinally-flat rotation profile, observed rotation period.

Figure 4.7 shows how the adopted relations impact the rotation period distributions. The left column shows the 2D histogram of the [McQuillan et al. \(2014\)](#) measured rotation period distribution. In the middle column, we show the 2D histogram of the observed rotation period distributions under the adopted relations between latitudinal differential rotation and R_o . From top to bottom panel, we show the equatorial rotation periods from our generative model (with no latitudinal differential rotation), then under the [Saar \(2011\)](#) Equation (4.2) differential rotation relation, then with the Equation (4.3) model, and finally with the Equation (4.4) model. These panels correspond to the blue, orange, green, and purple distributions in Figure 4.2 respectively. All of the panels in the left two columns are coloured by the number of stars in each bin for each panel: $N_{\text{Obs.}}$, the number in each bin of the [McQuillan et al. \(2014\)](#) sample, for the left column and $N_{\text{Mod.}}$, the number in each bin of the various models, for the middle column. In the right column, we show the difference between the distributions through $N_{\text{Obs.}}$ and $N_{\text{Mod.}}$ for each adopted relation. Darker colours correspond to regions where the model over-predicts observations and lighter where the model under-predicts observations.

Like in Figure 4.4, our models predict a dearth of observations, coincident with the intermediate period gap as a result of the transition from latitudinally-flat to equator-fast differential rotation at $R_o = 0.45$. We observe that the model that adopts latitudinal differential rotation when calculating the observed rotation period reduces the disparity between the model observed and measured rotation period distributions: compare the top panel to the bottom three in the right column of Figure 4.7. Further, the increased density of observations of stars just above the intermediate period gap in the *Kepler* sample is reproduced under this model, unlike a model of extreme magnetic braking to explain the gap. We again observe that increases with the power on R_o (2, 4, and 8 for Equations 4.2, 4.3, 4.4 respectively) increase the distinctiveness (relative

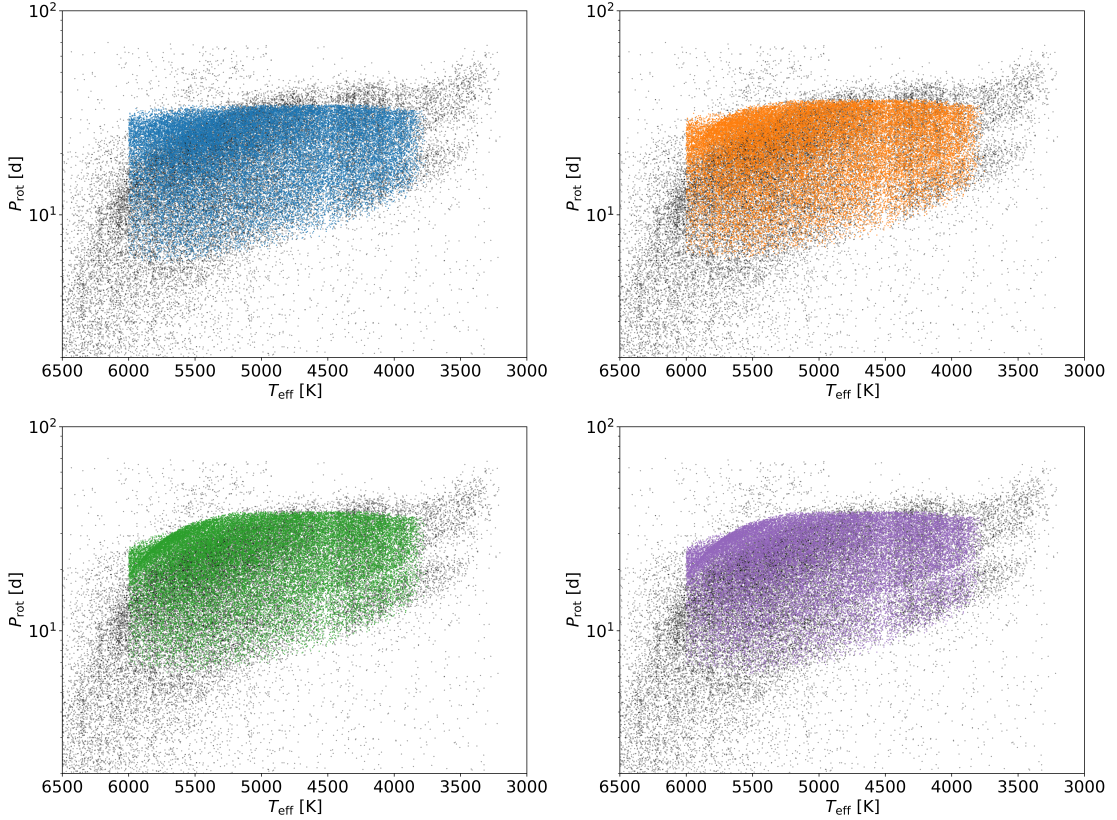


FIGURE 4.6: The observed rotation period distributions of the synthetic sample of stars given various relations between latitudinal differential rotation and R_o overlayed over the measured distribution of rotation periods of the Kepler sample from [McQuillan et al. \(2014\)](#) (black). Here, the coloured observed rotation period distributions correspond to the various differential rotation relations adopted in this work, as seen in Figure 4.2. The latitudinally-flat (blue, top left) sample reflects the equatorial rotation periods of our sample considered in this work. We observe no intermediate period gap in this synthetic sample of stars without differential rotation. We observe the effects of latitudinal differential rotation on the observed rotation period. We tentatively observe a dearth of observations at the transition between latitudinally-flat ($R_o < 0.45$) and equator-fast rotation, which occurs precisely at the location of the intermediate period gap. To more thoroughly investigate the introduced variations, we have plotted the 2D histograms of these distributions to qualify and make comparisons between the measured and model observed rotation distributions in Figure 4.7.

decrease in density of observations) of the gap. We also find that all models predict an over-density of stars where the transition from equator-fast to equator-slow latitudinal differential rotation occurs ($\log P_{\text{rot}}/d = 1.2$, $T_{\text{eff}} = 6000 \text{ K}$), coinciding with the long-period pile-up. The model also predicts this over-density with no differential rotation, but the shape of the distributions in this domain do not agree. When we introduce differential rotation, however, the shape of the upper edge of the model observed rotation period distributions closely matches the shape of the measured rotation period distribution. The coincidence of the position of the over-density predicted by our model and the long-period pile-up may suggest that, in fact, the cause of the long-period pile-up is this transition.

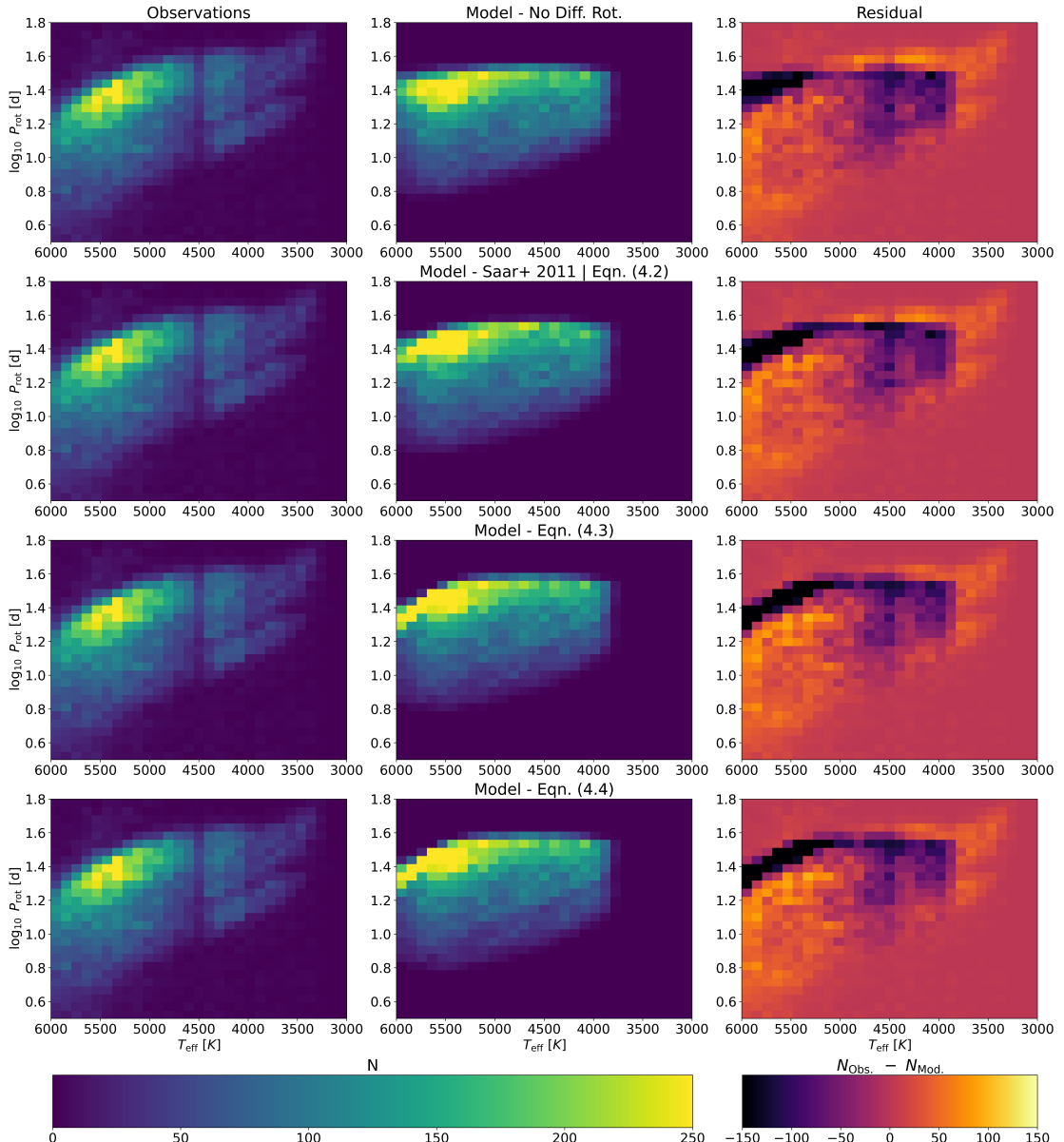


FIGURE 4.7: 2D histograms of measured and the synthetic observed rotation period distribution assume various relations between the scale of differential rotation and R_o and the difference between the two. **Left:** 2D histogram of the McQuillan et al. (2014) rotation period distribution. **Middle:** 2D histogram of the measured rotation period distributions under the adopted relations between latitudinal differential rotation and R_o . From the top to the bottom panel, we show the equatorial rotation periods from our generative model (with no latitudinal differential rotation), then the relation under the Saar (2011) differential rotation relation (Equation 4.2), then with two steeper but physically probable (Equation 4.2) and two model-motivated (Brun et al., 2022) scale of differential rotation relations Equations 4.3, 4.4. These distributions correspond to the blue, orange, green, and purple distributions in Figure 4.2 respectively. All of the panels in the two left columns are colour by the number of stars in each bin: $N_{\text{Obs.}}$, the number in each bin of the McQuillan et al. (2014) sample, for the left column and $N_{\text{Mod.}}$ for the middle, the number in each bin of the various models. **Right:** The difference between the distributions: $N_{\text{Obs.}} - N_{\text{Mod.}}$ for each adopted relation. Darker colours correspond to regions where the model over-predicts observations and lighter where the model under-predicts observations. Accounting for differential rotation when determining the expected observed rotation periods of stars introduces a decrease in the density of observations where significant equator-fast differential rotation arises. The dearth is coincident with the intermediate period gap. We find that the larger the power in the relation between $\frac{\Delta\Omega}{\Omega_{\text{eq}}}$ and R_o below the transition to a saturated scale of differential rotation (2, 4, and 8 for Equations 4.2, 4.3, 4.4 respectively), the more apparent the dearth becomes. Our models predict an over-density of stars where the transition from equator-fast to equator-slow latitudinal differential rotation occurs ($\log P_{\text{rot}}/d = 1.2$, $T_{\text{eff}} = 6000$ K) which aligns with the position of the long-period pile-up.

4.4 Discussion

In this Chapter, we have proposed a novel explanation for the intermediate period gap: the growth equator-fast differential rotation near the location of the intermediate period gap and the effect that this has on the observed rotation periods of stars. Our hypothesis is built only upon an existing theoretical prescription for how latitudinal rotation evolves in stars, and then quantifying the impact this would have on observable quantities. The two leading theories are that either: stars in the intermediate period gap drop below the detectability threshold suggested by the drop in photometric variability; or that stars "jump" the intermediate period gap through sudden enhanced magnetic braking. In Appendix A of this thesis, we have discussed an investigation into evidence against these explanations, which we believe suggests that they are not the underlying mechanism of the intermediate period gap.

In this work, we consider the effect of latitudinal differential rotation on the observed rotation periods of main-sequence stars. To do this, we developed a model to predict the observed rotation period of stars given models of surface latitudinal differential rotation growth from observational and 2D magnetohydrodynamical simulations of rotating main-sequence stars. The observations of latitudinal differential rotation and magnetohydrodynamical models of latitudinal differential rotation with R_o agree - suggesting that latitudinal differential rotation grows from latitudinally-flat to equator-fast differentially rotating at a $R_o \approx 0.45$. Introducing this differential rotation to our calculation of the observed surface rotation period of stars produces a lower density of observations where the differential rotation grows. We believe that this suggests that the underlying mechanism of the intermediate period gap is the onset of latitudinal differential rotation. We have investigated several relationships between the scale of growth of latitudinal differential rotation and R_o . The qualitatively best-fit relations have a swift growth of $\frac{\Delta\Omega}{\Omega_{eq}}$ close to the intermediate period gap (Equations 4.3 and 4.4). We found in this work that the distinctness, or rather the decrease in density of stars within the gap, increases with the power on R_o when $R_o \leq 0.45$.

While our model predicts a dearth of observations coincident with the gap, we are hesitant to suggest a prescription for the growth of the scale of differential rotation based on our results. There is significant degeneracy between several parameters in our work, and there are still many unknowns that we have yet to account for that require future work.

We adopt a constant distribution of stellar spots between a latitude of 0° and 60° . The evolution of the latitudinal distribution of stellar spots is unknown, so we will not speculate as to whether changes to this parameter would result in our models reflecting the observed rotational distribution. However, we will note the effects that variations to this parameter have. If spots are more concentrated to the equator ($\theta_{min} = 0^\circ$ and $\theta_{max} < 60^\circ$) then the observed rotation periods more closely reflect the equatorial rotation periods. Conversely, if spots are more concentrated

toward the poles ($\theta_{\min} > 0^\circ$ and $\theta_{\max} > 60^\circ$), then differential rotation will have a larger impact on the observed rotation period distribution. The observed rotation periods will be much larger than the equatorial rotation periods. The variations that those variations make are similar to an increase in the saturated scaling of differential rotation $\left(\frac{\Delta\Omega}{\Omega_{\text{eq}}}\right)$. The larger this value, the greater the scale of the dearth region in terms of rotation period.

A more rigorous model of the latitudinal expression of stellar spots and their effect on the measured rotation period of stars is required to determine the effect of latitudinal shear on the measured rotation periods. Such an analysis could first be completed with non-uniform distributions of stellar spots on the surface of stars from magnetohydrodynamic simulations of rotating stars using a similar analysis to that performed in this work. The relation between this work's purported observed rotation periods and measured rotation periods from light curves, including differential rotation, is unclear. The effect of latitudinal shear on the measured rotation period may, in fact be minimal compared to the effect observed here.

We have adopted a uniform function to draw our stellar masses. A uniform mass distribution better reflects the mass distribution of the [McQuillan et al. \(2014\)](#) sample (a Salpeter initial mass function, for example, predicts an order of magnitude greater number of low-mass stars), but under-predicts the number of high-mass stars relative to low-mass stars. The probability density distributions generally agree when comparing the effective temperature and luminosity distributions, as seen in Figure 4.8. We believe that this assumption is representative of the observed sample, even if it is not representative of the universe. The relative distribution of rotational periods and effective temperatures between the two distributions (measured and model observed), as we have performed in Section 4.3, will not be significantly biased by the underlying mass distribution.

We argued in Section 4.1 that a physical model of the intermediate period gap must account for all of the observed features of the gap. We believe that our model reproduces a number of these features. The gap definitionally aligns with a line of constant R_o , the swift growth of equator-fast latitudinal shear occurs at $R_o = 0.45$. The model naturally reproduces the roughly equal density distribution of stars above and below the gap (See the middle columns of Figure 4.7). Stars above and below the gap are of similar age (assuming Skumanich-like spin-down of the equator rotation rate) but swiftly grow in the observed rotation period. As a result, stars above and below the gap would not be significantly observationally distinct and would be of a similar kinematic age. More theoretical work is required to determine whether some of those features arise due to latitudinal bias.

For example, it is unknown how our model interacts with fully convective stars: the variance of latitudinal shear with R_o of fully convective is unknown. On the other hand, a feature of the intermediate period gap not currently explained by our results is the decreased R_{per} of stars within the gap relative to the surrounding rotation periods. We propose a mechanism to explain

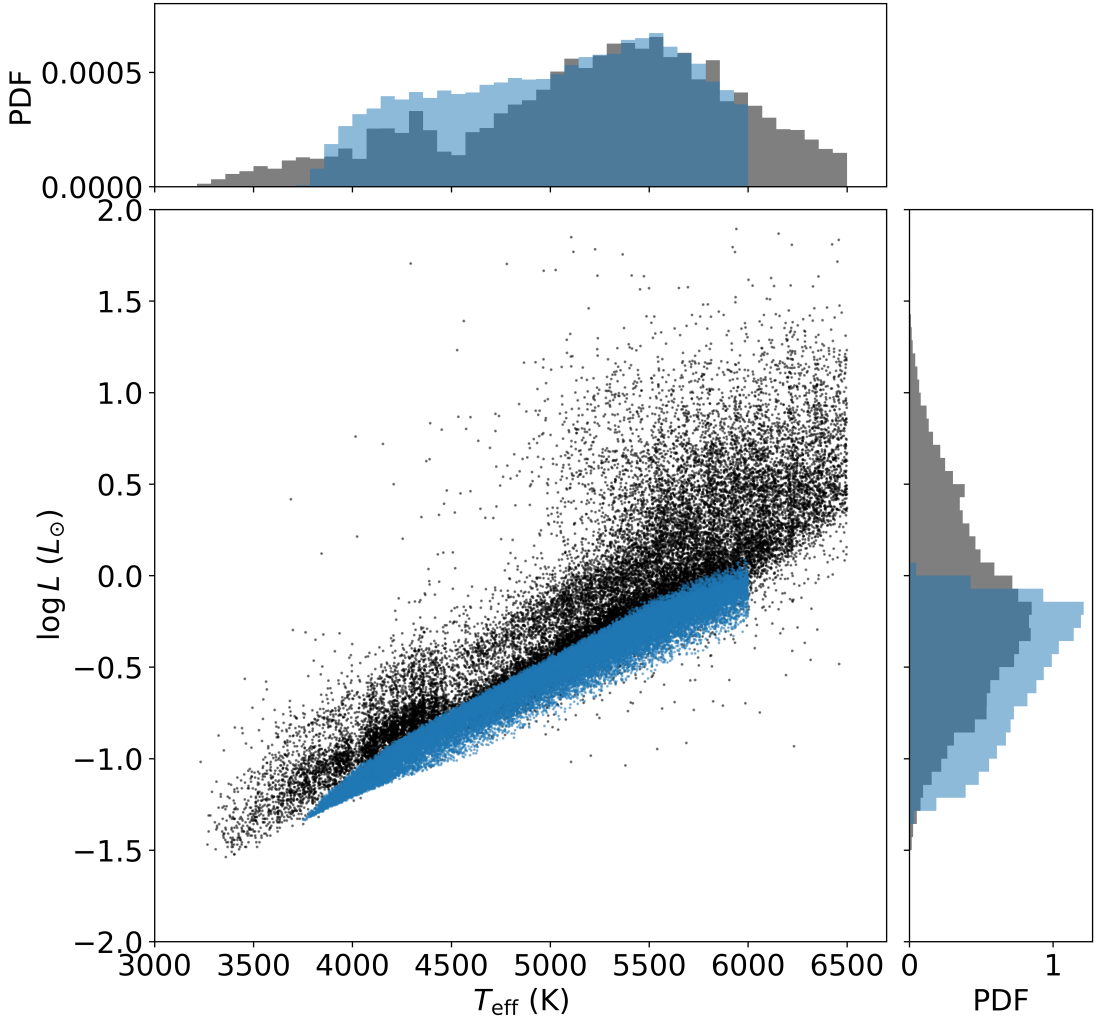


FIGURE 4.8: A scatter plot of effective temperature and luminosity distributions of the [McQuillan et al. \(2014\)](#) (black) and synthetic sample (blue) adopted in this work. On the left and above, we also show the probability density distributions of the luminosity and effective temperature, respectively. The distributions generally agree, suggesting that a direct comparison between the distributions is sound.

this feature. The fractional spot coverage of young, fast rotators ($R_o < 0.2$) is saturated. Above this regime, the fractional spot coverage drops rapidly (See Figure 7. in [Cao & Pinsonneault \(2022\)](#)). Latitudinal shear is, however, anticipated to serve as a catalyst for large-scale strong magnetic fields. Further, latitudinal shear leads to differential twisting of the poloidal field lines, resulting in a bunching of field lines that result in active regions on the surfaces of stars (see, e.g., [Berdyugina, 2005](#); [Miesch, 2005](#); [Brun & Browning, 2017](#)). As latitudinal shear grows, we, speculate that the fractional spot coverage of stars could, in turn, increase, leading to the observed increase in R_{per} above the gap. We intend to investigate this testable hypothesis by measuring the fractional spot coverage of stars above the gap. Further work to confirm the mechanism is required with more rigorous methods and theoretical investigations.

Confirmation of this model as the cause of the intermediate period gap using observational data

is difficult. Constraining the scale of latitudinal differential rotation of main-sequence stars appears improbable using current photometric methods (see Section 4.3 of [Aigrain et al., 2015](#)). However, potential observations of the differential rotation of nearby stars with Doppler imaging above and below the rotation period gap could be performed. Observations of significant variance between the latitudinal differential rotation of stars above and below the gap suggest that our model is accurate. To make a recommendation, a first step in this investigation could be observing the stars seemingly crossing the gap in the nearby open cluster Ruprecht 147 ([Curtis et al., 2020](#)).

The transition from equator-fast to equator-slow differential rotation is not well characterised in theory or observations. If this transition does occur, we expect the observed rotation periods of stars to decrease suddenly, resulting in an increased density of observations near this transition. This work shows that this increased density of observed rotation periods could arise as a result of this transition ($\log P_{\text{rot}}/d = 1.2$, $T_{\text{eff}} \sim 6000$ K). The measured *Kepler* rotation period distribution does contain a high density of stars precisely in this region, known as the long-period pile-up ([van Saders et al., 2019](#)). However, we are hesitant to suggest whether this feature results from this transition or from the selection function of *Kepler* observations being biased towards higher mass, brighter stars.

We note that the over-density is also reflected in our synthetic sample’s adopted equatorial rotation periods generated using the rotational isochrone models of [Spada & Lanzafame \(2020\)](#). Adopting this generative model also limited the mass range of stars investigated by our work to low mass (> 4000 K). The model can qualitatively reproduce the over-abundance of stars on the slow branch (below the intermediate period gap) by introducing mass-dependent core-envelope coupling. However, it greatly overestimates low-mass (< 4000 K) rotation periods for stars older than approximately 1 Gyr, likely because the oldest cluster used to tune their model (NGC 6811) is only 1 Gyr old. The gap is most apparent for stars with lower masses than this permits, limiting our investigation.

The measured rotation periods used to tune the generative model of our synthetic sample’s (assumed) equatorial rotation periods may already be potentially latitudinally biased measurements. We require an unbiased generative model of equatorial rotation periods to differentiate between these effects. However, we can only tune a physically motivated generative model of observed cluster periods with those potentially biased by latitudinal effects. Therefore, we propose a follow-up work retuning the rotational isochrone model, assuming that latitudinal effects bias the measured rotation period distributions of clusters. This work could also include the previously unincluded Ruprecht 147 ([Curtis et al., 2020](#)) and NGC6819 ([Meibom et al., 2011](#)) measured rotation period distributions, which would allow the rotational isochrones to more accurately predict the rotation periods of much older low-mass stars than the model currently reflects. A model comparison could also be performed, where one model assumes the measured

rotation periods are latitudinally biased, and one assumes they are the equator rotation periods. The parameters of their model may be significantly degenerate with the effects of latitudinal bias. Further, a flexible enough model (with or without the effects of latitudinal differential rotation) could reproduce the rotational period distributions, so a more rigorous test of the latitudinal shear model may be required.

4.5 Conclusions

In this work, we have qualitatively shown that the transition from latitudinally-flat to equator-fast differential rotation can introduce a dearth of observations in a rotation period distribution. The transition from latitudinally-flat to significant equator-fast differential rotation occurs precisely at $R_o = 0.45$ coincident with the intermediate period gap. This suggests that this is the cause of the intermediate period gap. We argue that the growth in latitudinal shear explains several features of the intermediate period gap, including the high density of stars above and below the gap and the decrease in photometric variability of stars within the gap. The scale of the introduced dearth depends on highly uncertain parameters that may be degenerate: the latitudinal distribution of stellar spots and the relationship between R_o and latitudinal shear, suggesting further explorations of the parameter space are required. These results provide a novel explanation for the intermediate period gap without the requirement of new physics and underscores the need for further research into the impact of latitudinal differential rotation on observations of surface rotation of stars across the main-sequence.

Chapter 5

Summary, Conclusions and Future Work

5.1 Summary

Rotation is an often overlooked area of stellar astrophysics and astronomy due to its complexity in modelling and observation. That being said, over the previous decades, our understanding of the evolution of rotation and its impact on stellar evolution has grown dramatically. With every observation of rotation that we make, we are learning that our simple implementations and parameterisations in stellar evolution codes do not necessarily account for a number of misunderstood mechanisms underlying the evolution of rotating stars. We are also learning that rotation can have impacts on the observations that we are able to make of stars. This is the direct result of the growth of the data boom that we find ourselves in due to the sheer number of stars we have precisely photometrically observed over long-period baselines through missions such as *Kepler* ([Borucki et al., 2010](#)), *K2* ([Howell et al., 2014](#)), *TESS* ([Ricker et al., 2014](#)) and *Gaia* ([Distefano et al., 2023](#)) .

Indeed, this thesis does not provide an exhaustive list of every single effect that rotation has on stellar evolution, nor every gap in our knowledge of its effects. In this work, we have attempted to provide novel ways to improve our understanding of rotation without requiring more data. The title of this thesis was deliberately chosen as “Problems in low-mass stellar rotation” - because, while we do work to provide methods that may lead to conclusions about the effects that rotation has on stellar evolution, these are not closed problems.

5.2 Conclusions

This thesis outlines three problems in low-mass stellar rotation and our attempts to address them through novel methods. In Chapter 2 we first investigated the subgiant angular momentum transport problem. This is the disparity between the observations of subgiants' core and surface rotation rates and expected core and surface rotation rates from rotating models of stellar evolution. Those observed core-to-surface rotation rate ratio of low-luminosity subgiants suggest angular momentum transport one to two orders of magnitude greater than the angular momentum transport currently implemented in rotating stellar evolution codes. Stronger constraints to those low-luminosity subgiants' internal rotation profile shapes would illuminate the excess angular momentum transport mechanism at play. We have shown in this thesis that, through applying distinct measurements of stellar rotation, specifically here asteroseismology and periodic photometric variability due to stellar spots, to more precisely constrain the internal rotation profile of low-luminosity subgiants. While we have only applied this method to a single star, KIC 12508433, we believe the method is easily adopted in other studies to more tightly constrain those internal rotation profiles better than either of those measurements of stellar rotation can individually - without requiring more data.

In Chapter 3 we investigate the effect that stellar rotation can have on accurate and precise measurements of atmospheric metallicity and chemical abundances. Accurate measurement of stellar metallicity can be an integral part of our understanding of the universe, from understanding the origin of elements in the universe to galactic archeology to accurate aging of open clusters. Astrophysicists rely on accurate measurements of atmospheric metallicity to constrain their models of stellar evolution, and astronomers investigate the predictions made by those models. This is a cyclic process where if astronomers do not adopt accurate models of the stellar atmosphere, inaccuracy compounds. We created a sample of synthetic spotted stellar spectra with physically motivated stellar parameters to investigate the effect of adopting a non-spotted model of the stellar atmosphere on the accuracy of recovered stellar parameters. We found that even when adopting a naive model of the effect of stellar spots through a two-temperature model of the stellar atmosphere, stellar spots introduce a mean scatter of 0.03 to the measured metallicity of main-sequence stars. This effect is non-negligible. A spotted model of the stellar atmosphere should be adopted, or the effect that this level of imprecision can have on our inferences of astrophysics should be considered, especially where precise inference of stellar metallicity is required.

Finally, this thesis investigates the intermediate period gap in Chapter 4. The intermediate period gap is an unexplained phenomenon manifesting as a dearth of observations of particular stellar surface rotation periods from photometric variability due to stellar spots. We propose, through a series of data tests in Appendix A that leading theories do not appear to explain the observed features of the gap adequately. We propose another cause for the intermediate period

gap: the onset of equator-fast latitudinal differential rotation at $R_o \sim 0.45$ and the variability of the distribution of stellar spots (latitudinally) on the surfaces of stars. We generate a sample of physically motivated stellar rotation periods and calculate their observed rotation periods given multiple relationships between the scale of differential rotation and R_o . Paradoxically, equator-fast differential rotation introduces a bias to larger observed rotation periods. This, in conjunction with a swift increase in the scale of differential rotation just below $R_o < 0.45$ creates a dearth of observations resulting in the gap at $R_o \sim 0.5$, precisely aligning with the intermediate period gap. While this result requires more thorough investigations into the effect of latitudinal differential rotation on the stellar light curve and, therefore, observed rotational period, this is a novel proposal that we argue explains all of the observational counterparts¹ to the intermediate period gap without the requirement of new, and complex, physics.

5.3 Future Work

5.3.1 Applications of our work

In this work, we have presented representative studies that provide methods for improving our understanding of rotation in stars. All of these works have further applications for the wider rotational astronomic community.

Applying a surface rotation prior to inference of the internal rotation profiles of low-luminosity subgiants is a novel way to further constrain the internal rotation profiles of stars without requiring more data. Without this method, see e.g. [Ahlnborn et al. \(2020\)](#) who suggest precise measurement of up to $\ell = 10$ mode rotational splittings are required for inference of the internal rotation profile of post-main-sequence stars using only the rotational splittings, inference of the internal rotation profile of stars will require extremely long baseline observations of a number of subgiants. While plans are being made for longer-baseline asteroseismic missions ([Rauer et al., 2014](#); [Akeson et al., 2019](#); [Miglio et al., 2021](#)) the length of the missions required for such investigations (on the order of 10s of years) appear unfeasible - given the recent track record of the length of observational missions. We propose that this method be applied to our observations of post-main-sequence stars with measured rotational splittings. As we discuss in the conclusion of Chapter 2, this method can be applied to any star with observed rotational splittings and a measurement of the surface rotation rate. This can either come in the form of surface rotational period measurements from the active regions of stars, as was adopted in that work and is a by-product of time series-based photometric observation missions, or through spectroscopic $v\sin i$. The inclination angle and stellar radius, which usually plague the constraints to our measurements of stars, are independently constrained through asteroseismic investigations

¹Or lack thereof, in terms of the implied peculiarity.

of the star, making it possible to strongly constrain the surface rotation rates of stars in this way. In this respect, a good place to start is with the ~ 30 subgiant stars for which rotational splittings have been observed. The combination of the constraints to the internal rotation profiles of low-luminosity subgiants, in a population inference sense, may constrain the angular momentum transport mechanism underlying the post-main sequence angular momentum transport problem.

Regarding measuring the effect that stellar spots have on the measurement of the atmospheric metallicity of stars, several applications and extensions to our work could be adopted. The spectroscopic nature of active regions is a field in its infancy. More modelling work is required to understand how the fundamental parameters of stars other than the Sun govern their magnetic fields and the properties of stellar spots. Stellar spots likely have more complex contributions to spectra than the 2-temperature model we have adopted in that work. Further, the effect of magnetic fields, the properties of stellar spots and their effect on the stellar spectra are unknown. For some stars, Doppler imaging can indirectly determine the spot contribution to stellar flux. Investigations into the variance between spotted and unspotted stars, even through observations of the Sun, are required to parameterise the effect of stellar spots on stellar spectra more accurately.

For example, in this work, we have only considered the effect that the cooler “spot” regions have on the inference of stellar parameters. Indeed, as well as the cool regions, magnetically active regions can also be brighter or hotter than the ambient temperature of a star in the form of faculae. The relative effect of faculae is, comparatively, unknown. Algebraically, in the model we adopt, a star with a large fractional coverage of cool spots is the same as a star with a small fractional coverage of hot faculae. This suggests that scatter to inferred stellar parameters will be introduced whether you adopt spots or faculae.

The contribution of spots and faculae could be disentangled from the stellar spectra using the method we adopt in this paper. The cancellation of the contribution to the stellar flux from spots by faculae, and vice versa, is a proposed mechanism underlying the intermediate period gap that we are currently unable to investigate. However, with a 3-temperature stellar spectra model of the stellar atmosphere, we could determine whether this is true. We propose an investigation into the feasibility of using the reduced goodness of fit between a single and 3-temperature contribution stellar spectra of the same effective temperature of stars using a single or 3-temperature contribution model of the stellar spectra.

While this method cannot be used to image the stellar spots on the surfaces of stars directly, it can be used to determine the fractional spot coverage and the relative effect that they may have on observed variations to the stellar flux. An area of concern when using the transit method for observing exoplanets is the degeneracy between transits and stellar spot contributions. This method could determine the spot contribution to the stellar spectra of stars with suspected exoplanetary transits. Exoplanet transits do not impact the stellar spectra; they simply reduce the

observed flux, but as described in our work, spots do. A lack of variation in the stellar spectra before and during suspected transits would indicate that the transit is indeed a transit.

Finally, in this work, we investigated the nature of the intermediate period gap that we conclude is created by the onset of latitudinal differential rotation and variances to the latitudinal probability density function of stellar spots. Given that this is a novel model, we propose a number of follow-up works in this Chapter and will only restate what we consider to be the most important for brevity. That being said, confirmation of this conclusion using observations is difficult. Constraining the scale of latitudinal differential rotation of main-sequence stars appears improbable using current photometric methods (See Section 4.3 of [Aigrain et al., 2015](#)). Fourier transforms of spectroscopic line profiles and time series Doppler image maps of the active regions of stars offer a possible avenue to explore in this regard (See Chapter 1). We know at what observed rotation periods stars are below and above the gap, so a good first step would be to determine the scale of differential rotation (and stellar spot distribution) of stars with similar masses and varying observed stellar rotation periods. Observation of little latitudinal differential rotation below the gap and differential rotation above the gap would provide clear evidence for this being the main mechanism at play.

Furthermore, more investigations into the evolution of magnetic activity regarding rotation are required. Only recently has the observation that magnetic activity, through the fractional spot coverage of stars, varies as a result of core-envelope recoupling been made. While our work proposes that the cause of the decreased photometric variability of stars is the decrease in gross rotation rate, followed by an increase in stellar spot coverage from latitudinal differential rotation, further work is required to determine if this is indeed the case.

5.3.2 The future of asteroseismology and observation of stellar rotation through photometric modulation

While the second *Kepler* mission ended five years ago, the data is still being investigated. A number of stars, especially low-luminosity subgiants, from which we can determine core and surface rotation rates, have yet to be asteroseismically investigated. We have shown in this work that the internal rotation profile shape of these stars cannot be measured with current measurements of the rotational splittings. The feasibility of determining the internal rotation profile of these stars without dedicated long-term photometric missions is low. That being said, the data boom we are currently experiencing regarding photometric data is not slowing. The *TESS* photometric mission has been collecting short cadence data for over 4 years. High-resolution observations of stars have been made that will bring with them a new observing field of stars through which we will be able to measure surface rotation periods and rotational splittings, especially within its continuous viewing zones. With this data, more and more stars have their

surface rotation periods ([Claytor et al., 2023](#)) and rotational splittings determined. With the accurate measurement of those quantities and the application of our proposed method to place stronger constraints on the internal rotation profile of these stars with a surface rotation rate constraint, a population inference approach appears to answer the post-main sequence angular momentum transport problem.

The future of precise measurement of stellar rotation comes from space-based high-cadence photometric missions. The Nancy Grace Roman telescope ([Akeson et al., 2019](#)), known initially as *WFIRST*, is a space-based photometric mission that will observe large patches of the sky with a faster cadence than both the *Kepler* and *TESS* missions. The telescope is expected to launch in 2026, and it will be some time before the baseline is long enough to infer stellar rotation. Proposals have been made for targeted high-precision asteroseismically focussed missions: PLAnetary Transits and Oscillations of stars (*PLATO*) ([Rauer et al., 2014](#)), the High-precision AsteroseismologY of DeNse stellar fields (*HAYDN*) mission ([Miglio et al., 2021](#)). When, or if, these missions are launched, our understanding of the nature of the rotation of stars will grow. This will be both from a larger sample of stars with more precise photometric observations and with longer baselines, which will result in more stars with a larger number of and more precise measurements of rotational splittings, as well as a larger sample of stars with photometrically measured surface rotation rates.

As we have discussed within this thesis, there are problems underlying stellar rotation that we still need the answers for, though we are making progress in answering them. We will not speculate on the next problems in the low-mass stellar rotation. However, with this level of data, we are certainly focussing on 2nd and 3rd-order effects of rotation, which will no doubt improve our understanding of the evolution of rotation in stars and its effects on the observations we make.

Appendix A

An investigation into the evidence for current explanations of the intermediate period gap

In this Appendix, we investigate the evidence for the two leading explanations for the intermediate period gap. This work is intended to be treated as a companion and motivation for Chapter 4 where we propose a novel explanation for the intermediate period gap through the onset of equator fast latitudinal differential rotation. We separate the two for ease of readability.

A.1 Introduction

There are two leading explanations for the intermediate period gap. They are, that the gap arises from a decrease in probability to observe rotation periods of stars precisely within the gap or that, through the onset of strong magnetic braking, stars suddenly “jump” in surface rotation period, leading to dearth of observations¹. We propose here that the data does not support either of these explanations. Before we can begin however it is worth discussing two concepts, the difference between the probability of observation, and the detectability of rotation period and the so-called magnetic activity indicators.

In this work we will use the terms probability of observation of rotation, and detectability of rotation period. While they are related, they are different terms. The detectability of rotation requires a relatively short cadence, on the time scale of days-weeks, observations with distinct variability in the light curve due to spots or faculae. It depends on several factors on a star-to-star basis, including the inclination angle, wherein the magnetic activity cycle observations

¹as to not repeat ourselves we direct you to our introduction of these mechanisms in Chapter 4

are made, where faculae and spots are distributed on the star's surface, and the lifetimes of these surface features relative to the star's rotation period. (Aigrain et al., 2015; Reinhold et al., 2019, 2021). The probability of observation of rotation refers to a more stellar parameter-based average statistic under the comparison of the set of stars with and without detection rotation periods. The detectability of rotation with fundamental stellar properties (temperature, metallicity, stellar age etc.) has been previously investigated. Cool stars, especially cooler than 5200K, have a significantly higher probability of rotational period observation than hotter stars. Cool stars both tend to have higher magnetic activity, and therefore more spots, and also have more significant brightness variations as a result of the same level of surface spot activity compared to hotter stars (McQuillan et al., 2014; Santos et al., 2021; Zhang et al., 2020) A relation with metallicity has also been investigated (Amard et al., 2020; See et al., 2021; Claytor et al., 2023). Higher-metallicity ($[{\rm Fe/H}] \gtrsim -0.1$) stars tend to have a higher rotation period detection rate than lower-metallicity stars. Avallone et al. (2022); Masuda (2022) separate the metallicity dependence from age and suggest that this effect arises from the fact that younger, more active stars are enriched by metals from Galactic chemical evolution rather than a result of the metallicity on the evolution of magnetic activity and probability of rotational observation. Older stars tend to have a lower probability of observation. Their rotation periods are long and thus require a longer baseline of observations, and they tend to have weaker magnetic fields and thus express a smaller number of stellar spots. Many stars cannot have their rotation periods measured purely from the inclination angle's effect on the rotation's detectability. If a star is pole-on, even if a star expresses surface features close to the axis of rotation, no variance in the brightness of that star will be detected. Increasing the sensitivity of telescopes, and methods of determining rotation periods, increase the number of stars that can have their rotation periods detected. Still, this number is bounded by the subsample of stars that cannot have their rotation measured. While the distribution of the inclination angle of stars is biased toward equator-on observations, a non-zero population of stars will never have their rotation periods detected through photometric variability.

Stellar magnetic activity indicators

Stellar magnetism is a complex component of stellar evolution that is hard to predict and model. Links between magnetism and mass, metallicity, age, convection, and rotation have been identified (Cao & Pinsonneault, 2022). These links are, however, based upon observations of stars rather than theory. The observation of rotational modulation in a light curve, and the observation of surface rotation from that modulation, requires cool spots and bright faculae created by concentrated magnetic fields near the surface of a star. Stars with stronger magnetic fields tend to express larger spot coverage, thus having larger rotational photometric modulation and more readily observable rotation periods.

Stellar activity is the collective term used to describe different effects magnetic fields have on stars. This name arises from the variability phenomena occurring from structured magnetic fields emerging from the convective envelope of stars. For example, flares and large-scale photometric variability from stellar surface features (stellar spots or faculae). The strength of the magnetic field can be directly or indirectly measured in several ways, and a star's photometric variance varies with the magnetic field's strength. Here we will discuss three indicators of a star's magnetic field: the elemental magnetic activity through $\log R_{\text{H,K}}^+$ and S , the photometric variability range (R_{per}) and the fractional spot coverage of a star (f_{spot}).

One of the most frequently probed indicators of chromospheric activity, and thus magnetic field strength, in low-mass magnetically active stars is the non-thermal flux reversal in the cores of the Ca II H and K lines at 3968 Å and 3933 Å respectively. Two measures of the chromospheric Ca II *H* and *K* line fluxes are generally adopted. The first is through the classical S index. This is the flux ratio in the core of the Ca II *H* and *K* lines to close by continuous windows

$$S = \alpha \frac{H+K}{R+V}, \quad (\text{A.1})$$

where H and K are the line fluxes measured in 1.09 Å wide triangular bandpasses while R and V are estimates of the continuum on either side of the lines measured in 20 Å wide spectral windows centred on 3901 Å and 4001 Å. α is a normalisation constant dependent on the telescope used to make the measurements, providing a link between samples. The quantity S is sensitive to the integrated emission over these windows and the photospheric radiation transmitted in the *H* and *K* passbands. S is, therefore, evolutionary and metallicity dependent, which renders direct comparison of S between different spectral type stars unsuitable. The quantity $\log R_{\text{H,K}}^+$, on the other hand, eliminates this contribution (see, e.g. [Lorenzo-Oliveira, Diego et al., 2018](#)) and is thus a more reliable measure of the chromospheric Ca II *H* and *K* flux.

Another indirect measure of the magnetic field's strength arises from the star's photometric variability. Here we differentiate between the large-scale photometric variability of a star during a magnetic activity cycle, where the average stellar flux of a star increases and decreases on the timescale of years and the variability range of a star due to stellar spots on a rotational time scale. The solar integrated Ca II index, S , correlates linearly with photospheric star-spot number. [Lorenzo-Oliveira et al. \(2016\)](#); [Lorenzo-Oliveira, Diego et al. \(2018\)](#) established a relationship between solar chromospheric activity and the number of spots on the surface for solar-like stars, suggesting that the two are interconnected. However, whether this correlation is strong enough to derive long-term chromospheric activity cycles similar to photometric cycles on magnetic activity timescales (years) is uncertain. The consistently similar periods of the two relations suggest the two are interconnected, with the faculae or star spot dominance of the magnetic photometric cycles being derived from the expected relation between the two. A

star that expresses a larger number of stellar spots will have a more significant photometric variability as it rotates.

Photometric variability is generally measured through the quantity R_{per} . R_{per} is defined as the median of the range between the 5th and 95th percentile of normalised flux in bins of the light-curve divided into sections of the length of the measured rotational period (McQuillan et al., 2014). Larger R_{per} stars are expected to have more easily detectable rotation periods because the larger the star’s variability as it rotates, the more easily distinguishable this variability is from noise.

Finally, the most recent measure of stellar activity has arisen from the measurement of the fractional spot coverage of stars (See Chapter 3 and Cao & Pinsonneault (2022)). They found that fitting *APOGEE*spectra with two temperature components allows one to infer the surface fractional spot coverage and the temperature contrast of the spots to the ambient surroundings. The fractional stellar spot coverage of a stars is expected to be tied to the photometric variability of those stars with larger photometric variability arising from a larger fractional spot coverage.

All of these measurements of magnetic activity have been shown to be related to each other and follow similar relations with the stellar Rossby number. Magnetic activity indicators saturate below a $R_o < 0.3$ (Cao & Pinsonneault, 2022) (fast rotation) and decrease with a power law as R_o increases. This relation reflects the decreased probability of observing older slow-rotating stars in the McQuillan et al. (2014) sample. Variations in magnetic activity can therefore indicate variations to the expression of stellar spots and, thus, the observability of stellar rotation.

The magnetic activity also varies with the stellar magnetic cycle of a star, with some scatter to magnetic activity indicators being attributed to this. Therefore, a single temporal measurement of magnetic activity must be treated with care. Variations to the magnetic activity of stars, in a population-wide sense, should be found by the average magnetic activity of a subpopulation. We adopt a population study approach to minimise this effect in this work.

This Appendix will be structured as follows. In Section A.2, we introduce our method to determine where minima in photometric variability occur and reconfirm that the gap aligns with minima in the photometric variability range. Using this method, in Section A.3, we show that this minima also aligns with minima in $\log R_{\text{HK}}^+$. Following this, in Section A.4, we then show that the sample of stars with undetected rotation does not contain a subsample of stars with magnetic activity low enough to fall below the rotation-detection threshold. Then, in Section A.5, we argue that the number of stars required for the dearth of observations to no longer be considered a dearth requires a larger number of stars than the number of stars within the undetected sample. In Sections A.6 and A.7, we summarise and discuss the implications of our work on proposed mechanisms to explain the intermediate period gap.

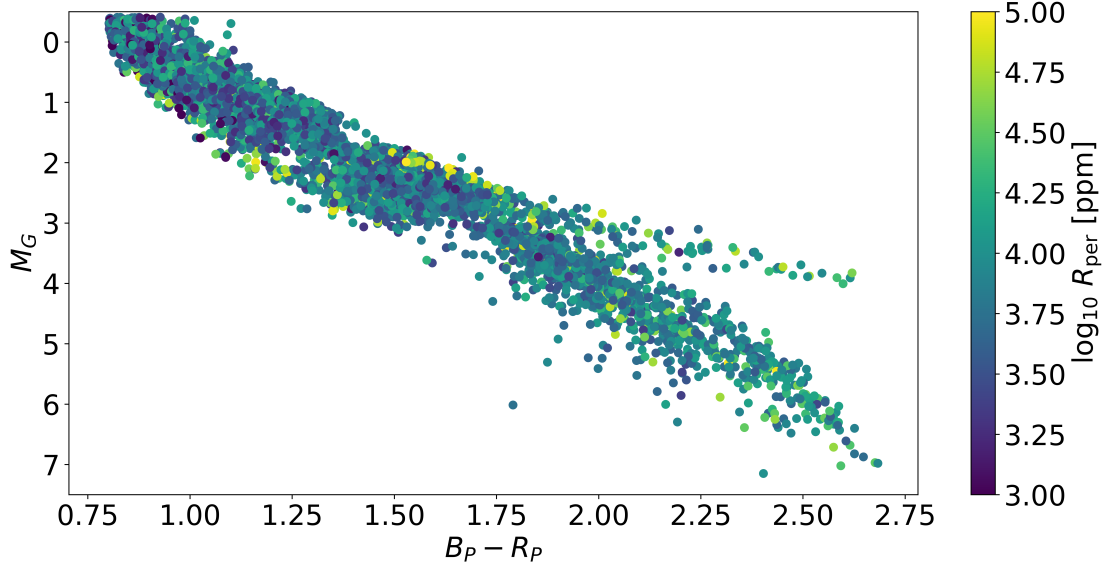


FIGURE A.1: Colour-magnitude diagram of the closeby rotating main-sequence sample colours by photometric variability (R_{per}).

A.2 The gap aligns with a minima in photometric variability

The first mechanism we consider is that the rotation period gap reflects a decrease in photometric variability due to a variation in the magnetic field strength of stars near the gap. We will begin with the 33,000 stars with rotation periods from [McQuillan et al. \(2014\)](#). While this sample has been superseded by other missions in terms of sensitivity, the increase in sensitivity has *not* increased the number of detected rotation periods of cooler stars, particularly where the gap is most apparent. In terms of number of stars, it is still the state-of-the-art mission for precise measurement of the rotation periods of low-mass stars near the intermediate period gap. All stars in this sample lay within the crossmatch with *Gaia* data release 3, which contains precise measurements of the $B_P - R_P$ colour, G -band magnitude and distance from parallax. We limit our sample to stars within the nearest 525pc, to avoid selection effects and inaccurate measurement of rotation periods of stars beyond this distance. This reduces the sample to 8,594 stars. We made cuts in *Gaia* DR3 magnitudes and colours using $M_G \geq 0$ and $B_P - R_P \geq 0.8$ to target below the main-sequence turnoff and star's lower mass than the Kraft break ([Kraft, 1967](#)). This leaves us with a sample of 6,243 nearby stars with reliable surface rotation and colour measurements. These measurements are shown in Figures A.1 and A.2, where we have plotted them as a colour-magnitude diagram and log rotation period against *Gaia* $B_P - R_P$ colour, what we will refer to as the rotational period distribution from in this work. In Figure A.2 we have also coloured the measurements by the log of R_{per} , which exhibits the decrease in photometric variability surrounding the gap.

From this sample, we can describe the average evolution of photometric variability around the intermediate period gap. We will first separate the subsample into bins of $B_P - R_P$ (colour) from

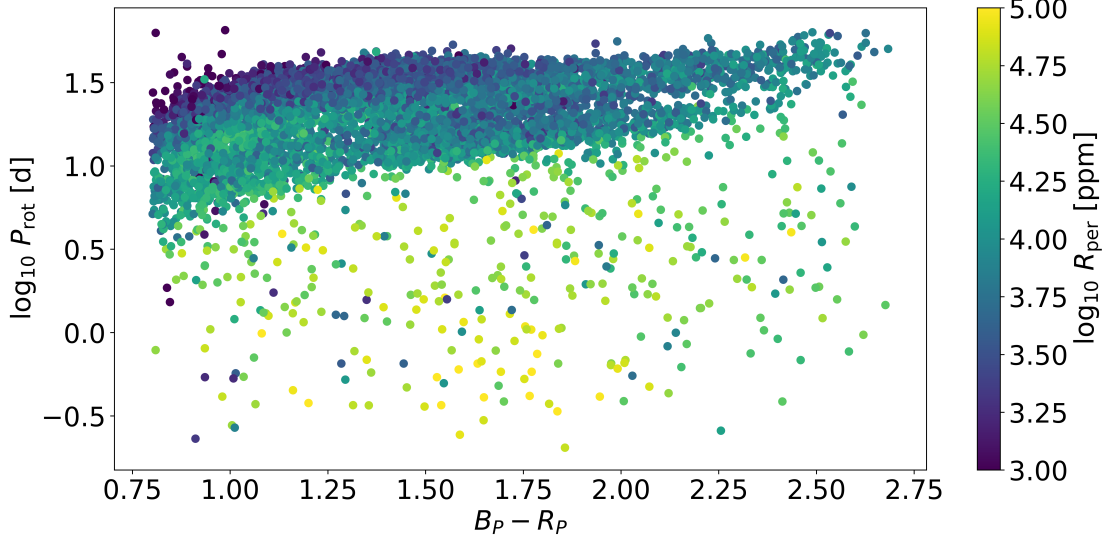


FIGURE A.2: \log_{10} of the rotation period against *Gaia DR3* $B_P - R_P$ colour of the closeby rotating main-sequence sample colours by photometric variability (R_{per}). In this figure, we can see observe the decrease in the photometric variability of stars near the gap.

0.8–2.5 of size 0.17 (10 bins). In each colour interval, we then split the data into the logarithm of rotational period intervals of width 0.07 dex between 0.4 and 1.8 dex, which correspond to 2.5 and 70 days, respectively. We then compute the median and median absolute deviation of R_{per} in each colour and rotational period bin. The median is used here to attempt to alleviate the effect of activity cycles on the variance of the magnetic activity, and the median absolute deviation establishes the scatter on the measured photometric variability: regions with large median absolute deviation should be treated as less reliable measurements. We neglected the regions with few stars (<5). This removes the spurious stars that have not ascended onto the lower prong of the intermediate period gap, which does not indicate large-scale trends in the data. We reconfirm that R_{per} tends to increase with mass, decrease with the rotational period, and decrease towards the rotational period gap (Reinhold & Hekker, 2020; Basri & Nguyen, 2018; Santos et al., 2021). Comparing Figures A.2 and A.3, we also confirm that the gap aligns itself with a minima in R_{per} .

As a result of the large-scale variability with stellar mass and rotational period, the position of the minima becomes harder to notice as $B_P - R_P$ approaches 0.8. We plot the same data in Figure A.4 to make the minima more prominent. We show the median R_{per} (scatter points) and scatter (errorbars) against the \log_{10} of the rotation period for each colour range indicated in brackets – here, the colour of the interval increases down the plot – as well as fitted cubic spline to the data (dashed). From the cubic spline, we can use the first and second derivatives of the spline to accurately determine the position of the local minima in R_{per} , which is indicated by the solid vertical blue line.

The calculation of the position of the minima is an automated process. To identify minima, we

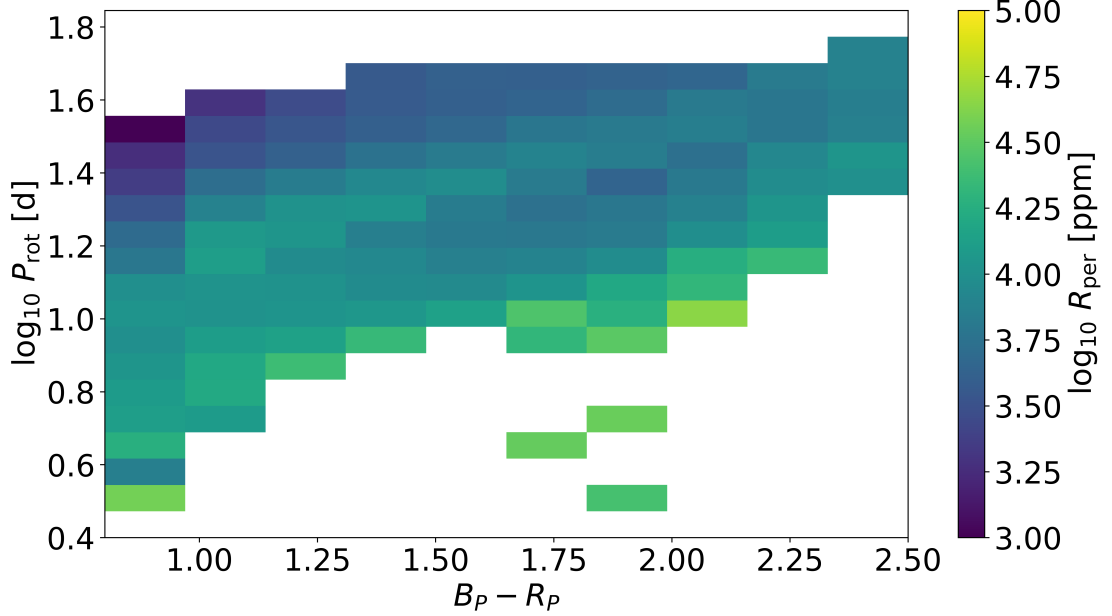


FIGURE A.3: 2D binned photometric variability (R_{per}) for the slices of \log_{10} of the rotation period and colour $Gaia B_P - R_P$ used in this work. Comparing this Figure and A.2, the alignment of the minima of photometric variability and observation of stars in the gap can be seen.

calculate the first and second derivatives of the cubic spline fit and find where the first derivative is close to zero and where the second derivative is greater than 5 to ensure we ignore any spurious jitter in the spline fit. We use an automated process to ensure we have not selected a position that we believe aligns with the intermediate period gap. We found that the resulting position of minima can vary slightly depending on the smoothing of the cubic spline and the threshold value chosen for the second derivative. However, the found minima here tended to be robust to variations of the smoothing at that threshold. The first minima, in regards to the rotational period, in the $B_P - R_P = (0.8-0.97)$ bin was also manually ignored.

The position of the minima are shown in blue in Figure A.5, where it is clear that the majority of minima align with the intermediate period gap. We note that the minima do not accurately predict the position of the intermediate period gap for $B_P - R_P \geq 2.16$. We believe this is because of the small number of stars below the gap in this colour range which were cut due to them not containing enough stars. With larger numbers of observations of low-mass stars below the gap we believe our prediction of the position of the rotation period gap with R_{per} would be more accurate in this regime. We also note that the average photometric modulation amplitude tends to peak to a maximum with a larger R_{per} than stars on the lower prong of the rotational period gap despite having longer rotation periods. Whether this peak is indicative of stronger photometric activity suddenly above the gap or of suppression of photometric activity below the gap is unknown.

A possible explanation for the decrease in median photometric variability comes from the nature

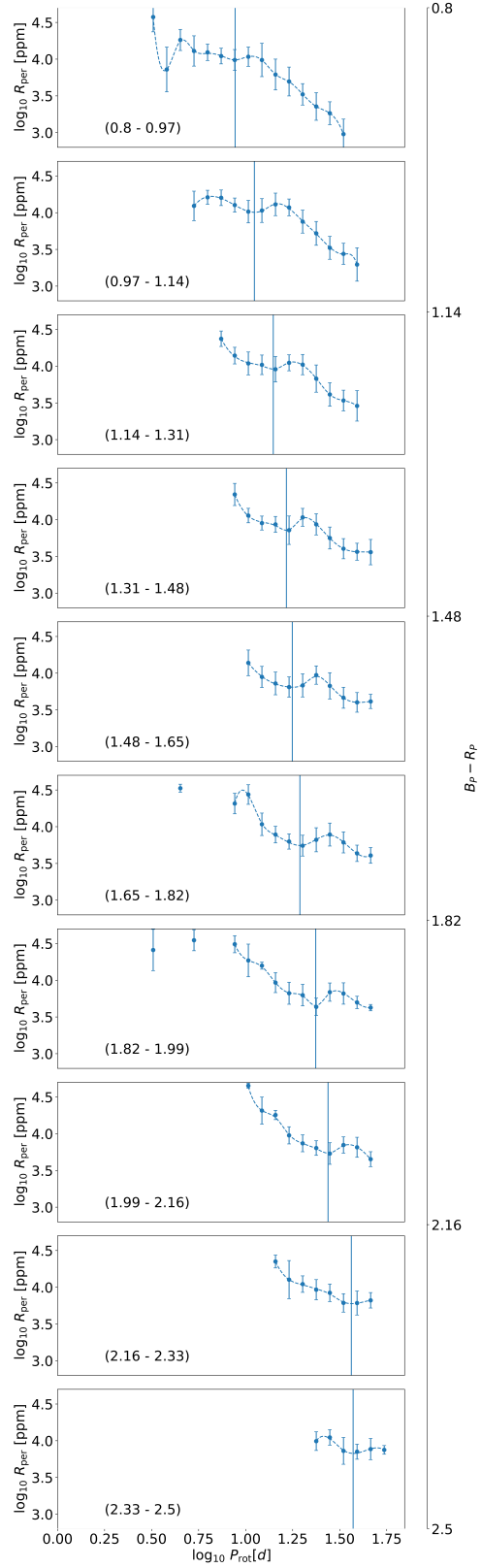


FIGURE A.4: Median and median absolute deviation of photometric variability (R_{per}) against \log_{10} of the rotation period in bins of and colour $Gaia B_P - R_P$ (indicated in brackets). Here we have fitted a cubic spline to median R_{per} and calculated minima using the first and second derivatives of the fitted cubic spline. Solid vertical blue lines show the minima here. These minima align with the rotational period gap.

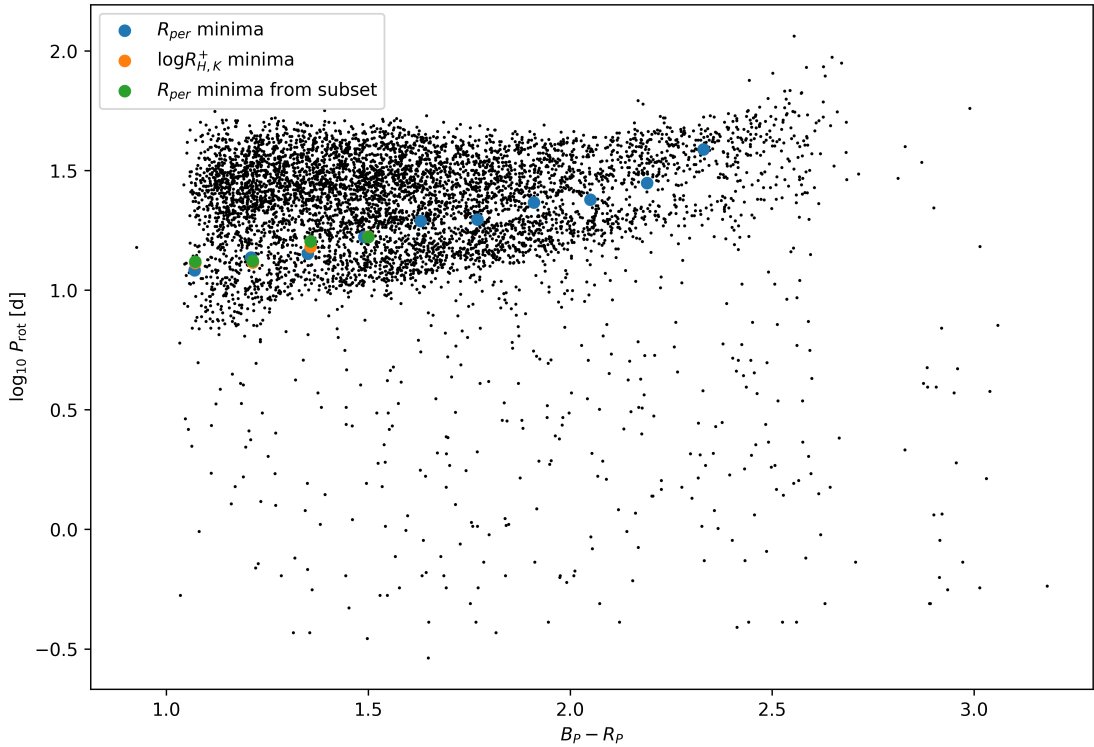


FIGURE A.5: The position of the identified minima in R_{per} against rotational period using the full close-by rotating main-sequence *Kepler* sample, the R_{per} minima identified with the *LAMOST* crossmatch and the $\log_{10} R_{H,K}^+$ minima identified with the *Kepler-LAMOST* crossmatch.

of a dearth of observations, as the gap is not horizontally aligned and increases in period for stars of lower mass (higher $B_P - R_P$). R_{per} generally decreases with mass and rotation period. Taking the median value in slices of constant rotation period near the dearth of observations will be systematically biased in different ways as it passes through the dearth. In order of increasing rotation period, a sample of stars in each bin of rotation period will contain initially, majority fast rotating but redder stars and a small number of slow-rotating bluer stars, then approximately equal fast-rotating red stars and slow-rotating blue stars, and finally majority slow-rotating bluer stars and a small number of fast-rotating redder stars. The relationship between the R_{per} and mass or rotation period are not easily parameterised, especially near the gap. However, we can confirm that this effect does not skew our results by calculating the median and median absolute deviation of $B_P - R_P$ in each colour and rotational period bin. We have shown this in Figure A.6. We confirm that the minima and maxima of R_{per} with rotation period in each colour bin do not correspond to minima or maxima in colour that would indicate that this effect is at play. The variation in R_{per} is, therefore, a physical effect that aligns itself with the rotational period gap.

At first glance, the minima in R_{per} surrounding the gap suggests that the rotation period gap is the result of the decreased probability of observing stars at the given rotation period. However, the minima values of R_{per} within the gap can otherwise be detected for other colour stars. For example, the minima in the $B_P - R_P - (0.97-1.14)$ slice has a R_{per} value of ~ 4.0 , which can

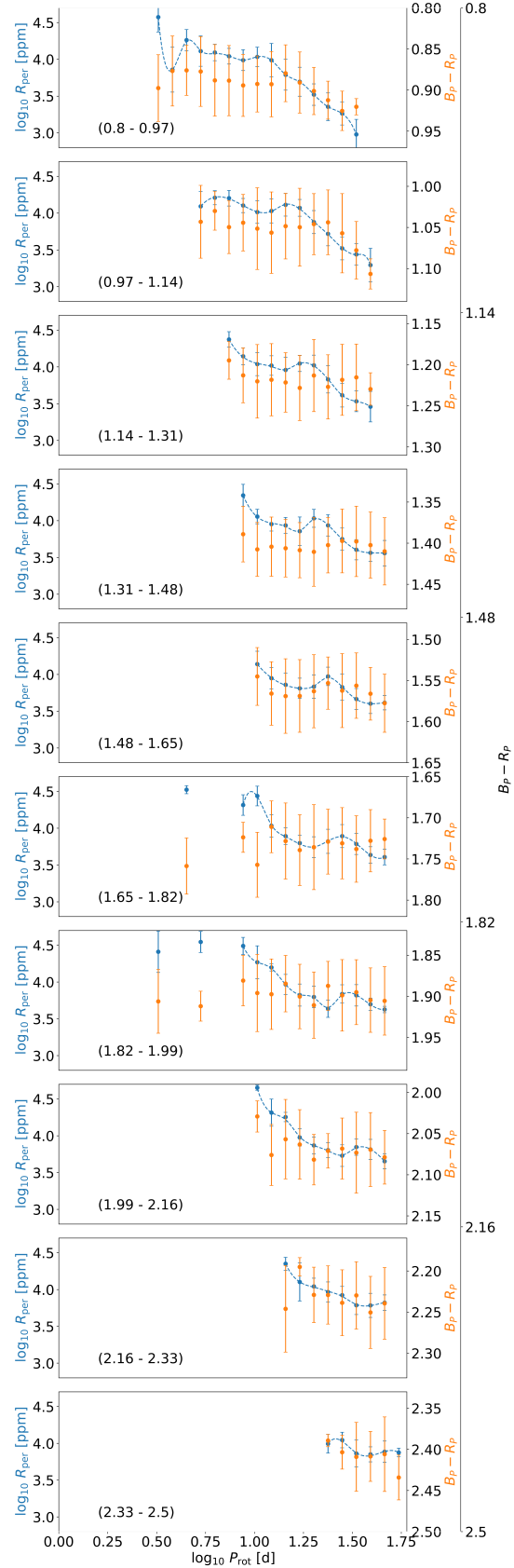


FIGURE A.6: Median and median absolute deviation of photometric variability (R_{per}) (blue) and $B_P - R_P$ (orange) against \log_{10} of the rotation period in bins of and *Gaia* $B_P - R_P$ colour (indicated in brackets). The position of the minima in R_{per} do not align with maxima or minima in $B_P - R_P$ implying that the colour bias when fitting across the dearth can be the cause of the R_{per} minima.

otherwise be easily detected for slower rotating or redder stars. This either suggests that the periodic variability drops suddenly to levels where rotation is not measurable at the rotation period gap or that the rotational variability drops due to the process by which stars cross the gap. [Santos et al. \(2021\)](#) increased the sensitivity of period detection for *Kepler* lightcurves and did not increase the number of stars observed near the intermediate period gap suggesting that the drop in photometric variability does not result in a decreased probability of observing stars near the gap. This implies that if the drop in photometric variability is not the cause for the dearth of observations near the rotational period gap and rather that the drop in photometric variability is purely coincident with the rotational period gap - suggesting that the mechanism underlying the two observations is the same. R_{per} is not defined for stars where rotation is not detected - as R_{per} is defined by the photometric variability range over a rotational period timescale. Therefore we do not know whether the potential stars that lay within the gap, which we cannot observe because of the supposed dramatic decrease in R_{per} , do or do not suddenly decrease in R_{per} .

A.3 The gap aligns with a minima in $\log R_{HK}^+$

While it has been well established that the photometric variability of stars decreases towards the intermediate period gap, other magnetic activity indicators have not been explored in this regard, only the large-scale trends with stellar mass and rotation ([Zhang et al., 2020](#)). Suppose other magnetic activity indicators vary in the same fashion as R_{per} - decreasing to a minimum at the rotational period gap. In that case, it is more likely that the decrease in R_{per} towards the gap results from a variation in the magnetic field of stars.

[Zhang et al. \(2020\)](#) extracted the chromospheric magnetic activity indexes, S and $\log R_{HK}^+$, for 59,816 stars from low-resolution *LAMOST* spectra in the *Kepler-LAMOST* crossmatch. The crossmatch of their work with the nearby rotating main-sequence we established yielded 1060 stars. The stars in the crossmatch tend to be the higher mass, brighter stars with $B_P - R_P < 1.8$, where the intermediate period gap is less apparent. Given that we could predict the gap position for these stars in our earlier experiment, we carry forward and re-analyse their data under a new framework.

$\log R_{HK}^+$ provides a more accurate measure of the chromospheric magnetic activity than S so we adopt $\log R_{HK}^+$ in this work. The resulting rotational distribution of stars is shown in Figure A.7 coloured by $\log R_{HK}^+$.

We adopt the same process as we described earlier to find the minima in R_{per} in a bin of colour against the rotational period. We again separate the stars into the same slices of $B_P - R_P$ and \log of rotation period, and remove any bins containing small numbers of stars (< 2). This cut-off was chosen because of the reduced number of stars in the sample *Kepler-LAMOST* crossmatch,

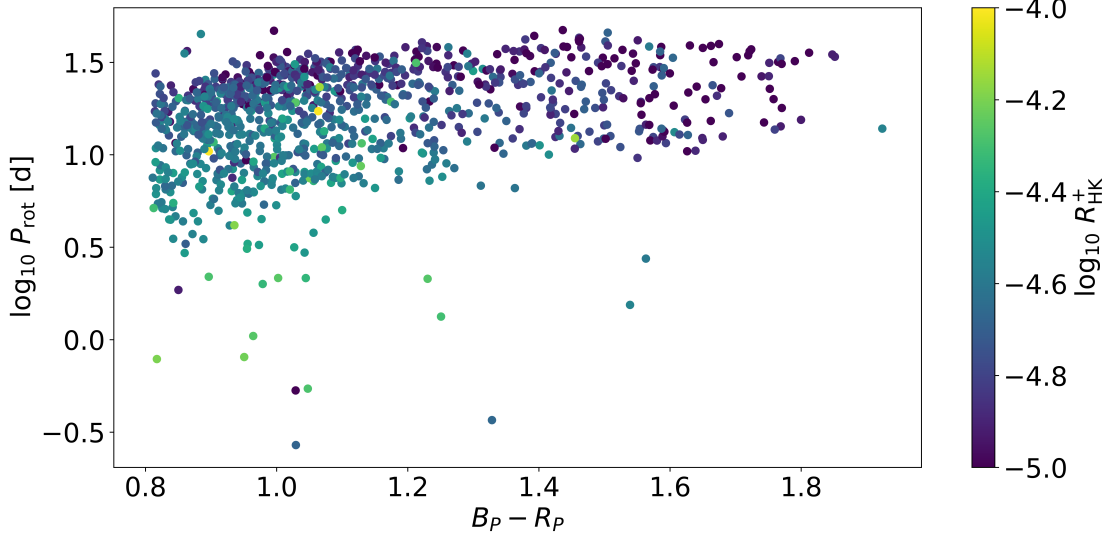


FIGURE A.7: The *LAMOST* chromospherically active and *Kepler* rotating closeby, main-sequence cross-match \log_{10} of rotational period $\log_{10} P_{\text{rot}}$ against $Gaia B_P - R_P$ colour coloured by $\log_{10} R_{\text{HK}}^+$. It is unclear from this whether $\log_{10} R_{\text{HK}}^+$ decreases toward the gap like R_{per} .

compared to the [McQuillan et al. \(2014\)](#) sample. Still, the results should be treated with more caution because we rely on small number statistics. The median and median absolute deviation of both $\log R_{\text{HK}}^+$ and R_{per} in these slices was then calculated, which we then fit with cubic splines against the log of the rotation period. We have repeated this method on R_{per} here because we are using a subset of the original stars and to compare the recovered minima from the subset more accurately this also allows us to confirm the accuracy of the fit of our minima in the first test. The minima of the cubic spline fits are then calculated again using the first and second derivatives using the same smoothing and first and second derivative thresholds.

We compare the distributions of R_{per} and $\log R_{\text{HK}}^+$ against the log of rotation period in Figure A.8 and show the found minima in blue and orange solid vertical lines for R_{per} and $\log R_{\text{HK}}^+$ respectively. Like photometric variability, $\log R_{\text{HK}}^+$ tends to decrease with rotational period owing to their relation to the strength of the magnetic field. We find that, generally, R_{per} and $\log R_{\text{HK}}^+$ are directly tied: increases and decreases to the median value with rotational period in one tends to align with a similar response in the other.

We show the comparison of the recovered minima from R_{per} using this subset as well as the minima recovered using $\log R_{\text{HK}}^+$ in Figure A.5. The recovered R_{per} minima using the subset lay on top of the R_{per} minima recovered using the full sample. Interestingly, we may detect previously unreported minima in $\log R_{\text{HK}}^+$ close to the rotation period gap. Excluding the minima recovered in the $B_P - R_P$ - (0.8-0.97) bins, the minima that we recover in $\log R_{\text{HK}}^+$ against logged rotational period are in the same period bin and are close in position to the minima of R_{per} we recover, which we have established aligns with the intermediate period gap. The alignment of

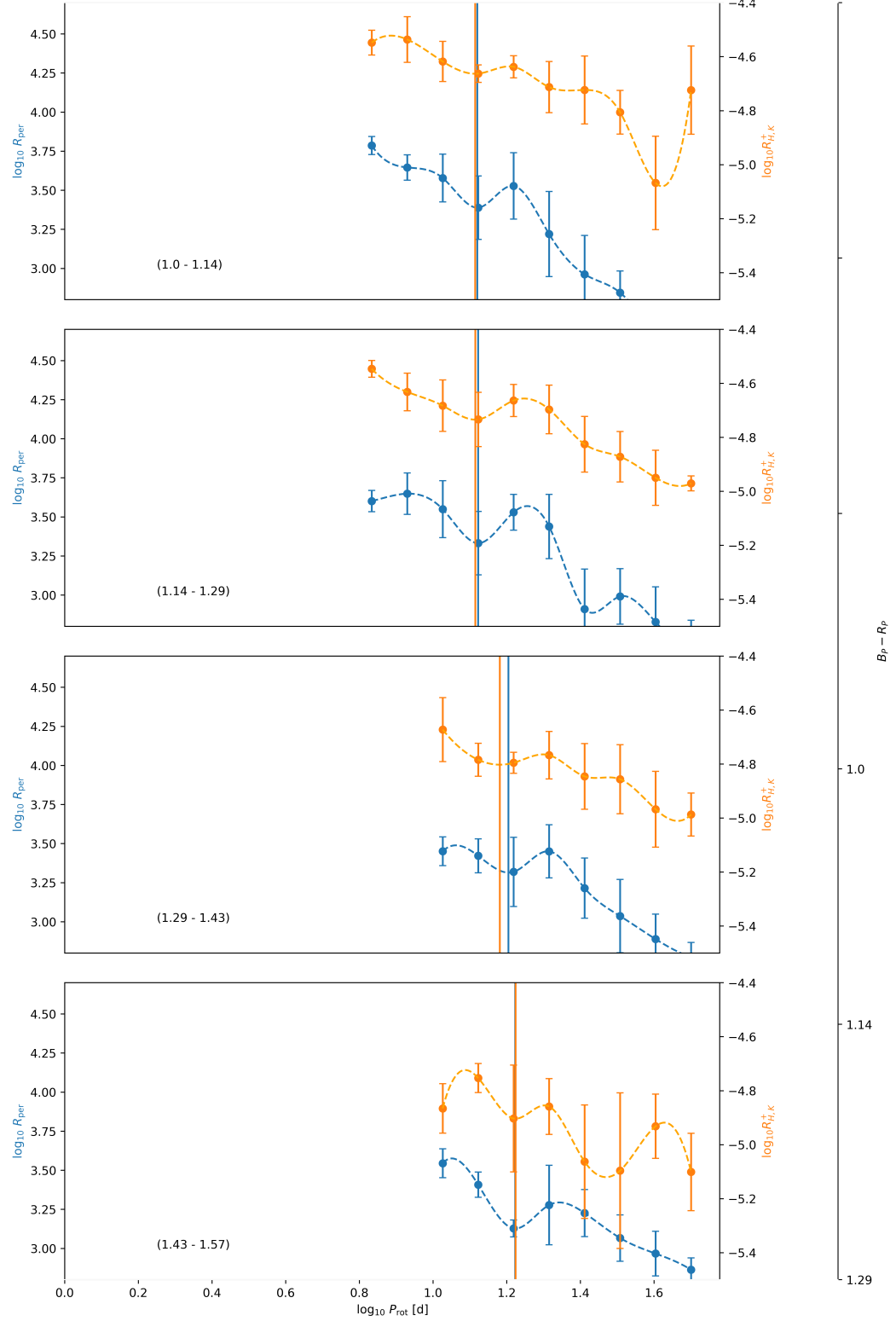


FIGURE A.8: Median and median absolute deviation of photometric variability (R_{per}) (blue) and LAMOST $\log_{10} R_{\text{HK}}^+$ against \log_{10} of the rotation period in bins of colour $Gaia B_P - R_P$ (indicated in brackets). Here we have fitted a cubic spline to the median of these values in each bin and calculated minima using the first and second derivatives of the fitted cubic spline. The minima in R_{per} are shown by solid vertical blue lines, while the minima in $\log_{10} R_{\text{HK}}^+$ are shown in solid vertical orange lines. These minima align with each other and the rotational period gap.

the minima is also robust to variation in the smoothness of the fitted cubic spline - suggesting that the minima are not spurious.

Measurements of $\log R_{HK}^+$ are less precise than R_{per} . The detection of the coincidence in a single slice of $B_P - R_P$ could be explained through this imprecision. Detecting this in multiple slices of $B_P - R_P$ suggests that the cause of the minima is related. We will assume, for now, that the rotational period gap does align itself with minima in both R_{per} and $\log R_{HK}^+$ and explore whether there is a sample of low-magnetic activity, non-detected rotators.

A.4 Is there a sample of low-magnetic activity stars without rotational period detection?

If the gap contains stars that have dramatically low R_{per} and thus do not have detectable rotation periods, then $\log R_{HK}^+$ should also dramatically drop within this regime. If there is a sample of dramatically lower $\log R_{HK}^+$ stars without detected rotation periods, then the existence of such a subsample would support the hypothesis that the intermediate period gap results from a decreased probability of observing stars at those rotation periods due to a decrease in stellar activity.

We will compare the $\log R_{HK}^+$ distributions of the [McQuillan et al. \(2014\)](#) rotating and non-rotating samples. We prepare the sample of 99,000 stars without detected rotation periods from their work² in the same way that we did for the rotating sample ensuring they are close by ($< 525\text{pc}$), on the main-sequence and redder than $B_P - R_P = 0.8$ where the rotational period gap is most apparent. This leaves us with a sample of 5574 non-rotating close by, main-sequence stars, which we can cross match with the *Kepler-LAMOST* sample of chromospheric active stars measured in [Zhang et al. \(2020\)](#) reducing the number of stars to 1134 stars. The number of stars in this sample is similar to that in the rotating sample. We show the resulting HR diagram of stars without rotational detection (bottom) and with rotational detection (top) in Figure A.9 coloured by $\log R_{HK}^+$. Comparing the distributions, it is clear that the non-rotating sample is clearly biased for higher mass stars and does not permeate into the low mass regime, where the gap would be most apparent.

With the rotating and non-rotating *Kepler-LAMOST* samples we can investigate the detectability of rotation as a function of $\log R_{HK}^+$. We expect more magnetically active stars (higher $\log R_{HK}^+$) to be easier to detect in rotation as R_{per} should increase in turn. However, as we have noted earlier in this work, stars can have their rotation go undetected for a multitude of reasons and the non-detection of rotation will not purely be the result of lower magnetic activity.

²This is a slight misnomer as *some* of the stars $\sim 100,000$ stars have detectable rotation periods, but do not pass a detectability threshold, see Section A in the appendix of their work, and those periods should be treated with some care.

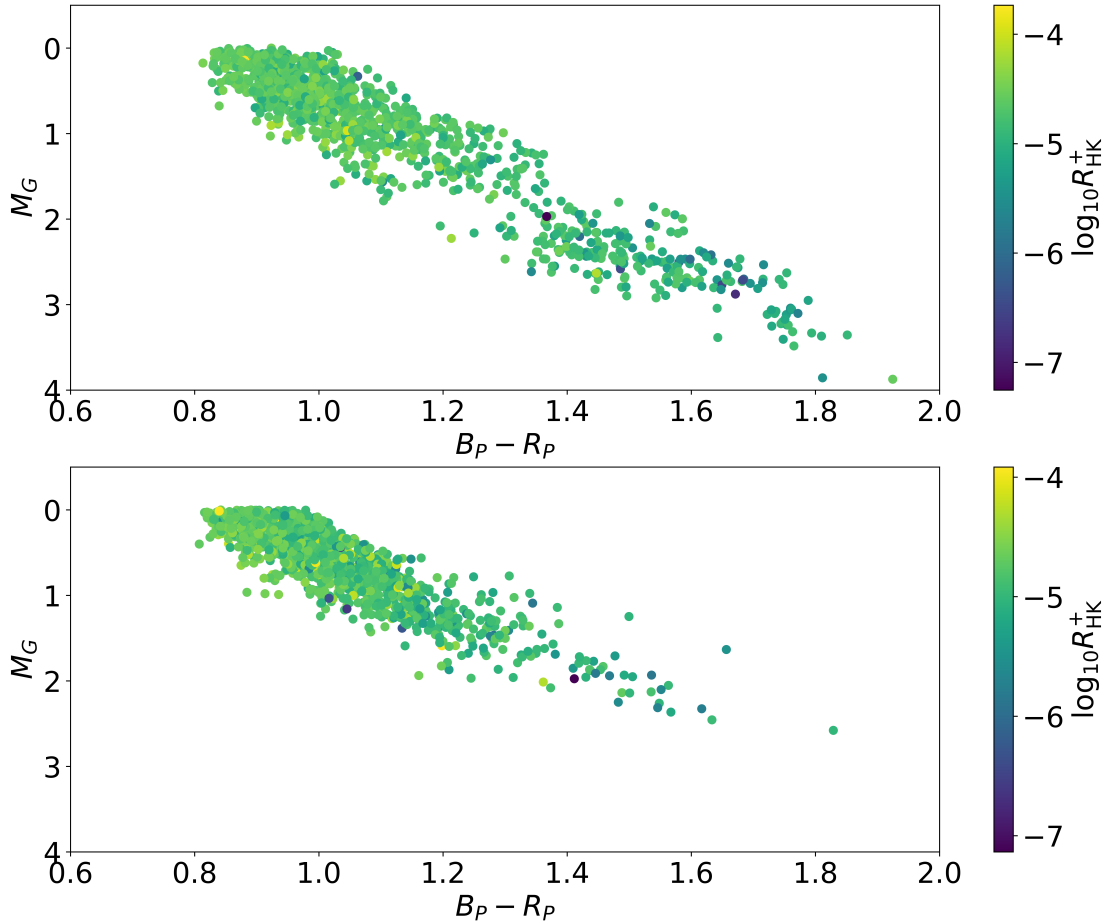


FIGURE A.9: HR diagram of the closeby rotating (top) and non-rotating (bottom) main-sequence sample crossmatched with the *Kepler-LAMOST* field coloured by the chromospheric magnetic activity indicator $\log R_{HK}^+$. Comparing these two samples, we observe very few low-mass stars for which the rotation period is undetected.

Figure A.10 shows the distribution of rotation detected and rotation non-detected samples with $\log R_{HK}^+$. The left panel shows the probability density, while the right shows the cumulative probability density function. Stars detected in rotation appear to have higher $\log R_{HK}^+$ than those without detection. A Kolmogorov-Smirnov (KS) test returns a p -value of $4 \cdot 10^{-15}$. With this, we can reject the null hypothesis that the two samples are drawn from the same underlying distribution with strong statistical significance. The non-rotation detected tends to be less magnetically active, in terms of $\log R_{HK}^+$, than the rotationally detected sample. Less magnetically active stars tend to have a lower detection rate due to the decrease in prominence of stellar spots with lowering magnetic activity.

To investigate the detectability of rotation, let us consider the fraction of targets for which we detected periods in bins of colour and $\log R_{HK}^+$. The detection efficiency here is measured from the ratio of the number of stars with a measured rotation rate to the total number of stars in that bin. Other works (see, e.g., [Claytor et al., 2023](#)) consider the ratio of stars with highly precise rotation period measures to those without. We forgo any cuts to the fractional error on

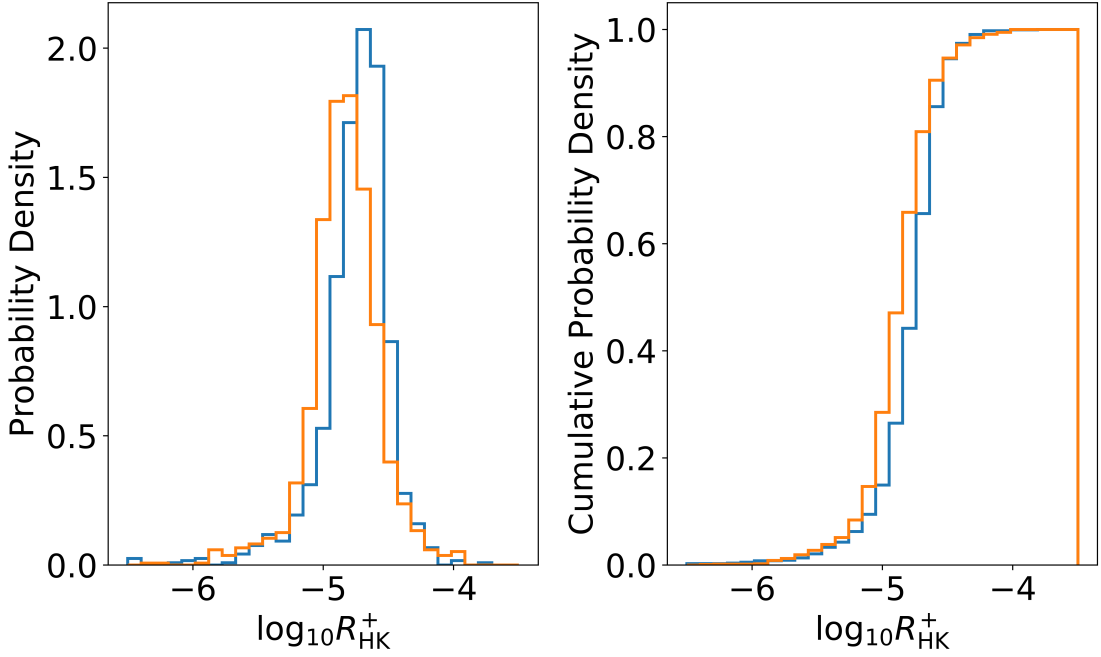


FIGURE A.10: The probability density function (left) and cumulative probability density function (right) of $\log R_{HK}^+$ are separated by whether rotation was or was not detected in the close-by main-sequence Kepler-LAMOST crossmatch. We expect less magnetically active stars to have a lower detection rate due to the decrease in prominence of stellar spots with lowering magnetic activity. This is supported by the data here as the non-rotation detected sample contains a larger number of low $\log R_{HK}^+$ stars.

the rotational period as we have limited our stars to nearby stars, which should have very high precision recovery of the stellar rotation period, and we also make no cuts to the number of stars in each bin that we calculate the histogram for. While limiting the minimum number of stars would allow us to clarify large-scale trends, we are searching for a subsample of stars with spuriously low magnetic activity with an already small sample size.

Figure A.11 shows the detection fraction (top) and a 2D histogram of the non-detected rotation sub-sample (bottom) against colour and $\log R_{HK}^+$. We confirm that rotation is preferentially measured in stars with higher magnetic activity (larger $\log R_{HK}^+$) and tends to increase with colour. Low-mass stars have a high probability of rotation being measured. If we assume that stars of the same $\log R_{HK}^+$ express the same number of stellar spots, then dimmer stars will express larger variability, due to the larger change in relative flux from each spot, and thus will have a higher detectability of rotation. We do not observe an ultra-low magnetic activity population with undetected rotation that would be required to explain the lack of observation of stars in the intermediate period gap. While there are stars with low, for a given colour bin, and ultra low $\log R_{HK}^+ (< 5.5)$ in each $B_P - R_P$ bin, stars in those bins can both be rotationally detected or not rotationally detected. Ultra-low magnetic activity does not indicate their lack of probability of rotational observation, and there is no subsample of ultra-low magnetic activity stars without detected rotation periods. While stars older-slowly rotating stars also tend to have

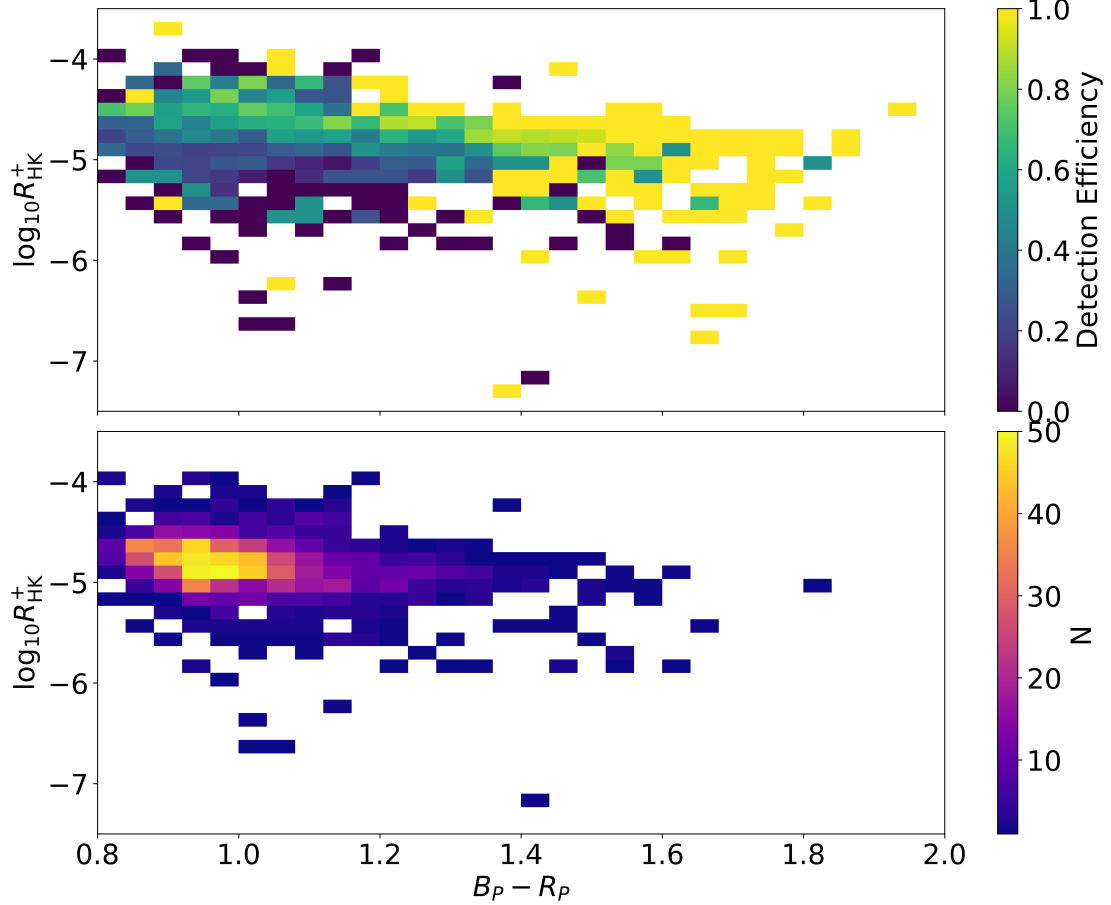


FIGURE A.11: The detectability of rotation (top) and 2D histogram of stars without detected rotation periods (bottom) across $Gaia B_P - R_P$ colour and $\log R_{HK}^+$. Rotation is preferentially measured in stars with higher magnetic activity (larger $\log R_{HK}^+$) and tends to increase with colour. Low-mass stars have a high probability of rotation being measured. Stars with low magnetic activity have a lower likelihood of rotational observation. Bins with detection efficiency equal to zero or one tend to contain single stars, with detected rotation or without detected rotation, respectively and are not indicative of trends in the detection efficiency. We do not observe an ultra-low magnetic activity population with non-detected rotation that would be required to explain the lack of observation of stars in the intermediate period gap. While there are stars with ultra-low $\log R_{HK}^+$ (< 5.5) in each $B_P - R_P$ bin they can either both rotationally detected or not rotationally detected. The ultra-low magnetic activity does not indicate their lack of rotational observation probability.

lower $\log R_{HK}^+$, which may camouflage a population of low $\log R_{HK}^+$ gap stars, they still tend to have observable rotation periods. For the gap to exist the magnetic activity would need to drop to a point where observation of rotation period is impossible, which is not supported by the data here.

A.5 The lack of observation of stars that could fill the intermediate period gap

For the hypothesis that the gap represents a minimum of stellar rotational period detection and that the gap is indeed full of stars, then must be enough stars without detected rotation periods to fill the shortage of observations. In this Section, we will determine whether this is indeed the case.

We will assume that the multiple missions that have observed the rotation period gap (*Kepler*, *K2*, *ZTF*, *TESS*) missions are not biased away from observing stars within the rotation period gap and compare the distribution of stars in the [McQuillan et al. \(2014\)](#) *Kepler* rotating and undetected rotating samples. Further, this analysis will focus on very low-mass stars where the gap is most apparent where [McQuillan et al. \(2014\)](#) remains the state-of-the-art in detecting rotational periods for low-mass stars near the gap. We make no quality cuts to the data to ensure we are not preferentially selecting for stars that could/could not possibly fill the gap.

If we compare the distribution of the number of stars in the rotation detected and undetected samples with colour, as we have shown in Figure A.12, we observe that stars with detectable rotation periods outnumber stars with undetectable rotation periods at lower masses ($B_P - R_P \geq 1.3$), despite the overall 3:1 ratio of the detectable rotation period to undetectable period catalogues. In the inset of this Figure, where we compare the distributions where the gap is most apparent, we see that the proportion of stars with undetectable rotation periods to stars with detectable rotation periods decreases with decreasing mass, to a minimum of 1:10 undetectable to detectable rotation periods at the lowest masses. This suggests that there are not a large number of stars available to fill the rotational period gap.

We will more concretely investigate this by determining how many stars would be required to fill the gap - or rather for the dearth in observations to be undetectable in the low mass range where the proportion of stars between the samples is largest and where the gap is most apparent ($B_P - R_P \geq 1.5$). To find the number of stars required for the dearth of observations to be no longer considered a dearth we first separate the sample with detected rotation into bins of $B_P - R_P$ from 1.5-2.2 of size 0.045 (15 bins). In each colour interval, we then split the data into log rotational period intervals of width 0.07 dex between 1.0 and 1.7 dex (10 bins) which correspond to 10 and 50 days, respectively. We then calculate the number of stars in each slice of log period for a given colour range. In Figure A.13 we show the number of stars in each slice (scatter points) against \log_{10} of the rotation period for each colour range indicated in brackets to which we have fit a cubic spline (dashed). From the cubic spline, we determine the position of the local minima in number of stars with detected rotation period, which is indicated by the solid vertical black line. To calculate the number of stars required for the dearth, we compare the average of the two scatter bins surrounding the closest bin of the minima position. While

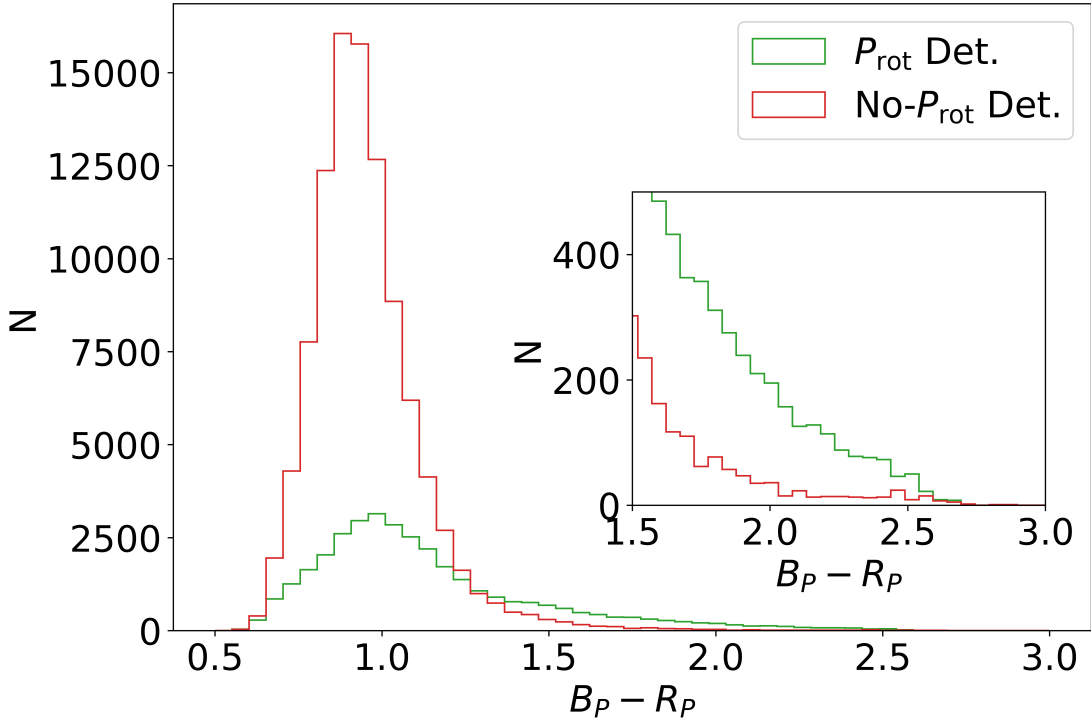


FIGURE A.12: A histogram of the distribution of $B_P - R_P$ colour of stars with (green) and without (red) detected rotation periods. **Inset:** A zoom-in of the distribution for $B_P - R_P \geq 1.5$ where the rotational period gap is most apparent. The distribution in colour of stars with and without detected rotation periods vary. The undetected rotation sample is strongly biased towards stars with $B_P - R_P$ close to 1, comparative to the lower-mass stars where the number of stars drops quickly. Despite the $\sim 3:1$ ratio of the number of stars with undetected rotation periods to those with detected rotation periods, the number of stars without detected rotation periods drops below those with detected rotation at $B_P - R_P \geq 1.3$.

this approach is admittedly naive, as it assumes all of the stars will be in the bin closest to the minima rather than being distributed throughout the dearth region, it places a lower bound on the stars required to fill the gap.

In Figure A.14 we compare the number of stars required to fill the gap to the number of stars without detected rotation periods in each colour range. The number of stars required to fill the gap is approximately constant at $N \sim 20$. This suggests that the number of stars required to fill gap is independent of the total number of stars observed in that mass range. Suppose, then, that the gap is full of stars without detectable rotation periods. In that case, we expect the proportion of stars required to fill the gap to increase proportionate to the total number of stars (detected and non-detected rotation), but this is not the case. The number of stars required to fill the gap is much smaller than the number of stars without detected rotation periods for $B_P - R_P < 1.8$. Still, as colour increases and the number of observed (detected rotation period stars) stars decrease, the number of stars required to fill the gap becomes the majority of stars without detected rotation periods. This suggests that for the gap to be full of stars with undetected rotational period stars, all of the stars in the undetected rotational period sample would need to be in this small rotational

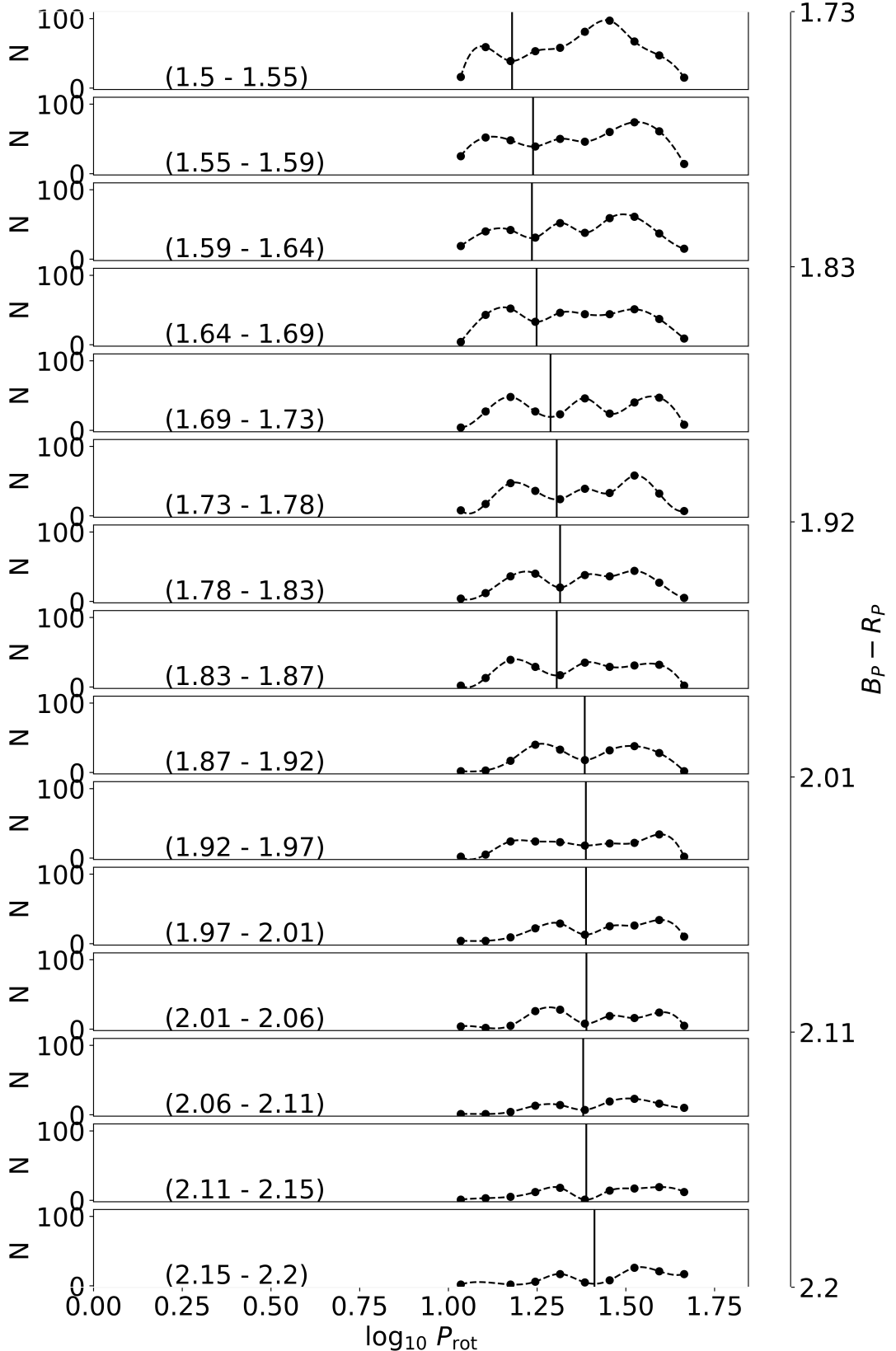


FIGURE A.13: Number of stars in each bin against \log_{10} of the rotation period in bins of colour $Gaia B_P - R_P$ (indicated in brackets). Here we have fitted a cubic spline to the number of stars in each bin and calculated minima using the first and second derivatives of the fitted cubic spline. Solid vertical black lines show the minima in number of stars. These minima are the rotational period gap.

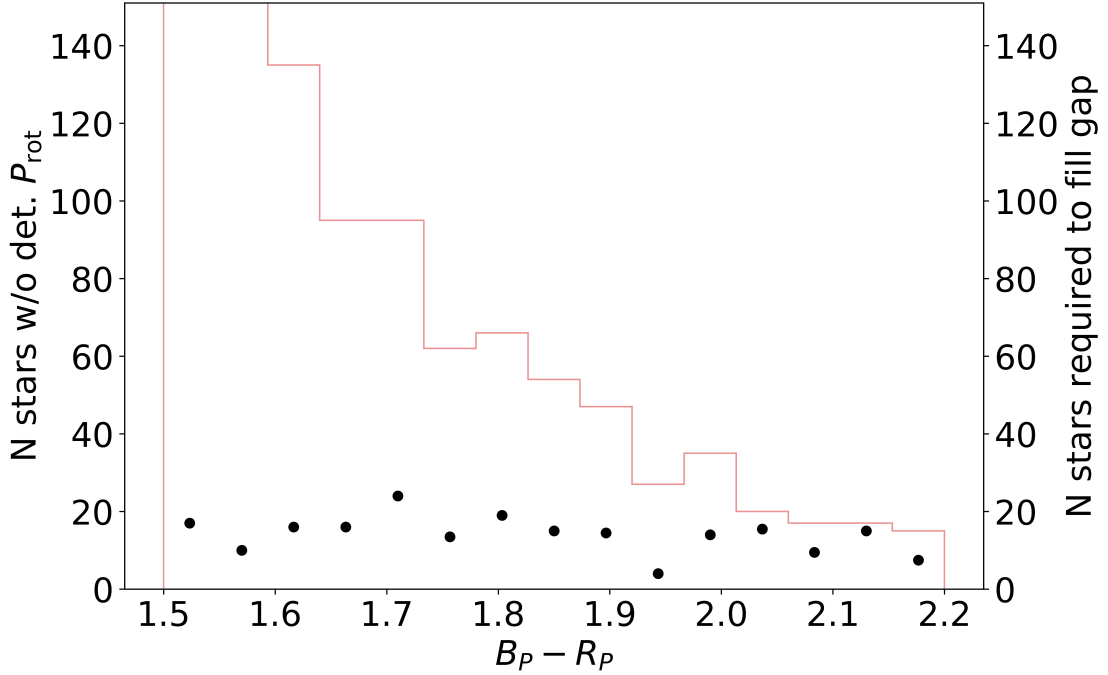


FIGURE A.14: The number of stars required to fill the gap (black scatter points) against the number of stars with undetected rotation periods against $B_P - R_P$. The number of stars required to fill the intermediate period gap is roughly constant at $N \sim 20$. While the number of stars without detected rotation greatly outnumbers the number required to fill the gap below $B_P - R_P \sim 1.8$, the two are almost equal for lower mass stars.

period range, and only a very small number of stars with undetected rotation are the result of noise or inclination effects. The requirement of most (if not all) stars within the undetected rotation period sample suggests that the gap is not full of stars with undetectable rotation.

A.6 Summary and discussion

Through this work we have reconfirmed that the gap aligns with a minima in the photometric variability range (R_{per}). The coincidence of the gap and the minima has been invoked to suggest that the gap results from a very low probability of observing stars within the gap and that the gap is, in fact, full of stars with undetectable rotation periods. The average R_{per} of stars around the gap does not fall below the detectability threshold of rotation and stars with much lower R_{per} have detectable rotation periods can be detected.

One explanation could be that R_{per} drops suddenly below the rotation detectability threshold, for stars precisely within the gap. The exact cause of this drop is unknown. This drop could arise from a decrease in the magnetic activity of stars within the gap, leading to little to no expression of stellar spots or, as Reinhold et al. (2019) suggests, the result of the cancellation brightness variations of spots by faculae. We found in this work that the drop in R_{per} , and thus the gap, is also

coincident with a drop in $\log R_{\text{HK}}^+$ suggesting that the decrease in photometric variability in stars close to the gap is the result of a decrease in magnetic activity, rather than a transition in the spots dominance to faculae dominance. However, we also found that there is not a subsample of stars without rotational period detection but with ultra-low $\log R_{\text{HK}}^+$. While the stars without rotational period detection tend to have lower magnetic activity, there is not an obvious subsample of stars with $\log R_{\text{HK}}^+$ below the rotation period detection threshold. This suggests that there are no stars within the gap with ultra-low magnetic activity that make rotational period observation impossible.

Another possible mechanism we can investigate using this data arises if we consider that stars within the gap may have magnetic activity so great that noise dominates their light curves making observation of their rotation impossible. Rotation tends to be less readily detectable at high activity when the light curve is noisy from the stochastic production of a larger number of surface features. Consider a scenario whereby the average magnetic activity of stars increases in the region of evolution around the magnetic activity gap. Indeed, the magnetic activity of stars tends to decrease with rotation rate, but we will ignore this for now. Let us assume instead that the spot-faculae cancellation does not occur and that brightness variations on a magnetic activity timescale are spot dominated below the Vaughn-Preston Gap³. Conceivably, as the average magnetic activity increases for stars near the gap, the regions where noise is minimal enough for rotation to be detected become smaller and more concentrated to times when the magnetic activity of stars is very small, which must constitute a minority of stars for a given $B_P - R_P$ and rotational period. This would coincide with a decrease in R_{per} of stars as average magnetic activity increases. The gap would then represent a region of evolution where the average magnetic activity of stars would be large enough that the noise permeates the entire magnetic activity cycle, and no rotation observations could be made. Observations of rotation period should therefore be more likely to occur when a star is minimally active and thus has the smallest observed magnetic activity- which would also correspond to a minima in observed $\log R_{\text{HK}}^+$. This would suggest that there is a population of magnetically active stars with $\log R_{\text{HK}}^+$ greater than the average magnetic activity of stars near the gap that have otherwise undetectable rotation periods. In Figure A.11, we show that there is not a subsample low rotation detectability stars with $\log R_{\text{HK}}^+$ greater than the average of stars near the rotational period gap, suggesting that this selection mechanism is not at play.

The proposition that the rotational period gap represents a minimum of detectability of stars is not favoured by the data. The coincidence of the minima in R_{per} with minima in $\log R_{\text{HK}}^+$ along with the lack of a population of low or high $\log R_{\text{HK}}^+$ stars with low detectability suggests that minima in R_{per} cannot be explained by a spot-faculae transition nor a selection effect for stars with low or high magnetic activity near the rotational period gap. Furthermore, we found that

³A distinct gap from the intermediate period gap wherein the transition from spot dominance to faculae dominance occurs in their work

for the gap to be explained by a lack of detection of the rotational period, stars within the gap must make up most stars in the *Kepler* non-detected rotational period sample. This explanation is unlikely due to the many factors by which rotation is not observed for all stars: inclination effects, noise drowning the rotational period signal etc. Recent works have also tentatively shown that the kinematic ages of stars above and below the rotation period gap have comparable kinematic ages (Lu et al., 2022) which suggests that there is no missing sample of stars that fill the gap.

The only alternative mechanism that has been proposed in the literature is the onset of strong surface angular momentum loss whereby stars “jump” the gap. However, this explanation does not have a proposed physical mechanism. As stars evolve toward the gap, their core and envelope undergo recoupling, slowing their spin-down. Cao et al. (2023) suggest that the process of core-envelope recoupling with significant angular momentum flux (See Section 4. of their work) between the core and the surface enhances the magnetic dynamo of stars, inducing larger photometric variability from greater spot coverage. The decrease in photometric variability towards the gap can be explained under this framework if the enhancement of the magnetic dynamo is dependent on the scale of the radial shear between the core and the surface, which decreases towards the gap if the core and envelope have completely recoupled.

Two mechanisms could then be invoked to explain the sudden enhanced spin-down: core-envelope re-decoupling or enhanced magnetic spin-down. Conceivably the core and the surface of the star can again decouple at the rotational period gap; the surface spins down at a much faster rate than below the gap resulting in the apparent dearth of observations. It is, however, not clear the effect that this decoupling would have above the gap. If the core and envelope are strongly decoupled above the gap then angular momentum transport between the core and surface is likely to reoccur, supported by the relatively flat radial differential rotation profile observed for the Sun and young subgiants (Deheuvels et al., 2015). R_{per} of stars just above the gap is similar to stars below the gap, suggesting that they do not have enhanced dynamos consistent with the strong radial shears. R_{per} increases with rotation period above the gap, suggesting instead that the enhancement of the dynamo by core-envelope should grow as the star evolves. For this to be the case the core-surface radial shear must grow and the core and surface must remain decoupled until recoupling enhances the magnetic dynamo. However, the gap is only apparent for a small rotational period range and the density of stars with observed rotation periods above and below the gap are consistent - suggesting that the decoupling is not slowly counteracted by core-envelope recoupling resulting in the enhanced R_{per} away from the gap.

Enhanced magnetic angular momentum loss is another possible explanation for the gap. The magnetic braking of a star is dependent on the rotation rate, mass loss rate and the strength of the magnetic field. Stars near and just above the gap are rotating slower and have smaller magnetic activity indicators than stars below the gap. Further, we found that stars just above the

gap do not show significant enhancement in $\log R_{\text{HK}}^+$. If the sudden increase in magnetic braking arises from enhancement to the magnetic field, it is not reflected in the magnetic activity of stars near the gap. The only other variable to consider here is increased mass loss. While mass loss rates of main-sequence stars are an ongoing field of research, to reflect the change in rotation period of stars passing through the gap, we speculate that the mass loss rate would need to be enhanced by several orders of magnitude compared to the observed mass loss rate of the Sun. That significant mass loss is not reflected in any other measurements of stars surrounding the gap, nor is there a known mechanism by which the enhanced mass loss would occur. As a result, currently, there is no known mechanism for said enhanced magnetic braking to arise.

A.7 Conclusion

In this work we have proposed that the data does not support the two leading explanations for the intermediate period gap: a sudden decrease in probability of rotational period detection or the sudden onset magnetic braking. While further work is required to definitively rule out their involvement in the intermediate period gap, we use this as motivation to propose a novel explanation for the intermediate period gap: the sudden onset of latitudinal differential rotation and the impact that has on the observed rotational periods of stars.

We thank Jing Hua Zhang for providing us with the magnetic activity indicators $\log R_{\text{HK}}^+$ and S values of the non-rotating sample of the *Kepler-LAMOST* crossmatch in their work [Zhang et al. \(2020\)](#) that made sections of this work possible.

Bibliography

- Aerts C., Christensen-Dalsgaard J., Kurtz D. W., 2010, *Asteroseismology*. Springer
- Affer L., Micela G., Favata F., Flaccomio E., Bouvier J., 2013, *Monthly Notices of the Royal Astronomical Society*, 430, 1433
- Agüeros M. A., et al., 2018, *The Astrophysical Journal*, 862, 33
- Ahlborn F., Bellinger E. P., Hekker S., Basu S., Angelou G. C., 2020, *Astronomy & Astrophysics*, 639, A98
- Aigrain S., et al., 2008, *Astronomy & Astrophysics*, 488, L43
- Aigrain S., et al., 2015, *Monthly Notices of the Royal Astronomical Society*, 450, 3211
- Akeson R., et al., 2019, arXiv e-prints, p. arxiv:1902.05569
- Albrecht S., Winn J. N., Carter J. A., Snellen I. A. G., de Mooij E. J. W., 2011, *The Astrophysical Journal*, 726, 68
- Albrecht S., Setiawan J., Torres G., Fabrycky D. C., Winn J. N., 2013, *The Astrophysical Journal*, 767, 32
- Amard L., Palacios A., Charbonnel C., Gallet F., Bouvier J., 2016, *Astronomy & Astrophysics*, 587, A105
- Amard L., Palacios A., Charbonnel C., Gallet F., Georgy C., Lagarde N., Siess L., 2019, *Astronomy & Astrophysics*, 631, A77
- Amard L., Roquette J., Matt S. P., 2020, *Monthly Notices of the Royal Astronomical Society*, 499, 3481
- Anders F., et al., 2016, *Astronomische Nachrichten*, 337, 926
- Angus R., Morton T., Aigrain S., Foreman-Mackey D., Rajpaul V., 2017, *Monthly Notices of the Royal Astronomical Society*, 474, 2094
- Angus R., et al., 2020, *The Astronomical Journal*, 160, 90

- Arlt R., Hollerbach R., Rüdiger G., 2003, *Astronomy & Astrophysics*, 401, 1087
- Augustson K. C., Brun A. S., Toomre J., 2019, *The Astrophysical Journal*, 876, 83
- Avallone E. A., et al., 2022, *The Astrophysical Journal*, 930, 7
- Baglin A., 2003, *Advances in Space Research*, 31, 345
- Balbus S., Hawley J., 1994, *Monthly Notices of the Royal Astronomical Society*, 266
- Ball W. H., Gizon L., 2014, *Astronomy & Astrophysics*, 568, A123
- Ball W. H., Gizon L., 2017, *Astronomy & Astrophysics*, 600, A128
- Barker A. J., Jones C. A., Tobias S. M., 2019, *Monthly Notices of the Royal Astronomical Society*, 487, 1777
- Barker A. J., Jones C. A., Tobias S. M., 2020, *Monthly Notices of the Royal Astronomical Society*, 495, 1468
- Barnes S. A., 2010, *Astrophysical Journal*, 722, 222
- Barnes J. R., Cameron A. C., Donati J.-F., James D. J., Marsden S. C., Petit P., 2005, *Monthly Notices of the Royal Astronomical Society: Letters*, 357, L1
- Basri G., Nguyen H. T., 2018, *Astrophysical Journal*, 863, 190
- Basu S., Chaplin W. J., 2017, *Asteroseismic Data Analysis: Foundations and Techniques*. Princeton University Press
- Bazot M., Benomar O., Christensen-Dalsgaard J., Gizon L., Hanasoge S., Nielsen M., Petit P., Sreenivasan K. R., 2019, *Astronomy & Astrophysics*, 623, A125
- Bedding T. R., et al., 2011, *Nature*, 471, 608
- Belkacem K., et al., 2015, *Astronomy & Astrophysics*, 579, A31
- Benomar O., et al., 2013, *The Astrophysical Journal*, 767, 158
- Benomar O., Takata M., Shibahashi H., Ceillier T., García R. A., 2015, *Monthly Notices of the Royal Astronomical Society*, 452, 2654
- Benomar O., et al., 2018, *Science*, 361, 1231
- Bensby T., Feltzing S., Lundström I., 2004, *Astronomy & Astrophysics*, 421, 969
- Berdyugina S. V., 2005, *Living Reviews in Solar Physics*, 2, 8
- Berta Z. K., Irwin J., Charbonneau D., Burke C. J., Falco E. E., 2012, *Astronomical Journal*, 144, 145

- Blanco-Cuaresma S., 2019, Monthly Notices of the Royal Astronomical Society, 486, 2075
- Borucki W. J., et al., 2010, Science, 327, 977
- Brun A. S., 2003, EAS Publications Series, 9, 179
- Brun A., Browning M., 2017, Living Reviews in Solar Physics, 14, 4
- Brun A. S., Strugarek A., Noraz Q., Perri B., Varela J., Augustson K., Charbonneau P., Toomre J., 2022, Astrophysical Journal, 926, 21
- Cantiello M., Mankovich C., Bildsten L., Christensen-Dalsgaard J., Paxton B., 2014, The Astrophysical Journal, 788, 93
- Cao L., Pinsonneault M. H., 2022, Monthly Notices of the Royal Astronomical Society, 517, 2165
- Cao L., Pinsonneault M. H., van Saders J. L., 2023, Astrophysical Journal, 951
- Casagrande L., Ramirez I., Melendez J., Bessell M., Asplund M., 2010, Astronomy & Astrophysics, 512, A54
- Casamiquela L., Castro-Ginard A., Anders F., Soubiran C., 2021, Astronomy & Astrophysics, 654, A151
- Ceillier T., Eggenberger P., García R. A., Mathis S., 2013, Astronomy & Astrophysics, 555, A54
- Ceillier T., et al., 2017, Astronomy & Astrophysics, 605, A111
- Chahal D., de Grijs R., Kamath D., Chen X., 2022, Monthly Notices of the Royal Astronomical Society, 514, 4932
- Charbonnel C., Talon S., 2005, Science, 309, 2189
- Charbonnel C., Talon S., 2008, pp 163–174
- Charbonnel C., Vauclair S., Maeder A., Meynet G., Schaller G., 1994, Astronomy & Astrophysics, 283, 155
- Christensen-Dalsgaard J., 2008, Astrophysics and Space Science, 316, 113
- Christensen-Dalsgaard J., Gough D. O., 1982, Monthly Notices of the Royal Astronomical Society, 198, 141
- Christensen-Dalsgaard J., Schou J., Thompson M. J., 1990, Monthly Notices of the Royal Astronomical Society, 242, 353

- Christensen-Dalsgaard J., Hansen P. C., Thompson M. J., 1993, Monthly Notices of the Royal Astronomical Society, 264, 541
- Claytor Z. R., van Saders J. L., Llama J., Sadowski P., Quach B., Avallone E. A., 2022, Astrophysical Journal, 927, 219
- Claytor Z. R., van Saders J. L., Cao L., Pinsonneault M. H., Teske J., Beaton R. L., 2023, arXiv e-prints, p. arXiv:2307.05664
- Collier Cameron A., 2007, Astronomische Nachrichten, 328, 1030
- Cranmer S. R., Saar S. H., 2011, Astrophysical Journal, 741, 54
- Crowther P. A., 2007, Annual Review of Astronomy & Astrophysics, 45, 177
- Curtis J. L., Agüeros M. A., Douglas S. T., Meibom S., 2019, The Astrophysical Journal, 879, 49
- Curtis J. L., et al., 2020, The Astrophysical Journal, 904, 140
- Davenport J. R. A., 2017, The Astrophysical Journal, 835, 16
- Davenport J. R. A., Covey K. R., 2018, The Astrophysical Journal, 868, 151
- David T. J., Angus R., Curtis J. L., van Saders J. L., Colman I. L., Contardo G., Lu Y., Zinn J. C., 2022, The Astrophysical Journal, 933, 114
- Deheuvels S., et al., 2014, Astronomy & Astrophysics, 564, A27
- Deheuvels S., Ballot J., Beck P. G., Mosser B., Østensen R., García R. A., Goupil M. J., 2015, Astronomy & Astrophysics, 580, A96
- Deheuvels S., Ballot J., Eggenberger P., Spada F., Noll A., Hartogh J. W. d., 2020, Astronomy & Astrophysics, 641, A117
- Delorme P., Collier Cameron A., Hebb L., Rostron J., Lister T. A., Norton A. J., Pollacco D., West R. G., 2011, Monthly Notices of the Royal Astronomical Society, 413, 2218
- Di Mauro M. P., Ventura R., Corsaro E., Moura B. L. D., 2018, The Astrophysical Journal, 862, 9
- Distefano E., Lanzafame A. C., Lanza A. F., Messina S., Korn A. J., Eriksson K., Cuypers J., 2012, Monthly Notices of the Royal Astronomical Society, 421, 2774
- Distefano E., et al., 2023, Astronomy & Astrophysics, 674
- Douglas S. T., Agüeros M. A., Covey K. R., Kraus A., 2017, The Astrophysical Journal, 842, 83

- Douglas S. T., Curtis J. L., Agüeros M. A., Cargile P. A., Brewer J. M., Meibom S., Jansen T., 2019, *The Astrophysical Journal*, 879, 100
- Dumont T., Palacios A., Charbonnel C., Richard O., Amard L., Augustson K., Mathis S., 2021, *Astronomy & Astrophysics*, 646, A48
- Eddington A. S., 1918, *The Astrophysical Journal*, 48, 205
- Eddington A. S., 1926, *The Internal Constitution of the Stars*. Cambridge University Press
- Eddington A. S., 1929, *Monthly Notices of the Royal Astronomical Society*, 90, 54
- Eggenberger P., 2013, *EPJ Web of Conferences*, 43, 01005
- Eggenberger P., Meynet G., Maeder A., Hirschi R., Charbonnel C., Talon S., Ekström S., 2008, *Astrophysics and Space Science*, 316, 43
- Eggenberger P., Miglio A., Montalban J., Moreira O., Noels A., Meynet G., Maeder A., 2010, *Astronomy & Astrophysics*, 509, A72
- Eggenberger P., Montalbán J., Miglio A., 2012, *Astronomy & Astrophysics*, 544, L4
- Eggenberger P., et al., 2019, *Astronomy & Astrophysics*, 621, A66
- Elvey C. T., 1929, *The Astrophysical Journal*, 70, 141
- Fang X.-S., Zhao G., Zhao J.-K., Bharat Kumar Y., 2018, *Monthly Notices of the Royal Astronomical Society*, 476, 908
- Fellay L., Buldgen G., Eggenberger P., Khan S., Salmon S. J. A. J., Miglio A., Montalbán J., 2021, *Astronomy & Astrophysics*, 654, A133
- Fricke K., 1967, *Science*, 156, 1101
- Fuller J., Cantiello M., Stello D., Garcia R. A., Bildsten L., 2015, *Science*, 350, 423
- Fuller J., Piro A. L., Jermyn A. S., 2019, *Monthly Notices of the Royal Astronomical Society*, 485, 3661
- Gallet F., Bouvier J., 2013, *Astronomy & Astrophysics*, 556, A36
- Garaud P., 2002, *Monthly Notices of the Royal Astronomical Society*, 335, 707
- Garcia R. A., et al., 2014, *Astronomy & Astrophysics*, 572, A34
- Gehan C., Mosser B., Michel E., Samadi R., Kallinger T., 2018, *Astronomy & Astrophysics*, 616, A24
- Gehan C., Mosser B., Michel E., 2019, *EAS Publications Series*, 82, 225

- Gibson B. K., Fenner Y., Renda A., Kawata D., Lee H., 2003, Publications of the Astronomical Society of Australia, 20, 393
- Goldreich P., Schubert G., 1967, The Astrophysical Journal, 150, 571
- Gordon T. A., Davenport J. R. A., Angus R., Foreman-Mackey D., Agol E., Covey K. R., Agüeros M., Kipping D., 2021, The Astrophysical Journal, 913
- Gough D. O., 1981, Solar Physics, 74, 21
- Gough D. O., 2015, Space Science Reviews, 196, 15
- Gough D. O., Thompson M. J., 1990, Monthly Notices of the Royal Astronomical Society, 242, 25
- Gough D., Toomre J., 1991, Annual Review of Astronomy and Astrophysics, 29, 627
- Gough D. O., Sekii T., Stark P. B., 1996, The Astrophysical Journal, 459, 779
- Gustafsson B., Edvardsson B., Eriksson K., Jørgensen U. G. N. A. P. B., 2008, Astronomy & Astrophysics, 486, 951
- Hall O. J., et al., 2021, Nature Astronomy, 5, 707
- Hansen C. J., Cox J. P., van Horn H. M., 1977, The Astrophysical Journal, 217, 151
- Hartman J. D., et al., 2009, The Astrophysical Journal, 691, 342
- Hartman J. D., Bakos G. Á., Kovács G., Noyes R. W., 2010, Monthly Notices of the Royal Astronomical Society, 408, 475
- Hathaway D. H., 2015, Living Reviews in Solar Physics, 12, 4
- Hatt E., et al., 2023, Astronomy & Astrophysics, 669, A67
- Hegedűs V., Mészáros S., Jofré P., Stringfellow G. S., Feuillet D., García-Hernández D. A., Nitschelm C., Zamora O., 2023, Astronomy & Astrophysics, 670
- Heger A., 1998, PhD thesis, Technical University of Munich
- Heger A., Langer N., Woosley S. E., 2000, The Astrophysical Journal, 528, 368
- Henderson C. B., Stassun K. G., 2012, The Astrophysical Journal, 747, 51
- Herbst W., Bailer-Jones C. a. L., Mundt R., Meisenheimer K., Wackermann R., 2002, Astronomy & Astrophysics, 396, 513
- Hermes J. J., et al., 2017a, The Astrophysical Journal Supplement Series, 232, 23

- Hermes J. J., Kawaler S. D., Bischoff-Kim A., Provencal J. L., Dunlap B. H., Clemens J. C., 2017b, *The Astrophysical Journal*, 835, 277
- Hoffman M. D., Gelman A., 2014, *Journal of Machine Learning Research*, 15, 1593
- Holtzman J. A., et al., 2018, *The Astronomical Journal*, 156, 125
- Howe R., 2009, *Living Reviews in Solar Physics*, 6, 1
- Howell S. B., et al., 2014, *Publications of the Astronomical Society of the Pacific*, 126, 398
- Irwin J., Hodgkin S., Aigrain S., Bouvier J., Hebb L., Moraux E., 2008, *Monthly Notices of the Royal Astronomical Society*, 383, 1588
- Irwin J., Aigrain S., Bouvier J., Hebb L., Hodgkin S., Irwin M., Moraux E., 2009, *Monthly Notices of the Royal Astronomical Society*, 392, 1456
- Irwin J., Berta Z. K., Burke C. J., Charbonneau D., Nutzman P., West A. A., Falco E. E., 2011, *Astrophysical Journal*, 727, 56
- Johnson J. A., Fields B. D., Thompson T. A., 2020, *Philosophical Transactions of the Royal Society A: Mathematical, Physical and Engineering Sciences*, 378, 20190301
- Johnstone C. P., Güdel M., Lüftinger T., Toth G., Brott I., 2015a, *Astronomy & Astrophysics*, 577, A27
- Johnstone C. P., Güdel M., Brott I., Lüftinger T., 2015b, *Astronomy & Astrophysics*, 577
- Kissin Y., Thompson C., 2015, *The Astrophysical Journal*, 808, 35
- Kraft R. P., 1967, *The Astrophysical Journal*, 150, 551
- Lagarde N., Decressin T., Charbonnel C., Eggenberger P., Ekström S., Palacios A., 2012, *Astronomy & Astrophysics*, 543, A108
- Landin N. R., Mendes L. T. S., Vaz L. P. R., 2010, *Astronomy & Astrophysics*, 510, A46
- Lanza A. F., Rodono M., 1996, *Astronomy & Astrophysics*, 306, 145
- Lanzafame A. C., Spada F., 2015, *Astronomy & Astrophysics*, 584, A30
- Laughlin G., Adams F. C., 1997, *The Astrophysical Journal*, 491, L51
- Li Y., Bedding T. R., Li T., Bi S., Stello D., Zhou Y., White T. R., 2020a, *Monthly Notices of the Royal Astronomical Society*, 495, 2363
- Li T., Bedding T. R., Christensen-Dalsgaard J., Stello D., Li Y., Keen M. A., 2020b, *Monthly Notices of the Royal Astronomical Society*, 495, 3431

- Lockwood G. W., Skiff B. A., Henry G. W., Henry S., Radick R. R., Baliunas S. L., Donahue R. A., Soon W., 2007, *The Astrophysical Journal Supplement Series*, 171, 260
- Lomb N. R., 1976, *Astrophysics and Space Science*, 39, 447
- Lorenzo-Oliveira, Diego et al., 2018, *Astronomy & Astrophysics*, 619, A73
- Lorenzo-Oliveira D., Porto de Mello G. F., Dutra-Ferreira L., Ribas I., 2016, *Astronomy & Astrophysics*, 595
- Lu Y., Curtis J. L., Angus R., David T. J., Hattori S., 2022, *The Astronomical Journal*, 164, 251
- Maeder A., 2009, *Physics, Formation and Evolution of Rotating Stars*. Springer
- Maeder A., Meynet G., 2000, *Annual Review of Astronomy and Astrophysics*, 38, 143
- Maeder A., Zahn J.-P., 1998, *Astronomy & Astrophysics*, 334, 1000
- Maldonado J., Villaver E., Eiroa C., Micela G., 2019, *Astronomy & Astrophysics*, 624, A94
- Marques J. P., et al., 2013, *Astronomy & Astrophysics*, 549, A74
- Masuda K., 2022, *The Astrophysical Journal*, 937, 94
- Maunder E. W., 1904, *Monthly Notices of the Royal Astronomical Society*, 64, 747
- McQuillan A., Mazeh T., Aigrain S., 2014, *The Astrophysical Journal Supplement Series*, 211, 24
- McWilliam A., Rauch M., eds, 2004, *Origin and evolution of the elements No. 4* in Carnegie Observatories astrophysics series. Cambridge University Press
- Meibom S., Mathieu R. D., Stassun K. G., 2009, *The Astrophysical Journal*, 695, 679
- Meibom S., et al., 2011, *The Astrophysical Journal*, 733, L9
- Menou K., Mer J. L., 2006, *The Astrophysical Journal*, 650, 1208
- Metcalfe T. S., et al., 2010, *The Astrophysical Journal*, 723, 1583
- Miesch M. S., 2005, *Living Reviews in Solar Physics*, 2
- Miglio A., et al., 2021, *Experimental Astronomy*, 51, 963
- Milne E. A., 1923, *Monthly Notices of the Royal Astronomical Society*, 83, 118
- Montesinos B., Thomas J. H., Ventura P., Mazzitelli I., 2001, *Monthly Notices of the Royal Astronomical Society*, 326, 877
- Moraux E., et al., 2013, *Astronomy & Astrophysics*, 560, A13

- Morris B. M., Curtis J. L., Sakari C., Hawley S. L., Agol E., 2019, *The Astronomical Journal*, 158, 101
- Morton T. D., 2015, *Astrophysics Source Code Library*
- Mosser B., et al., 2012, *Astronomy & Astrophysics*, 548, A10
- Mottola S., et al., 1995, *Planetary and Space Science*, 43, 1609
- Moyano F. D., Eggenberger P., Meynet G., Gehan C., Mosser B., Buldgen G., Salmon S. J. A. J., 2022, *Astronomy & Astrophysics*, 663, A180
- Newton E. R., Mondrik N., Irwin J., Winters J. G., Charbonneau D., 2018, *The Astronomical Journal*, 156, 217
- Nissen P. E., 2015, *Astronomy & Astrophysics*, 579, A52
- Noll A., Deheuvels S., Ballot J., 2021, *Astronomy & Astrophysics*, 647
- Noyes R. W., Hartmann L. W., Baliunas S. L., Duncan D. K., Vaughan A. H., 1984, *The Astrophysical Journal*, 279, 763
- Önehag A., Gustafsson B., Korn A., 2014, *Astronomy & Astrophysics*, 562, A102
- Ouazzani R.-M., Marques J. P., Goupil M.-J., Christophe S., Antoci V., Salmon S. J. A. J., 2019, *Astronomy & Astrophysics*, 626
- Pagel B., 2009, *Nucleosynthesis and Chemical Evolution of Galaxies*, by Bernard E. J. Pagel, Cambridge, UK: Cambridge University Press, 2009
- Pasquini L., Döllinger M. P., Weiss A., Girardi L., Chavero C., Hatzes A. P., Silva L. d., Setiawan J., 2007, *Astronomy & Astrophysics*, 473, 979
- Paxton B., Bildsten L., Dotter A., Herwig F., Lesaffre P., Timmes F., 2010, *The Astrophysical Journal Supplement Series*, 192
- Paxton B., et al., 2013, *The Astrophysical Journal Supplement Series*, 208
- Paxton B., et al., 2015, *The Astrophysical Journal Supplement Series*, 220
- Paxton B., et al., 2019, *The Astrophysical Journal Supplement Series*, 243, 10
- Pinçon C., Belkacem K., Goupil M. J., Marques J. P., 2017, *Astronomy & Astrophysics*, 605, A31
- Pinsonneault M. H., Steigman G., Walker T. P., Narayanan V. K., 2002, *The Astrophysical Journal*, 574, 398

- Pont F., Eyer L., 2004, Monthly Notices of the Royal Astronomical Society, 351, 487
- Randich S., et al., 2022, Astronomy & Astrophysics, 666
- Rauer H., et al., 2014, Experimental Astronomy, 38, 249
- Rebull L. M., et al., 2016, Astrophysical Journal, 152, 113
- Reggiani H., Meléndez J., Yong D., Ramírez I., Asplund M., 2016, Astronomy & Astrophysics, 586, A67
- Reiners A., Schmitt J. H. M. M., 2002, Astronomy & Astrophysics, 384, 155
- Reinhold T., Hekker S., 2020, Astronomy & Astrophysics, 635, A43
- Reinhold T., Reiners A., 2013, Astronomy & Astrophysics, 557, A11
- Reinhold T., Reiners A., Basri G., 2013, Astronomy & Astrophysics, 560, A4
- Reinhold T., Bell K. J., Kuszlewicz J., Hekker S., Shapiro A. I., 2019, Astronomy & Astrophysics, 621, A21
- Reinhold T., Shapiro A. I., Witzke V., Nèmec N.-E., Işık E., Solanki S. K., 2021, The Astrophysical Journal Letters, 908, L21
- Ricker G. R., et al., 2014, Journal of Astronomical Telescopes, Instruments, and Systems, 1, 014003
- Rüdiger G., Schultz M., Stefani F., Mond M., 2015, The Astrophysical Journal, 811, 84
- Ruediger G., Gellert M., Schultz M., Hollerbach R., Stefani F., 2014, Monthly Notices of the Royal Astronomical Society, 438, 271
- Saar S. H., 2011, Conference proceedings: Physics of Sun and Star Spots, 273, 61
- Salaris M., Cassisi S., 2017, Royal Society Open Science, 4, 170192
- Salpeter E. E., 1955, The Astrophysical Journal, 121, 161
- Salvatier J., Wiecki T. V., Fonnesbeck C., 2016, PeerJ Computer Science, 2, e55
- Santos A. R. G., Breton S. N., Mathur S., García R. A., 2021, The Astrophysical Journal Supplement Series, 255, 17
- Scargle J. D., 1982, Astrophysical Journal, 263, 835
- Schunker H., Schou J., Ball W. H., Nielsen M. B., Gizon L., 2016, Astronomy & Astrophysics, 586, A79

- Scott T. R., Heamshaw J., Watson R., Kilmartin P., Gilmore A., 1992, Journal of Astrophysics and Astronomy, 13, 279
- See V., Roquette J., Amard L., Matt S. P., 2021, Astrophysical Journal, 912, 2
- Shetrone M., et al., 2015, The Astrophysical Journal Supplement Series, 221, 24
- Skumanich A., 1972, The Astrophysical Journal, 171, 565
- Smith V. V., et al., 2021, The Astronomical Journal, 161, 254
- Somers G., Pinsonneault M. H., 2015, Proceedings of the International Astronomical Union, 10, 91
- Spada F., Lanzafame A. C., 2020, Astronomy & Astrophysics, 636, A76
- Spada F., Gellert M., Arlt R., Deheuvels S., 2016, Astronomy & Astrophysics, 589, A23
- Spina L., et al., 2020, The Astrophysical Journal, 895, 52
- Spruit H. C., 2002, Astronomy and Astrophysics, 381, 923
- Strugarek A., Brun S., Zahn J., 2011, Astronomy & Astrophysics, 532
- Struve O., 1930, The Astrophysical Journal, 72, 1
- Struve O., Elvey C. T., 1930, Nature, 125, 308
- Takahashi K., Langer N., 2021, Astronomy & Astrophysics, 646, A19
- Tayar J., et al., 2015, The Astrophysical Journal, 807, 82
- Tayar J., Claytor Z. R., Huber D., van Saders J., 2022, The Astrophysical Journal, 927, 31
- Unno W., Osaki Y., Ando H., Saio H., Shibahashi H., 1979, Nonradial oscillations of stars. University of Tokyo Press
- Vaughan A. H., Preston G. W., 1980, Publications of the Astronomical Society of the Pacific, 92, 385
- Walkowicz L. M., Basri G. S., 2013, Monthly Notices of the Royal Astronomical Society, 436, 2
- Wheeler A. J., Abruzzo M. W., Casey A. R., Ness M. K., 2023, The Astronomical Journal, 165, 68
- Wilson O. C., 1963, Astrophysical Journal, 138, 832
- Wilson T. A., Casey A. R., 2023, Monthly Notices of the Royal Astronomical Society, 524, 1

- Wilson T. A., Casey A. R., Mandel I., Ball W. H., Bellinger E. P., Davies G., 2023, Monthly Notices of the Royal Astronomical Society, 521, 3
- Wright N. J., Drake J. J., Mamajek E. E., Henry G. W., 2011, The Astrophysical Journal, 743, 48
- Zahn J. P., 1992, Astronomy & Astrophysics, 265, 115
- Zhang J., et al., 2020, The Astrophysical Journal Supplement Series, 247, 9
- de Grijs R., Kamath D., 2021, Universe, 7, 440
- den Hartogh J. W., Eggenberger P., Hirschi R., 2019, Astronomy & Astrophysics, 622, A187
- van Saders J. L., Pinsonneault M. H., Barbieri M., 2019, The Astrophysical Journal, 872, 128
- von Zeipel H., 1924, Monthly Notices of the Royal Astronomical Society, 84, 684